Development of Terahertz Vacuum Electronics for Array Receivers

Dissertation
for attaining the PhD degree
of Natural Sciences

submitted to the Faculty of Physics
of the Johann Wolfgang Goethe University
in Frankfurt am Main

by
Mikko Kotiranta
from Helsinki, Finland

Frankfurt am Main 2012
D30

accepted by the Faculty of Physics of the

Johann Wolfgang Goethe University as a dissertation.

Dean:

Expert assessor:

Date of the disputation:

ABSTRACT

Heterodyne array receivers are employed in radio astronomy to reduce the observing time needed for mapping extended sources. One of the main factors limiting the number of pixels in terahertz receivers is the difficulty of generating a sufficient amount of local oscillator power. Another challenge is efficient diplexing and coupling of local oscillator and signal power to the detectors. These problems are attacked in this dissertation by proposing the application of two terahertz amplifier types for the amplification of the LO-signal and by introducing a new method for finding the defects in a quasioptical diplexer.

A 670-GHz power module based on a traveling wave tube amplifier (TWT) with a folded waveguide slow wave structure (SWS) has been presented in the literature. The total bandwidth of the device is 15 GHz and it produces a pulsed peak power of more than 100 mW. In this work, a traveling wave tube design based on a helix SWS at 825 GHz is presented. The helix SWS allows a larger bandwidth to be obtained. The size of the helix at terahertz frequencies is just a few tens of micrometers, so application of microfabrication methods is required. However, the circular shape does not lend itself easily for microfabrication. A square shape is adopted and the cold parameters of a helix SWS standing on a quartz substrate are simulated with 3D electromagnetic software. Efficient coupling of the input and output signals is realized with three different coupler types based on a helix to coplanar waveguide (CPW) and a CPW to rectangular waveguide transition. Three dimensional particle-in-cell (PIC) simulations of a traveling wave tube based on the designed square helix SWS and couplers are performed to demonstate the broadband amplification performance and to characterize the saturation behavior of the TWT. To author's knowledge, such a configuration has not been simulated before. A small-signal gain of 18.3 dB at 825 GHz and a 3-dB bandwidth of 69 GHz has been achieved. The output power of 1 mW at 900 GHz from a state-of-art solid-state frequency multiplier chain could be thus boosted to beyond 64 mW.

In order to produce LO-power at even higher frequencies, the operation of

a 850-GHz square helix TWT as a frequency doubler is studied. Frequency multiplication with multistage TWTs and gyro-TWTs at microwave frequencies has been demonstrated in the literature. Here, a single-stage TWT is shown to exhibit a simulated conversion efficiency of 7% to the second harmonic at 1700 GHz for an input power of 25 mW which is comparable with the efficiencies of state-of-art solid-state doublers.

This dissertation discusses also a 1 THz cascade backward wave amplifier based on a double corrugated waveguide SWS (DCW-SWS). Specifically, three couplers between the DCW-SWS and a rectangular waveguide are presented. The first structure exploits linear height tapering of the corrugations, but while providing excellent performance, the microfabrication of it is difficult. In the second coupler, the distance between the corrugations in the transverse direction is tapered linearly until the corrugations merge with the waveguide side walls. Good performance is obtained when the taper is made long enough. In order to keep the coupler length as short as possible, a third coupler type is introduced. Not only the distance between the corrugations in transverse direction is tapered nonlinearly, but also the other end of the corrugations is extended to touch the waveguide side walls. This novel coupler provides a -10 dB bandwidth of 250 GHz for a length of just 475 μm.

The loss per SWS period must be known for deciding the length of the SWS and consequently the gain of the amplifier. The losses may increase significantly in the terahertz region due to surface roughness. The S-parameters of DCW-SWS samples having lengths of 100, 150 and 200 periods are measured at 1 THz for determining the loss per SWS period. The insertion loss of each sample is close to 40 dB, even though differences in the order of 10 dB are expected. Visual inspection of the samples reveals significant deviations from the target corrugation height of 60 μm, and simulations confirm a 15 μm height excess of just a few corrugations to be sufficient for causing the measured insertion loss.

The input and output signals entering or leaving the slow wave structure are required to pass through a vacuum window. Mounting a window inside a terahertz waveguide is difficult due to the tiny size. This work presents a novel solution that allows a larger window diameter to be used: a quartz window is integrated inside a dual-mode horn antenna. The simulated radiation properties of the designed dual-mode horn exhibit improved Gaussian beam properties over a single-mode conical horn. The simulated E- and H-plane beamwidths are 3.2° and 2.3° at 1040 GHz, respectively, and the sidelobes are below -35 dB. These horns allow quasioptical coupling of the input and output signals to the amplifier, which makes the amplifier well suited for mea-

surements with a photomixer or molecular gas laser source. A quasioptical measurement setup for measuring the transmittance and reflectance of the amplifier has been designed and built, and calibration measurements with photomixers show the transmittance and reflectance losses caused by the setup itself to be within 0.7 dB from the ideal 9 dB and 12 dB, respectively.

Diplexing of the LO and signal beams is often performed with a Martin-Puplett interferometer. Misalignment and deformation of the quasioptical components cause the optical path length difference between the two arms of the interferometer to deviate from the desired value, which leads to incorrect polarization state of the output signal and, consequently, to coupling losses. A ray-tracing program has been developed for studying the influence of defects to the path lengths. When information about the measured optical path lengths of the beams related to the different receiver pixels are fed to a ray-tracing program, it computes the corresponding component configuration. The results of simulated defects are in agreement with verification measurements. Furthermore, five defect parameters are shown to be sufficient for reproducing the measured path length differences in the diplexer of the multi-pixel receiver CHAMP$^+$. The quasioptical configuration of the diplexer may thus be corrected to obtain a higher receiver sensitivity.

KURZFASSUNG

Heterodyne Array Empfänger werden in der Radioastronomie eingesetzt, um die Beobachtungszeit für Quellen zu verringern, die viel grösser als die Keulenbreite sind. Solche Quellen sind zum Beispiel interstellare Molekulargaswolken, in denen Sterne entstehen. Zahlreiche Rotationsübergänge von verschiedenen Molekülen können im Terahertzbereich beobachtet werden, und helfen so dem Verständnis von Prozessen, die für die Sternentstehung von Relevanz sind. Eine der Hauptschwierigkeiten, die die Anzahl der Pixel in Empfängern im Terahertzbereich begrenzt, ist die Verfügbarkeit von genügend hoher Lokaloszillatorenleistung. Eine weitere Schwierigkeit stellt das effiziente Diplexing und die Kopplung der Lokaloszillatoren und der Signalleistung an die Detektoren dar. Diese Herausforderungen werden in der vorliegenden Dissertation in Angriff genommen, indem zwei Terahertz-Verstärkermodelle zur Verstärkung des LO-Signals vorgeschlagen werden und indem eine neue Methode zur Ermittlung von Defekten in quasioptischen Diplexern vorgestellt wird.

Mit den neusten, kompakten und einstellbaren Halbleitervervielfacherketten kann eine Ausgangsleistung von 1 μW bei 900 GHz bei Raumtemperatur erreicht werden. Molekulargaslaser sind zwar leistungsfähiger, aber ihr Ausmass und die Tatsache, dass ihre Frequenz nicht kontinuierlich einstellbar ist, verringert ihren Anwendungsbereich. Mit steigender Anzahl Pixel wird das Leistungsteilernetzwerk komplizierter und verlustbehafteter. Obwohl die supraleitenden Mischer nur einige Mikrowatt Pumpleistung benötigen, ist eine Zunahme von einer ganzen Grössenordnung in der Lokaloszillatorenleistung oberhalb 1 THz erforderlich, um einen Array von hunderten von Pixeln zu betreiben.

Ein 670-GHz Leistungsmodul, das auf einem Wanderfeldröhrenverstärker (TWT) in Kombination mit einer gefalteten Hohlleiter-Verzögerungsleitung (SWS) basiert, wurde bereits in der Literatur vorgeschlagen. Die Gesamtbandbreite dieses Moduls ist 15 GHz und die gepulste Spitzenleistung beträgt mehr als 100 mW. Für diese Dissertation wurde eine Wanderfeldröhre

entworfen, die auf einer Helix-SWS bei einer Frequenz von 825 GHz beruht. Die Verwendung einer Helix ermöglicht eine Bandbreitenvergrösserung. Die Signalverstärkung in einer Vakuumröhre basiert auf der Wechselwirkung zwischen einem Elektronenstrahl und einer elektromagnetischen (EM) Welle, wobei die Elektronengeschwindigkeit ungefähr mit der Phasengeschwindigkeit übereinstimmen muss. Die Aufgabe der Verzögerungsleitung (SWS) einer Vakuumröhre ist es, die Phasengeschwindigkeit der EM-Welle bis auf etwa einen Fünftel der Lichtgeschwindigkeit zu reduzieren, damit die Elektronen anhand einer Beschleunigungsspannung von circa 10 kV in einen Geschwindigkeitssynchronismus gebracht werden können. Zusätzlich ist die SWS für die axiale Komponente des elektrischen Feldes verantwortlich, die die Elektronen beschleunigen oder abbremsen kann.

Die Helixgrösse nimmt umgekehrt proportional zur Frequenz ab, so dass sie bei einer Frequenz von 1 THz nur noch ein paar Dutzend Mikrometer beträgt, was nicht nur die herkömmliche maschinelle Bearbeitung verunmöglicht, sondern auch die Mikrofabrikationsmethoden an die Grenze des Möglichen bringt. Zusätzlich eignet sich die kreisförmige Form der Helix-SWS nicht gut für die Mikrofabrikation durch etablierte Technologien wie zum Beispiel das LIGA (Lithographie, Galvanoformung, Abformung) Verfahren, da es sich dabei im Wesentlichen um zwei-dimensionale Prozesse handelt. Deshalb wurde im Laufe dieser Arbeit eine Helix mit einer rechteckigen Form entworfen. Der Entwurfsprozess basiert auf den Gleichungen einer kreisförmigen Helix, deren Umfang mit dem der rechteckigen Helix übereinstimmt. Die Eigenschaften einer SWS werden mit drei Parametern — der Phasengeschwindigkeit, der Kopplungsimpedanz und den Verlusten — definiert, die aus dreidimensionalen elektromagnetischen Simulationen ermittelt werden können. Für die vorliegende Arbeit wurde eine Helixperiode mit Hilfe des CST Microwave Studios simuliert, nachdem eine Abschätzung der Verstärkung im Kleinsignalbereich anhand eines analytischen Wellenleitermodells berechnet worden war.

Eine effiziente Signalkopplung mit drei verschiedenen Kopplungsstrukturen für den Ein- und Ausgang der Helix-SWS wurden, basierend auf dem Übergang von der Helix zu einer Koplanarleitung (CPW) und einer CPW zu einem Rechteckhohlleiter, entwickelt. Der Übergang zwischen der CPW und dem Hohlleiter wurde mit einem sich in der E-Ebene befindenden Pfosten, einem Patch und einem Steghohlleiter realiziert. Um die Breitbandverstärkungseigenschaften nachzuweisen und das Sättigungsverhalten einer TWT, die auf einer rechteckigen Helix und den entwickelten Kopplern beruht, zu charakterisieren, wurden dreidimensionale Particle-in-Cell (PIC) Simulationen durchgeführt. Soweit dem Autor bekannt, ist die Simulation dieser Anordnung ein-

zigartig. Für die Simulationen wurde ein vorfokussierter zylindrischer Elektronenstrahl mit einem Durchmesser von 17 µm und einem Strom von 2.7 mA verwendet. Die Raumladungskräfte im Strahl versuchen, die Elektronen auseinander zu treiben, was mit einem axialen Magnetfeld von 1 T verhindert wird, indem die Elektronen mit einer Geschwindigkeitskomponente in Querrichtung durch die Lorentzkraft in eine kreisförmige Bahn abgelenkt werden. Durch die Wechselwirkung zwischen Strahl und elektromagnetischer Welle, wird das in der Helix fortschreitende Signal verstärkt. Die maximale Verstärkung wurde mit einer Beschleunigungsspannung von 9650 V erreicht und führte zu einer maximalen Kleinsignalverstärkung von 18.3 dB und zu einer 3-dB Bandbreite von 69 GHz bei einer Betriebsfrequenz von 825 GHz. Mit einer Eingangsleistung von 9 dBm wurde die höchste Ausgangsleistung von 25.8 dBm erreicht. Eine noch höhere Eingangsleistung hatte zur Folge, dass die Elektronen, durch die erhöhten Coulombkräfte, gegen das Ende der Röhre mit der Helix-SWS kollidierten.

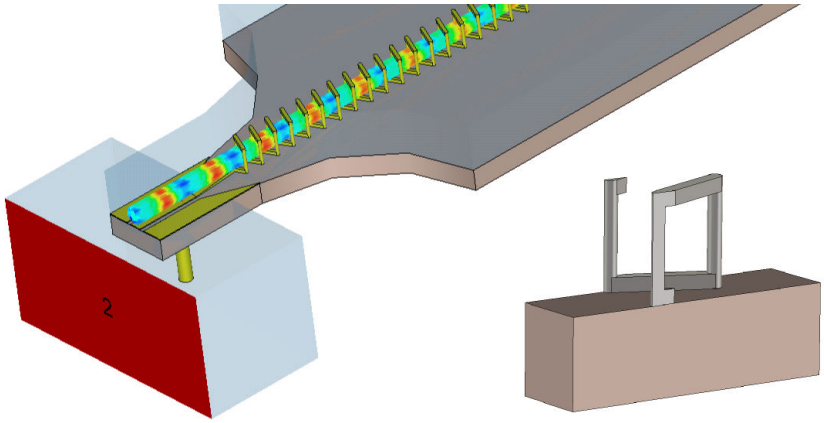

Abbildung 1: Ein geschwindigkeitsmodulierter Elektronenstrahl in der rechteckigen Helix Verzögerungsleitung. Der Durchmesser der Helix beträgt 30 µm. Die Kopplung zum Rechteckhohlleiter wurde hier durch einen Pfosten realisiert.

Die Wechselwirkung zwischen dem Elektronenstrahl und der elektromagnetischen Welle ist ein nichtlinearer Prozess, während dem harmonische Frequenzkomponenten der Eingangsfrequenz erzeugt werden. Um LO-Leistung bei noch höheren Frequenzen zu erzielen, wurde der Betrieb einer 850 GHz rechteckigen Helix TWT als Frequenzdoppler untersucht. Frequenzvervielfachung mit mehrstufigen TWTs und Gyro-TWTs bei Mikrowellenfrequenzen wurden in der Literatur bereits vorgestellt. Für diese Dissertation wurde jedoch eine einstufige TWT ohne eine Verstärkungsstufe simuliert, die einen Umwandlungswirkungsgrad von 7% zur zweiten Harmonischen bei 1700 GHz

bei einer Eingangsleistung von 25 mW aufweist. Dieser Wirkungsgrad ist mit dem von hochmodernen Halbleiter-Dopplern vergleichbar.

Die Dissertation stellt auch einen 1-THz Kaskadenrückwärtswellenverstärker vor, der auf einer Doppel-Pfosten-Hohlleiter-SWS (DCW-SWS) basiert. Die DCW-SWS ist kompatibel mit dem Röntgen-LIGA Verfahren und ermöglicht eine starke Wechselwirkung mit dem zylinderförmigen Elektronenstrahl zwischen den Pfosten. Insbesondere werden drei Kopplungsstrukturen zwischen einer DCW-SWS und einem Rechteckhohlleiter vorgestellt. Für die erste Struktur wird die Pfostenhöhe in axialer Richtung schrittweise verkürzt. Obschon eine solche Struktur eine ausgezeichnete Impedanzanpassung zwischen dem DCW-SWS und dem Rechteckhohlleiter über ein breites Frequenzspektrum liefert, benötigt jede Höhenstufe eine separate LIGA-Maske, die mit Mikrometergenauigkeit ausgerichtet werden muss. Eine andere Möglichkeit wäre, die Struktur um 90 Grad zu drehen und die Seite zu beleuchten. Die präzise Drehung einer Struktur mit Dimensionen im Mikrometerbereich ist allerdings anspruchsvoll. In der zweiten entworfenen Struktur bleibt die Pfostenhöhe konstant, und die Distanz zwischen den Pfosten vergrössert sich linear in Querrichtung bis die Pfosten in die Hohlleiterwände übergehen. Eine gute Leistung wird erzielt, wenn der Pfostenabstand in Querrichtung über eine genügend lange Strecke zunimmt. Um dabei die Kopplerlänge so kurz wie möglich zu halten, wurde eine dritte Kopplungsstruktur entwickelt, in welcher nicht nur die Distanz zwischen den Pfosten in Querrichtung nichtlinear vergrössert wird, sondern zusätzlich die Pfosten bis hin zu den Seitenwänden des Hohlleiters verbreitert werden. Diese neuartige Kopplungsstruktur liefert eine -10 dB Bandbreite von 250 GHz bei einer Gesamtlänge von nur 475 μm.

Der Verlust per SWS Periode muss bekannt sein, damit die Länge der SWS und folglich auch die Signalverstärkung bestimmt werden können. Die Verluste der Verzögerungsleitung können bei Terahertzfrequenzen aufgrund von Oberflächenunebenheiten massgeblich ansteigen, da die Eindringtiefe, zum Beispiel, bei 1 THz nur 66 nm beträgt. Dadurch wird die Strecke, die der Strom zurücklegt, verlängert, und folglich wird der effektive Widerstand erhöht. Die S-Parameter der DCW-SWS Muster mit den Längen 100, 150 und 200 Perioden wurden bei 1 THz gemessen, um den Verlust per SWS Periode zu bestimmen. Die Einfügungsdämpfung von allen Mustern ist in der Nähe von 40 dB, auch wenn Unterschiede in der Höhe von 10 dB erwartet wurden. Die visuelle Inspektion der Musterstrukturen offenbarte erhebliche Abweichungen von der geplanten Pfostenhöhe von 60 μm. Zusätzlich bestätigten Simulationen, dass die nur wenigen etwa 15 μm zu hohen Pfosten für einen drastischen Anstieg der Einfügungsdämpfung genügen.

Das Ein- und Ausgangssignal in und aus der Verzögerungsleitung muss jeweils ein Vakuumfenster durchlaufen. Ein Fenster innerhalb eines WR-1.0 Hohlleiters anzubringen, ist infolge des geringen Ausmasses jedoch schwierig. In dieser Arbeit wird eine neuartige Lösung vorgestellt, die einen grösseren Fensterdurchmesser erlaubt: Ein Quarzfenster, dessen Dicke und Durchmesser 478 µm und 1.2 mm betragen, wird in eine zweimodige Hornantenne integriert. Die Fensterdicke wird so ausgewählt, dass die von beiden Grenzflächen reflektierten Wellen einander auslöschen. Wegen dem resonanten Charakter des Fensters ist die -15 dB Bandbreite auf etwa 3% begrenzt. Durch Anbringen von Rillen an der Oberfläche des Fensters könnten breitere Bandbreiten erreicht werden. Die Platzierung des Fensters in der Antenne hat jedoch eine Amplitudenveränderung und eine Phasenverschiebung der Moden zur Folge, was im Entwurf berücksichtigt werden muss. Das Horn ist sehr lang, weil es den umhüllenden Magneten durchlaufen muss. Folglich erhöht sich die Gitterzellenanzahl in den 3D Simulationen auf 500 Millionen. Simulationen mit solch einer hohen Anzahl Gitterpunkte kann nur mit einem leistungsfähigen Computercluster durchgeführt werden. Die simulierten Strahlungseigenschaften des entworfenen zweimodigen Horns besitzen verbesserte Gauss'sche Keuleneigenschaften verglichen mit einem konischen Einmodenhorn. Die Keulenbreiten in der E- und H-Ebene sind jeweils 3.2° und 2.3° bei 1040 GHz, und die Nebenkeulen sind kleiner als -35 dB. Nebst diesen 3D-Simulationen wurde das Horn auch mit einer Gauss-Laguerre-Methode analysiert, um den Einfluss der Phasendifferenz auf die Strahlungscharakteristik zu ermitteln. Die Gauss-Laguerre Berechnungen zeigen, dass eine Phasendifferenz von 20 Grad, die an den Rändern des Betriebsfrequenzbandes entsteht, nur einen geringen Einfluss auf die Keulenbreite und Erhöhung der Nebenkeulen hat.

Solche Hornantennen erlauben eine quasioptische Kopplung zwischen dem Ein- und Ausgangssignal und dem Verstärker, weshalb sich der Verstärker gut für Messungen mit einem Photomischer oder einer molekularen Gaslaserstrahlquelle eignet. Obschon heutzutage Netzwerkanalysatoren mit Hohlleiterschnittstellen bis 1.1 THz erhältlich sind, hat die Anwendung einer Laserquelle den Vorteil, dass die Saturierungseigenschaften des Verstärkers untersucht werden können. Zur Messung des Transmissions- und Reflektionsgrades des Verstärkers wurde deshalb ein quasioptischer Messaufbau entworfen und errichtet. Der Aufbau basiert auf zwei polarisierenden Drahtgittern, die die Aufgabe eines Richtkopplers in einem Netzwerkanalysatoren, erfüllen. Kalibrationsmessungen mit Photomischern zeigen, dass die vom Messaufbau entstandenen Transmissions- und Reflektionsverluste bei 0.7 dB von den idealen 9 dB beziehungsweise 12 dB liegen, wobei die Ergebnisse etwas von den Ausrichtungsfehlern beeinflusst wurden, die trotz aller Bemühungen, nicht

ganz eliminiert werden konnten.

Ein Diplexer sorgt dafür, dass sich das astronomische Signal und das Lokaloszillatorensignal räumlich übereinander ausbreiten, wenn sie den Mischer erreichen. Das Diplexing wird meist im Submillimeterbereich mit einem Martin-Puplett Interferometer (MPI) durchgeführt. Dabei wird ein einfallender Strahl im MPI mit einem polarisierenden Drahtgitter in zwei senkrecht zueinander polarisierte Komponenten aufgeteilt. Jede Komponente wird danach von einem Dachspiegel reflektiert und trifft erneut auf das Gitter. Dadurch entsteht eine überlagerte Welle, deren Polarisationsrichtung von der Differenz der optischen Weglängen der einzelnen Komponenten im Interferometer abhängt. Die Weglängen werden so gewählt, dass die Polarisationsrichtung der Welle mit der des Mischer übereinstimmt.

Falsche Ausrichtung oder Verformungen von quasioptischen Komponenten führen zu vom gewünschten Wert abweichenden optischen Weglängedifferenzen zwischen den zwei Armen des Interferometers. Dies führt weiter zu einem fehlerhaften Polarisationszustand des Ausgangssignals und folglich zu Kopplungsverlusten. In einem Single-Pixel-Empfänger können die Weglängenfehler zwischen den zwei Komponenten durch die Verschiebung eines Dachspiegels korrigiert werden. In einem Multi-Pixel-Empfänger reicht dies aber nicht, weil die Fehler für jeden Pixel unterschiedlich sind. Um die Einflüsse von Defekten der Komponenten auf die Weglängen zu untersuchen, wurde ein Lichtstrahlverfolgungsprogramm entwickelt. Wird die Information der gemessenen optischen Weglängen der Strahlen, die in Verbindung zu den verschiedenen Empfängerpixeln stehen, dem Programm übergeben, berechnet es die entsprechende Komponentenanordnung. Da die gleichen Weglängen auf mehrere Weisen auftreten können, wurden die Resultate der simulierten Defekte mit Plausibilitätsprüfungsmessungen verglichen. Die simulierte Verkippung eines Dachspiegels, der Dachwinkelfehler und die Verformung des Gitterrahmens stimmen gut mit den Testmessungen überein. Die Simulationen sagen auch eine laterale Verschiebung eines Dachspiegels voraus, die eine Grössenordnung von mehreren Millimetern hat. Das Ergebnis ist überraschend, aber die optische Konfiguration erlaubt eine solche Verschiebung, und es wird vermutet, dass der Spiegel während des Wechsels des Drahtgitters unbeabsichtigt verschoben wurde. Des Weiteren kann gezeigt werden, dass fünf Fehlerparameter zur Wiedergabe der gemessenen Weglängedifferenzen im Diplexer des Multipixel-Empfängers CHAMP$^+$ des APEX Teleskopes ausreichen. Die simulierten Defekte der quasioptischen Konfiguration können in der Anordnung korrigiert werden, was zur Erhöhung der Empfängerempfindlichkeit führt.

Contents

PREFACE **2**

1 HETERODYNE ARRAY RECEIVERS **4**

1.1 Terahertz Astronomy 4

1.2 Receivers 6

1.3 Mixers 9

1.3.1 SIS Mixers 9

1.3.2 HEB Mixers 10

1.3.3 Schottky Diode Mixers 11

1.4 Local Oscillator Sources 12

1.4.1 Solid state frequency multipliers 13

1.4.2 Molecular gas lasers 14

1.4.3 Photomixers 15

1.4.4 Quantum cascade lasers 15

1.5 Limitations of Current Technology 16

2 TERAHERTZ AMPLIFIER **18**

2.1 Introduction to Traveling Wave Tubes 18

2.2 Square Helix Traveling Wave Tube 22

2.2.1 Slow Wave Structure Design 22

2.2.2 Eigenmode Simulation 25

2.2.3 Input/Output Couplers 31

2.2.4 Cold Simulations 33

2.2.5 Particle-In-Cell Simulation 35
2.3 Frequency Multiplication 40
2.3.1 Nonlinearity in a Traveling Wave Tube 41
2.3.2 Structure of the Traveling Wave Tube 42
2.3.3 Simulated Nonlinearity 43
2.3.4 Frequency Doubler Chain 45
2.3.5 Results 47
2.4 1-THz Cascade Backward Wave Amplifier 48
2.4.1 Slow Wave Structure 49
2.4.2 Input/Output Couplers 50
2.4.3 Measurement of Losses 53
2.5 Dual-Mode Horn 58
2.5.1 Introduction 58
2.5.2 Structure 58
2.5.3 Design 61
2.5.4 Simulated Performance 63
2.5.5 Gauss-Laguerre Analysis 65
2.6 Quasioptical Measurement Setup 69
2.6.1 Polarization 69
2.6.2 Operating Principle 71
2.6.3 Characterization 73

3 QUASIOPTICAL DIPLEXER 76
3.1 Gaussian Beams 76
3.2 Martin-Puplett Interferometer 77
3.3 Ray-tracing Simulations 79
3.4 Diplexer Measurements 84
3.5 Multi-Pixel Receiver Measurements 90
3.6 Results 92

4 CONCLUSION 94

ACKNOWLEDGMENTS **100**

REFERENCES **102**

PREFACE

Heterodyne array receivers are employed in radio astronomy to reduce the observing time needed for mapping extended sources. One of the main factors limiting the amount of pixels in terahertz receivers is the difficulty of generating a sufficient amount of local oscillator power. Another challenge is efficient diplexing and coupling of local oscillator and signal power to the detectors. These problems are attacked in this dissertation by proposing the application of two terahertz amplifier types for the amplification of the LO-signal and by introducing a new method for finding defects in a quasioptical diplexer.

Chapter 1 explains why the terahertz region is important for astronomy. Array receivers and the most important mixer and local oscillator types are introduced, and this information is used to demonstrate the need for more powerful local oscillator sources. Chapter 2 introduces two terahertz vacuum electronic amplifiers that have the potential of boosting the local oscillator power more than an order of magnitude at frequencies near 1 THz. The improvement of the diplexing performance in an array receiver is addressed in Chapter 3.

1 HETERODYNE ARRAY RECEIVERS

1.1 Terahertz Astronomy

The space between the stars in our galaxy is not empty, but filled with clouds of gas and dust and energetic particles called cosmic rays [43]. Typical densities in interstellar matter are 1 gas atom per cm^3 and 1 dust particle per 10^5 m^3. Ten percent from the mass of our galaxy is interstellar gas and 0.1 percent is dust. Dust grains have typically a size less than 1 μm in diameter and they are composed of H_2O, silicates and graphene. Dust is concetrated in the inner edges of the spiral arms of our galaxy, but can also be found in dark nebulas observed as dark patches in front of background stars. The temperature of dust in the interstellar space is 10–20 K and can rise up to several hundreds of Kelvins near a star. Assuming the dust grains to be black bodies at temperature T =10–20 K, the maximum intensity is obtained at wavelengths of λ_{max} =300–150 μm, as given by the Wien's displacement law,

$$\lambda_{max} T = b, \tag{1.1}$$

where the constant b is approximately 0.003. The thermal radiation of dust is the main source of terahertz radiation in the Milky Way.

Hydrogen is the dominant constituent of interstellar matter and may be in ionized, neutral or molecular form. The typical temperature of clouds consisting of neutral hydrogen (HI) is 100 K. These cold clouds are surrounded by much warmer (8000 K), but rarer, intercloud medium. Regions of ionized hydrogen (HII) are formed near hot stars radiating strongly at ultraviolet wavelengths. The temperature of HII regions is several thousand Kelvins. Molecular hydrogen can exist only inside the densest clouds where also dust is abundant. It is formed on the surface of dust grains which act as a catalyst and also shield the molecules from UV radiation. The best environment for molecule formation is therefore inside dark nebulas or dust and gas clouds found near HII regions.

H_2 is the dominating component in molecular gas clouds, but over 140 other

molecules have been identified [55]. They are formed via collisions between atoms or simpler molecules or on the surface of dust grains as H_2 does. Observation of molecular absoption lines at optical or ultraviolet wavelengths requires that the light from a background star can penetrate through the molecular cloud, but the extinction due to dust typically prevents such observations. However, the rotational transitions of many molecules produce spectral lines in the terahertz region where the extinction is not a problem. The spatial distribution of gas can be mapped with spectral line observations, the brightness temperature (a measure of intensity) in a spectral line provides information about the gas density, Doppler-shift is used to determine the motion of the cloud as a whole and the broadening of spectral lines gives information about the gas temperature.

Molecular hydrogen itself does not have accessible emission line spectra in the physical conditions of the cold interstellar matter, but other molecular species can be used as tracer elements: the abundance of some tracer element can be assumed to be proportional to the abundance of H_2. One of the most commonly used tracer element is the CO molecule which is the most abundant molecule after H_2. Its emission lines due to rotational transitions are easily observable in the millimeter and submillimeter spectrum.

Star formation takes place in large, dense interstellar clouds. They start to collapse due to their own gravitation and split into several smaller parts, from which protostars are formed. Essential in the star formation process is that a cloud can get rid of the heat generated by the gravitational compression, otherwise the rising gas pressure is able to counter gravitation. The primary mechanism of cooling is based on the emission of terahertz photons which are produced when molecules excited through collisions decay to a lower energy state [74]. At lower densities, the main coolant is the rotational transitions of a CO molecule. As the density increases, H_2O becomes the primary coolant. At even higher densities, an ensemble of light hybride molecule species take over. Star formation in a molecular cloud can be therefore studied by observing spectral lines corresponding to different rotational transitions of the CO molecule. The higher the transition, the deeper in the cloud the radiation originates from, because the temperature of the outer regions of the cloud is not high enough to produce higher level transitions.

1.2 Receivers

Electromagnetic radiation in the terahertz frequency range from distant molecular clouds is heavily attenuated or even completely blocked primarily by the water vapor in the Earth's atmosphere. The telescopes used for observing are therefore located on top of mountains, where the atmosphere is thin and dry [36], [96]. Astronomical terahertz instruments have also been flown onboard of an airplane [38],[98] and satellites [67],[23] in order to reduce or remove the effect of the atmosphere.

The block diagram of the front end of a single-pixel heterodyne receiver is shown in Figure 1.1. A large reflector antenna collects the radiation from the observed source, after which the beam is guided into the diplexer which spatially combines the local oscillator and the astronomical signal to allow coupling to the mixer. A technology comparison from the point of view of receiver noise temperature, see (1.2), given in [83] shows that the best receiver sensitivity in the millimeter region below 180 GHz can be achieved by amplifying the astronomical signal with a low-noise high electron mobility transistor (HEMT) amplifier [91] before coupling it to the mixer. At higher frequencies it is more beneficial to couple the signal of interest directly to the mixer which converts it to a lower, intermediate frequency. The low-noise intermediate frequency (IF) amplifier amplifies the signal in order to allow further signal processing.

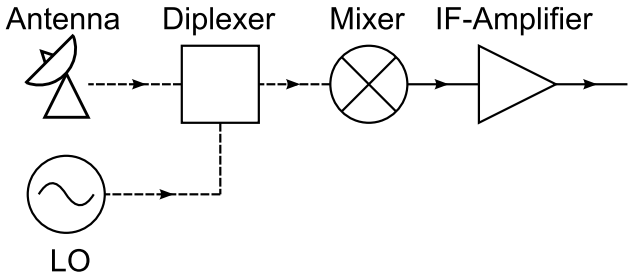

Figure 1.1: Block diagram of a THz-receiver.

Receiver noise temperature is used to characterize the performance of the receiver. The power delivered to a load resistor in a bandwidth B by a noisy source resistor at temperature T is $P_n = kTB$, where k is the Boltzmann constant. If a receiver with a noiseless matched source at the input is considered as a noise source that delivers a noise power P_n to a load resistor, the equivalent noise temperature of the receiver is defined as the temperature of a noisy resistor connected to the input of a noiseless receiver, $T_{rx} = P_n/kB$.

The noise temperature of the receiver is given by the Friis-formula [78],

$$T_{rx} = T_D + L_D T_m + L_D L_M T_{if}, \tag{1.2}$$

where $T_D = T_0 (L_D - 1)$ and L_D are the equivalent noise temperature and loss of the diplexer, T_M and L_M those of the mixer and T_{if} the equivalent noise temperature of the IF amplifier. The temperature T_0 is defined to be 290 K. The components are cooled to a cryogenic temperature for obtaining the lowest possible noise temperature. The sum of the antenna temperature T_a and the receiver noise temperature is called the system noise temperature,

$$T_{sys} = T_a + T_{rx}, \tag{1.3}$$

which determines the sensitivity of the receiver, or the minimum detectable antenna temperature, which may be expressed as

$$\Delta T = \frac{T_{sys}}{\sqrt{B\tau}}, \tag{1.4}$$

where B is the noise bandwidth of the receiver and τ the integration time of the detector output voltage [78]. The antenna temperature of a spectral line may be some millikelvins, so long integration times are required.

When T_{rx} is reduced, a shorter integration time may be used to achieve the same sensitivity. At some point the antenna temperature dominates and further reduction of T_{rx} becomes less beneficial. If extended sources much larger than the telescope beamwidth are observed, multi-beam array receivers can be utilized to reduce the required observing time considerably. For example, a 12-meter radio telescope observing at a frequency of 850 GHz has a -3 dB beamwidth of 6 arcseconds given by

$$\theta_{3dB} \approx \frac{\lambda}{D}, \tag{1.5}$$

where λ is the wavelength and D the diameter of the reflector antenna. A small beamwidth is desired in order to resolve the fine structure of the source. However, the angular diameters of molecular gas clouds extend up to several degrees. For comparison, the angular diameter of the full moon is 0.5 degrees. The mapping speed of a multi-beam receiver is characterized by the expression [35]

$$\frac{N_{pix}}{(\eta T_{sys})^2}, \tag{1.6}$$

where N_{pix} is the number of pixels and η a general efficiency term. The mapping speed increases linearly with the number of pixels and decreases

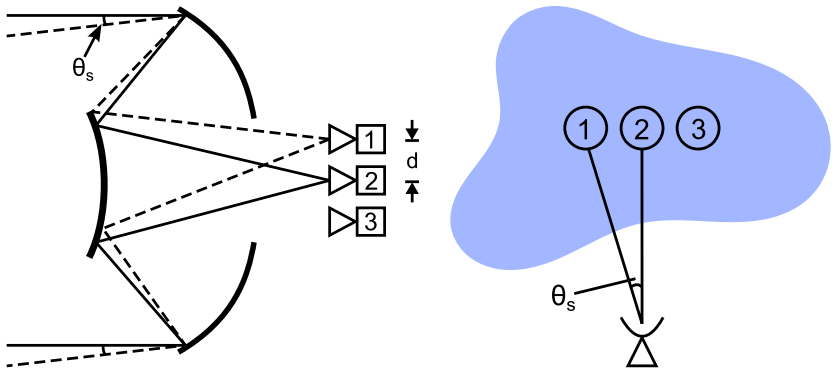

(a) (b)

Figure 1.2: (a) Array of detectors on the focal plane of a Cassegrain antenna, (b) beam spacing in the sky.

proportional to the square of the system noise temperature which means that the benefit of increasing the number of pixels is lost if a system temperature close to that of a single-pixel system cannot be maintained.

An array receiver basically consists of multiple closely packed detectors placed on the focal plane of the reflector antenna as illustrated by Figure 1.2a. The pixels can be individual receivers, but new projects integrating the components of several detectors to reduce the complexity in terms of mounting and wiring are underway [46]. A typical spacing of the detectors on the focal plane is

$$d = 2\frac{F\lambda}{D}, \tag{1.7}$$

where F is the focal length [35], which leads to a beam spacing of approximately two half power beamwidths on the sky (Figure 1.2b), since

$$d = \tan\theta_s F \approx \theta_s F \tag{1.8}$$

$$\theta_s \approx \frac{d}{F} = 2\frac{D}{\lambda} = 2\theta_{3dB}. \tag{1.9}$$

This spacing leads to an undersampling of the telescope field of view, but the physical size of the horn antennas makes closer spacing difficult.

The local oscillator power distribution network has to supply each pixel with an equal amount of power and exhibit low losses. The LO power is distributed with waveguide power dividers or quasioptically with Fourier gratings or dielectric beam splitters. A multiplexing efficiency of 72% has been obtained for a 4-beam system using beam splitters [92]. Fourier gratings reduce the complexity of optics compared to beam splitters at higher pixel numbers and

have typically an efficiency between 80% and 90% [34]. The diplexing of the individual LO-signals with the signal of interest and the coupling to the mixers are often performed with Martin-Puplett interferometers, the operation and imperfections of which are investigated in Chapter 3. Waveguide diplexing is an option at millimeter wave frequencies, while dielectric beam splitters may be used when the amount of LO power is abundant.

1.3 Mixers

The astronomical signals are very weak, and a total amplification in the order of 80 dB is necessary before further signal processing may take place. As mentioned in the previous section, the use of low noise amplifiers is limited to below 180 GHz. The signal is therefore shifted to a lower frequency with a mixer, which can basically be any element exhibiting a nonlinear current-voltage characteristic. When pumped by a local oscillator signal at a frequency f_{LO}, the signals at frequencies $f_s = f_{LO} \pm f_{if}$ are converted to an intermediate frequency $\pm f_{if}$ [78]. The most important mixer types employed in radio astronomy are introduced in this section.

1.3.1 SIS Mixers

Superconductor-insulator-superconductor (SIS) tunnel junction mixers are based on photon assisted tunneling of quasiparticles through a thin insulating layer between two superconducting layers [93]. A niobium-aluminium-oxide-niobium junction is a widely used material configuration. The exploitation of the superconducting properties of the materials requires cryogenic cooling to 4 K or below. Figure 1.3 shows energy band diagrams of a SIS-junction at temperature $T = 0$ K. Quasiparticle energy states up to $E_F - \Delta$ are filled in a superconductor, where E_F is the Fermi energy and Δ half of the binding energy of a cooper pair, the other current carrier in a superconductor. An energy gap of 2Δ separates the filled energy states of a quasiparticle from the empty states; this fact distinguishes a quasiparticle from an electron in a metal. Figure 1.3a illustrates the situation when no external DC voltage is applied across the junction. In Figure 1.3b, a DC voltage of $V = 2\Delta/e$ has caused the filled valence states and the empty conduction states to shift to the same level allowing tunneling current to flow. This is seen as a steep increase in the I–V curve in Figure 1.4. When terahertz radiation is applied to the junction, tunneling may take place with smaller DC voltages (Figure

1.3c). The missing energy is provided by a photon, the energy of which is

$$E = hf = 2\Delta - eV. \tag{1.10}$$

The photon energy may also be higher, but as the density of energy states decreases at higher energies, the tunneling is not that effective. If the energy of one photon is not sufficient, the required energy may be provided by several photons. The current can therefore flow when the following condition is fulfilled

$$E = nhf = (2\Delta - eV)n, \tag{1.11}$$

where n is the number of photons. The first step in the I–V curve below the limiting voltage marks the point where the energy of one photon is sufficient to allow a quasiparticle to tunnel through the insulator, at the next step two photons are required, and so on. Such events become rarer as n increases and the tunneling current is correspondingly smaller.

SIS mixers dominate ground based astronomical single- and multi-pixel heterodyne receivers at frequencies below 1.3 THz [39], [35], but have recently also proven their ability to function on a satellite platform [23]. They require only some microwatts of pump power [81]. Receivers utilizing SIS mixers have demonstrated noise temperatures of few times the quantum limit hf/k (noise caused by quantum vacuum fluctuations) below 0.7 THz and less than 10 times the quantum limit at 1 THz [83].

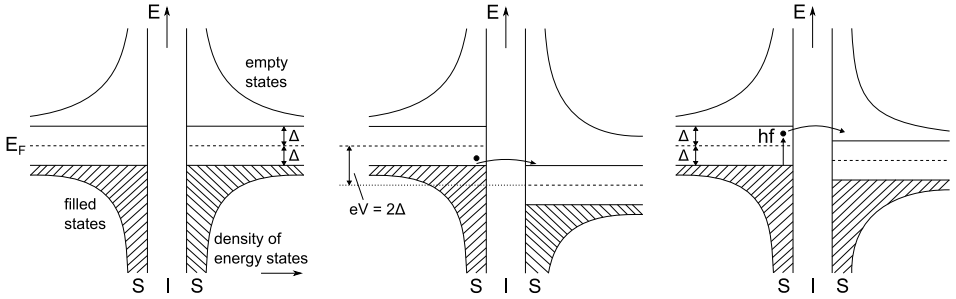

Figure 1.3: (a) $V = 0$, (b) $V = \frac{2\Delta}{e}$, (c) $V = \frac{2\Delta - hf}{e}$.

1.3.2 HEB Mixers

A bolometer can be considered as a temperature dependent resistor [66]. The thermal response time of the bolometer, which is the heat capacity divided by the thermal conductivity, defines how fast the temperature, and

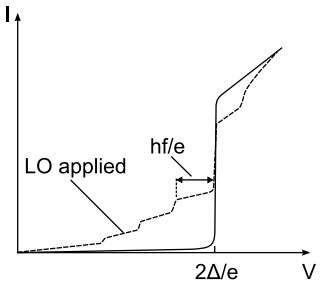

Figure 1.4: The characteristic I–V curve of a SIS junction.

consequently the resistance, of the bolometer can change if the high frequency power heating the bolometer changes suddenly. A bolometer may be able to follow variations in time averaged dissipated power, but not the high frequency field variations.

A hot electron bolometer (HEB) is based on a thin superconductive film which is heated to a temperature near the superconducting transition with a small bias voltage [101]. An electron (quasiparticle) on the film absorbs the energy of an incoming photon and shares it rapidly with other electrons, which causes a small increase in their temperature. Near the transition temperature, this small increase causes the electrical resistance of the bolometer to change strongly. The electrons need to cool down quickly in order achieve a short thermal response time. Cooling is based on electron diffusion to metal contacts at the ends of the film or on phonons (quasiparticles describing quantized lattice vibrations) that exit from the film to the underlying substrate. In the latter case, the thermal conductivity is maximized by selecting a superconductor with a strong electron-phonon interaction such as niobium-nitride and by using very thin films to allow the phonons to exit the film as quickly as possible. The heat capacity is minimized by minimizing the volume of the film.

HEB mixers are able to follow IF signals at frequencies of several GHz and require cryogenic cooling to 4 K and about 1μW LO power [39]. They are employed at frequencies above 1.4 THz, where the sensitivity of SIS mixers starts to degrade rapidly. The noise temperature of HEB mixers is about 10 times the quantum limit below 2.5 THz [83].

1.3.3 Schottky Diode Mixers

The Schottky barrier diode consists of a junction between a metal and a semiconductor (typically gallium arsenide) in which the height of the potential

barrier between the two materials can be controlled by altering the voltage applied across the junction [85]. Figure 1.5a shows the junction between metal and an n-type semiconductor in thermal equilibrium. The light blue area depicts the density of thermionically emitted electrons. The current density from the semiconductor to the metal, or vice versa, is proportional to the electron density. In thermal equilibrium, the electron densities, and therefore the current densities, are equal, which leads to a zero net current. When a positive voltage is applied to the metal (forward bias), the potential barrier decreases accordingly and it becomes easier for the electrons to be emitted from the semiconductor into the metal. Consequently, a net current flows in this direction (Figure 1.5b). When a reverse bias is applied, as in Figure 1.5c, the height of the potential barrier increases and it becomes more difficult for the electrons on the semiconductor side to move into the metal. The current across the junction changes exponentially in respect to the applied voltage, which is manifested by the nonlinear I–V curve.

The advantage of Schottky mixers is that they can be operated at room temperature, although a sensitivity improvement by a factor of 2–4 can be achieved by cooling the receiver [81]. Schottky mixers are 5–10 times less sensitive than the SIS and HEB mixers and require much more LO power. For example, a pump power of 1 mW for a 600-GHz [37] and 5 mW for 2.5-THz mixer [28] at room temperature have been reported. Cooling may reduce the amount of required LO power notably. Schottky mixers have been constructed in a planar form up to 2.5 THz and with a whisker contact up to 4.75 THz [6].

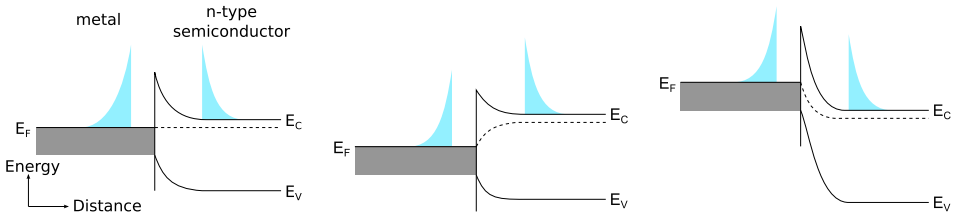

Figure 1.5: Schottky barrier at (a) thermal equilibrium, (b) with a forward bias and (c) with a reverse bias. Adapted from [85].

1.4 Local Oscillator Sources

Important characteristics of a local oscillator include the output power, spectral purity and tunability. The operating voltages, size and lifetime should

also be considered. Figure 1.6 illustrates the output power available from several terahertz region sources. This section introduces briefly the most relevant ones for radio astronomical applications.

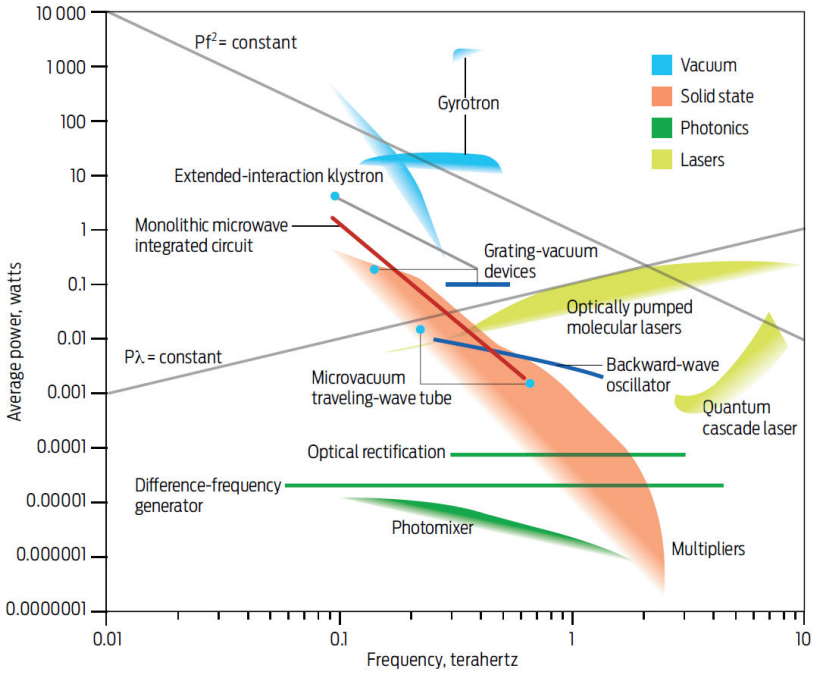

Figure 1.6: Output power of terahertz sources. Image from [3].

1.4.1 Solid state frequency multipliers

Currently the most prominent way to produce LO power at terahertz frequencies is to exploit the nonlinear capacitance of GaAs Schottky barrier diodes to generate harmonic frequency components of the input signal. Multipliers based on nonlinear capacitance (varactors) exhibit a higher efficiency than varistors (nonlinear resistance) and bandwidths of 10–15% [12]. A terahertz multiplier source consists of an electronically tunable microwave synthesizer, the output signal of which is multiplied up to the W-band. A powerful monolithic millimeter wave integrated circuit (MMIC) power amplifier amplifies the signal which is then multiplied again with a series of doublers and triplers up to terahertz frequencies. The conversion efficiency of higher order multipliers has not reached the efficiency of a cascade of lower order multipliers [81]. A powerful solid state frequency multiplier chain providing more than 1 mW at 840–900 GHz has been presented in [62] and very recently the

limits of multiplier technology has been pushed up to 2.75 THz, the record output power being 18 μW at 2.58 THz [61]. Spurious signals at harmonic frequencies reduce the spectral purity of frequency multiplied sources.

1.4.2 Molecular gas lasers

The energy level diagram in Figure 1.7 illustrates the origin of the THz-radiation from an optically pumped molecular gas laser [87], [14]. A resonator containing gas composed of molecules with a permanent dipole moment is excited with an infrared CO_2 pump laser. Molecules are transferred from a certain rotational state of the vibrational ground state into a certain rotational state of an excited vibrational state. The energy of the photons from the CO_2 laser must match the energy required for this transition. Laser emission is obtained when molecules in the excited vibrational state are transferred into a rotational state with smaller energy. The frequency of the emitted radiation depends on the energy difference of the rotational states and can thus be changed by selecting another spectral line or by changing the gas. Although not continuously tunable, there are many suitable gases in the submillimeter region, the average distance between emission frequencies being 10–20 GHz. Molecular gas lasers exhibit a high spectral purity and provide power from microwatts to several hundred milliwatts, the typical output power being some milliwatts. They are, however, large and heavy devices, altough efforts towards more compact configurations have been made: a molecular gas laser for aircraft environment with a weight of 45 kg and a size of 200×235×1000 mm^3 is presented in [40]. A 2.5-THz molecular gas laser LO has also been used in a satellite-based instrument [69].

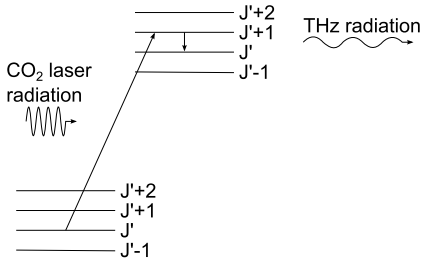

Figure 1.7: Energy level diagram of an optically pumped molecular gas laser.

1.4.3 Photomixers

Frequency downconversion from optical wavelengths using photomixers can be exploited to generate terahertz power [9],[10]. Two continuous-wave lasers operating at slightly different frequencies are focused onto the surface of a photoconductor, which is typically fabricated from low-temperature-grown GaAs. An incoming photon excites an electron from the valence band to the conduction band if its energy is higher than the energy gap between the bands. This creates an electron-hole pair with a subpicosecond lifetime. The increase in the number of carriers increases the conductivity of the photoconductor, so the conductivity is proportional to the absorbed optical power. The absorbed optical power contains a DC-component, components at optical frequencies and a component at the sum and at the difference frequency. When an external bias voltage is applied across the photoconductor, the charges create a photocurrent proportional to the conductivity. The response time of the carriers even in the fastest photoconductors is too long with respect to the power variations at the optical or sum frequencies. Instead, the conductivity varies at the difference frequency and causes the modulation of the photocurrent. Photomixer based local oscillators are able to provide an output power of around 1 μW at 1 THz and can be tuned over a whole waveguide band by tuning the wavelengths of the lasers. The output spectrum does not have harmonic content, and very narrow linewidths may be obtained [65].

1.4.4 Quantum cascade lasers

The radiation from a quantum cascade laser (QCL) is produced as electrons undergo an intersubband transition in the conduction band of a heterostructure [27]. The subbands arise in quantum wells due to quantum confinement. The heterostructure, and consequently the quantum wells, are realized by growing nanometer-thick alternating layers of GaAs and AlGaAs with molecular-beam epitaxy. The radiative transition between two subbands, and thus the emission wavelength, is selected by engineering the layers to the desired thicknesses and by applying a suitable bias voltage. The structure is periodic, and each unit contains an active as well as an injector region, as depicted schematically in Figure 1.8. A terahertz photon is emitted when an electron makes a transition from the upper radiative state 3 to the lower radiative state 2. Then the electron relaxes rapidly to state 1 and tunnels through the injector to the state 3 of the next unit, where the process is repeated. Suitable design of the heterostructure ensures that the electron

lifetime at state 2 is shorter than at state 3, which leads to a population inversion. Continuous wave operation of terahertz QCLs has been reported between 1.2 THz and 4.9 THz at temperatures below 120 K [94]. An output power of 138 mW has been reached at 4.4 THz, but below 2 THz the obtained output power levels are lower than 1 mW. The single mode frequency tuning range is typically limited to 10–20 GHz, but new methods to allow a broader tuning range are being investigated [12]. The spectral purity of a QCL may suffer from frequency drift and short term instabilities [40].

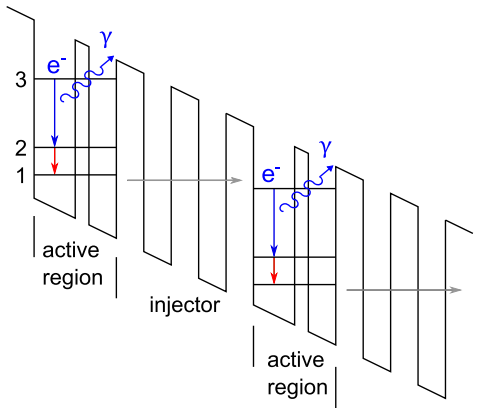

Figure 1.8: Schematic conduction band energy diagram of a quantum cascade laser. Two units, consisting of an active region and an injector, are shown. The radiative transition is shown in blue.

1.5 Limitations of Current Technology

Assuming that a cryogenically cooled solid state frequency multiplier is used to provide a pump power of P_{LO} [12], Table 1.1 presents the maximum number of pixels in a heterodyne array receiver. It is assumed that half of the pump power reaches the mixers and that the power requirements for Schottky, SIS and HEB mixers are 1 mW, 10 μW and 1 μW, respectively. The number of pixels is seriously restricted by the available pump power especially above 1 THz. The maximum pixel number in an array receiver realized so far is 32 in the millimeter region and 16 in the terahertz region [35], while a 64-pixel receiver is being developed [46].

The concept of using traveling wave tube amplifiers for the LO-signal amplification has been proposed in [25]. The next chapter presents several design and development aspects of two vacuum electronic terahertz amplifiers that

are suitable for this task. The improvement of the diplexing efficiency of a Martin-Puplett interferometer is then addressed in the succeeding chapter. These developments represent a step towards array receivers with even larger pixel numbers.

Table 1.1: Maximum number of pixels in a heterodyne array receiver driven by a solid state frequency multiplier.

f [GHz]	P_{LO} [μW]	Schottky	SIS	HEB
900	2000	1	100	1000
1350	100	0	5	50
1800	50	0	2	25

2 TERAHERTZ AMPLIFIER

2.1 Introduction to Traveling Wave Tubes

Figure 2.1 presents the main parts of a traveling wave tube. The electrons are emitted from a cathode ideally providing high current density and a long lifetime. The electrons are electrostatically compressed into an electron beam and accelerated by a voltage V_b, applied between the cathode and the anode, to a velocity

$$v_0 = \sqrt{\frac{2V_b e}{m_e}} = 0.593 \cdot 10^{-6}\sqrt{V_b}, \tag{2.1}$$

where e is the elementary charge and m_e is the mass of the electron. A typical velocity is around $0.20c$, so an accelerating voltage close to 10 kV is needed. A static axial magnetic field in the slow wave structure region is used to prevent the electron beam (e-beam) from dispersing due to repulsive forces between the electrons: any transverse motion causes an electron to start rotating as dictated by the Lorentz force,

$$\vec{F} = q(\vec{E} + \vec{v} \times \vec{B}). \tag{2.2}$$

The Brillouin field is the minimum magnetic field that balances the transverse repulsive force due to space charge and the inward force caused by the magnetic field in the electron beam [30],

$$B_{Br} = 8.302 \cdot 10^{-4} \frac{|I_b|^{1/2}}{V_b^{1/4} r_b}, \tag{2.3}$$

where I_b is the beam current and r_b the electron beam radius. Typically the focusing magnetic field is selected to be about twice B_{Br} and created with permanent magnets made of rare-earth alloys, primarily samarium cobalt (SmCo) or neodymium (NdFeB), since a magnetic field near 1 T is required at terahertz frequencies. The radiofrequency wave (RF-wave) enters the amplifier near the anode through an input coupler and is fed to the slow wave

structure. The wave and the electron beam are able to interact as long as their velocities are approximately equal. The amplification of the wave takes place at the expense of the kinetic energy of the electrons, and thus, at some point, the velocity synchronism between the electrons and the wave breaks down, and no further amplification is possible. The RF-wave is then coupled out of the device and the electrons are gathered at the collector. The collector is usually in a lower potential than the body of the tube, or depressed, in order to reduce the velocity of the electrons and consequently the energy converted to heat when the electrons collide with the collector walls. This allows high efficiencies to be obtained, especially when multiple depression stages are utilized [48].

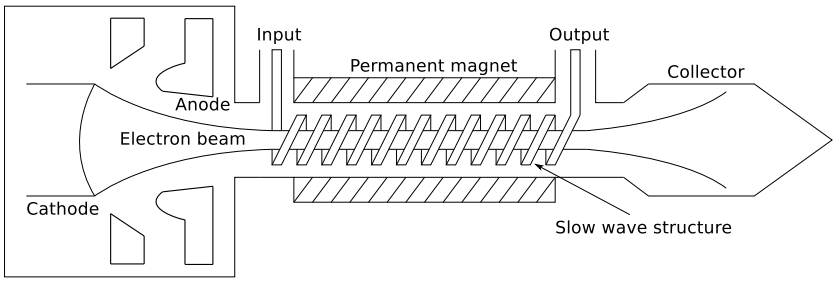

Figure 2.1: Main parts of a traveling wave tube. Adapted from [4].

An electron entering the slow wave structure experiences an accelerating or decelerating force depending on the phase of the axial component of the electric field caused by the input signal. The phase velocities of the electron and the wave are approximately equal which leads to continuous interaction between them. The trajectories of three electrons in a coordinate system moving at the wave velocity are illustrated in Figure 2.2a. An electron bunch starts to form between the accelerating and decelerating field regions. Velocity modulation leads therefore simultaneously to density and current modulation. The modulated electron beam current then acts as a source of electromagnetic fields. The slow wave structure sets the boundary conditions of the Maxwell's equations. The induced field is such that the electron bunches are located in decelerating regions, and the kinetic energy lost by the electrons via radiation is transferred to the electromagnetic energy of the wave. The electron velocity is adjusted to be slightly higher than the phase velocity of the wave in practice, which results in electron bunch formation within a decelerating field region, as shown in Figure 2.2b.

A helix is a very widespread slow wave structure due to the unmatched bandwidth it is able to provide (Figure 2.3a). At microwave frequencies, traveling wave tubes with bandwidths over 2.5 octaves have been demonstrated [4].

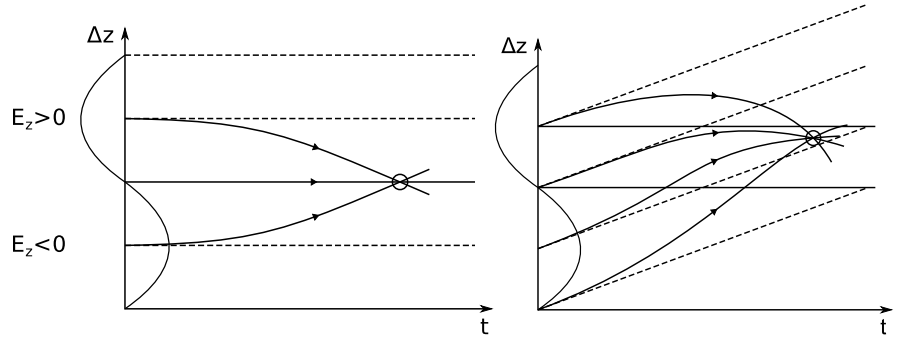

Figure 2.2: Bunching of electrons due to an axial electric field E_z: (a) $v_e = v_p$, (b) $v_e > v_p$. Adapted from [72].

However, any other structure that slows down the electromagnetic wave in such a way that approximate synchronism with the electron beam can be achieved and that creates an axial electric field component can be used to realize a traveling wave tube. Especially the folded waveguide slow wave structure (Figure 2.3b) has been under intense research by groups targering operation at millimeter and terahertz frequencies [7], [29]. It may provide a bandwidth of 20–30% and is also compatible with microfabrication. Very recently, a power module containing a solid state driver and a folded waveguide TWT has been reported to produce a pulsed output power of over 100 mW at 0.656 THz [88]. A coupled cavity structure (Figure 2.3c) is used in high-power TWTs, but its bandwidth is typically limited to 10–15%. A review of terahertz vacuum electron devices in general is given in [8].

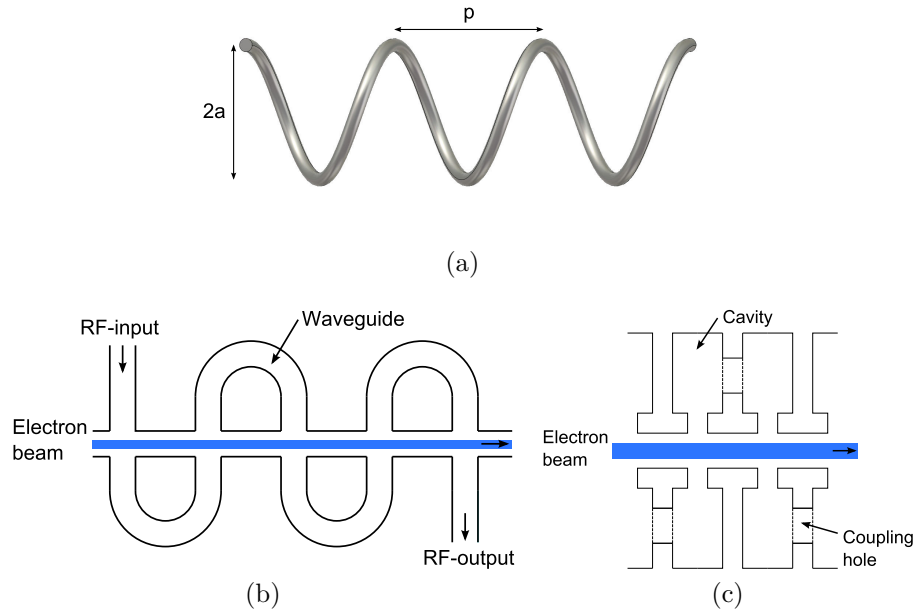

Figure 2.3: Slow wave structures: (a) a helix, (b) a folded waveguide and (c) a coupled cavity structure.

2.2 Square Helix Traveling Wave Tube

The extraordinary bandwidth makes the helix very interesting among the slow wave structures also at terahertz frequencies. Microwave and millimeter wave helices are wound from a metal wire, but as the size of the SWS changes inversely proportional to the frequency, such an approach cannot be taken at terahertz frequencies, where the helix diameter is only tens of micrometers. This section introduces a square geometry that makes the realization of a helix SWS with microfabrication methods more feasible. A W-band realization of a similar structure is presented in [18], while a terahertz backward wave oscillator based on a microfabricated helix is discussed in [21] and [22]. A ring-bar helix SWS, originally devised for suppressing backward wave oscillations in a conventional helix TWT at higher power levels, is also attractive from the microfabrication point of view [17]. However, the phase velocity on the ring-bar helix is higher and the bandwidth is narrower, about 10–20% in the microwave region [31].

The design principles of a circular helix are applied to estimate the size of the square helix. An eigenmode simulation is then used to find out the cold parameters, dispersion, interaction impedance and attenuation, which allow the small-signal gain to be computed from the Pierce theory (e.g. [31]). Suitable input/output couplers are designed and the influence of the mesh on the axial wavelength and scattering parameters of the structure in the absence of the electron beam are investigated. Finally, an electron beam is introduced to obtain the gain over frequency and the output power as a function of input power. All the simulations were carried out with CST Microwave Studio and CST Particle Studio, which solve the Maxwell's and Newton's equations in the real 3D structure. Nonlinear behavior near saturation, reflections due to input/output coupler mismatches and electron beam dynamics are therefore included in the simulations.

This chapter is based on the work published in [51] and [50].

2.2.1 Slow Wave Structure Design

The radius of a helix, see Figure 2.3a, is usually determined by the normalized radial propagation constant γa:

$$\gamma a = \left(\beta^2 - k^2\right)^{\frac{1}{2}} a = 2\pi f \left(\frac{1}{v_p^2} - \frac{1}{c^2}\right)^{1/2} a \approx \frac{2\pi f}{v_p} a, \tag{2.4}$$

where a is the helix radius, $\beta = \omega/v_p$ the axial propagation constant in the helix, $k = \omega/c$ the free space wavenumber and v_p the phase velocity. The last approximation follows from the assumption $v_p^2 \ll c^2$. The normalized radial propagation constant is typically in the range between 1.0–1.7. Values in the lower end of the range are useful at microwave frequencies for keeping the size of the helix small. A disadvantage is increased harmonic distortion of the signal. In order to make the manufacturing of the helix less difficult and to allow enough space for the electron beam, a high γa-value is required at terahertz frequencies. This leads to a reduced interaction impedance and efficiency. If the normalized radial wavelength is too high, the operating frequency may lie in the stop band of the helix and no wave propagation is possible. The use of γa as the design parameter is related to the fact that the axial electric field inside the helix varies in the radial direction as $I_0(\gamma r)$, where I_0 is the 0th order modified Bessel function of the first kind and r the distance from the axis [4]. In order to minimize the field variation across the beam, it is desirable to keep γa below 1.5.

An electromagnetic wave propagates along a conducting wire with the speed of light. When the wire is wound into a helix, the time needed for the signal to propagate one winding is the same as the time used by an axial wave to propagate a distance p,

$$t = \frac{2\pi\sqrt{a^2 + \left(\frac{p}{2\pi}\right)^2}}{c} = \frac{p}{v_p}. \tag{2.5}$$

The equation is solved for the pitch p, giving

$$p = \frac{2\pi a}{\sqrt{\left(\frac{c}{v_p}\right)^2 - 1}}. \tag{2.6}$$

After the operating frequency and the beam voltage have been selected, the radius and pitch of the helix may be computed by assuming velocity synchronism between the electrons and the wave, $v_p = v_e$.

Unfortunately, a circular helix shape poses a manufacturing problem at terahertz frequencies, at which microfabrication methods are needed due to extremely small structure dimensions. In order to make the structure more microfabrication compliant, a square shape has been adopted. The geometry is motivated by [24] which describes a process to fabricate smooth walled copper pillars with through-mold electrodeposition (Figure 2.4). The dimensions of the square helix have been limited to roughly correspond with the capabilities of this fabrication method: a pillar height of 25 µm, a diameter of 5 µm and a minimum pitch of 25 µm have been demonstrated.

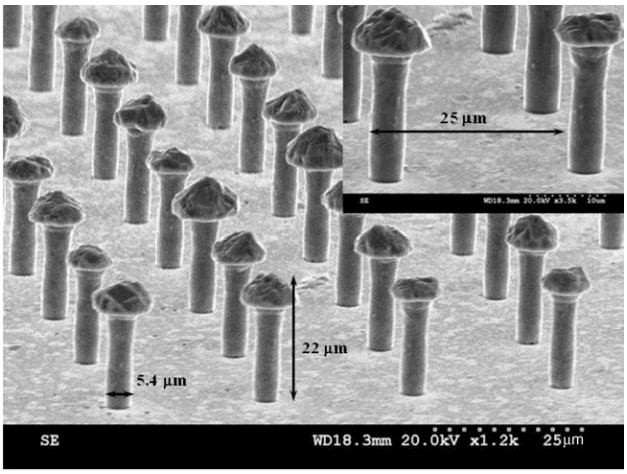

Figure 2.4: Copper interconnects from [24].

One period of the square helix SWS is shown in Figure 2.5. The material of the helix is copper, and it stands on a quartz substrate. The size of the square helix, l, is determined by setting the circumferences of both helix types, square and circular, equal while keeping the pitch constant:

$$2l + 2\sqrt{l^2 + \left(\frac{p}{2}\right)^2} = 2\pi\sqrt{a^2 + \left(\frac{p}{2\pi}\right)^2}. \tag{2.7}$$

The dimensions of a helix SWS designed for 825 GHz by using a γa of 1.5 and a beam voltage of 10 kV are given in Table 2.1.

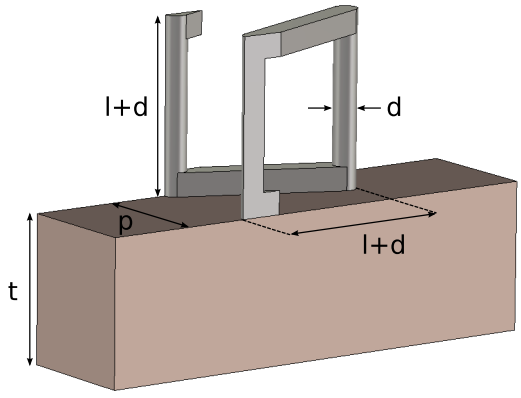

Figure 2.5: One period of a square helix slow wave structure and the related dimensions.

Table 2.1: Dimensions of the square helix SWS.

d [µm]	l [µm]	p [µm]	t [µm]
4	30	22	25

2.2.2 Eigenmode Simulation

One square helix SWS period with a pitch p is modeled. Periodic boundary conditions in the axial direction and a phase advance, $\phi = \beta_0 p$, for a wave propagating through the structure are defined. The eigenmode solver then treats the structure as a resonator and calculates eigenmode (resonance) frequencies as well as the electromagnetic fields in the simulation domain. The results allow the calculation of the phase velocity,

$$v_p = \frac{2\pi f}{\beta_0}, \tag{2.8}$$

the on-axis interaction impedance [30], which is a measure for the interaction strength between the electron beam and the wave and is related to the obtainable gain,

$$K_0 = \frac{|E_{z0,axis}|^2}{2\beta_0^2 P_{rf}}, \tag{2.9}$$

and the attenuation [79],

$$\alpha = \frac{\omega}{2Q v_g}. \tag{2.10}$$

Here, β_0 is the propagation constant of the wave in the absence of the electron beam, $E_{z0,axis}$ the axial electric field, P_{rf} the total RF power flow along the circuit, Q the unloaded Q-factor, which is a measure for the circuit quality from the point of view of losses, and v_g the group velocity. The subscript zero indicates that we are considering the fundamental space harmonic. It has been shown in [47] that 3D electromagnetic simulators, a comparison of which is presented in [1], are able to yield more accurate interaction impedance predictions than conventional measurement methods which involve perturbation of fields with a dielectric rod inserted inside the helix. At terahertz frequencies such a measurement approach is not even feasible due to the small structure size. The conductivity of copper is halved to $2.9 \cdot 10^7$ S/m in order to model the effect of surface roughness at high frequencies.

The simulated cold parameters for three different helix diameters are shown in Figure 2.6. On the one hand, a large helix diameter is desired in order to

relax the electron beam focusing requirements, but on the other hand, the size of the helix limits the maximal operating frequency, as shown in Figure 2.6a: the cutoff shifts towards lower frequencies as the diameter increases. At the same time, the interaction impedance decreases and the loss per period increases at the target frequency. As seen from (2.10), the rapid increase in losses near the cutoff is caused by the decreasing group velocity. A change of the helix pitch affects all parameters, but to a smaller extent than a similar change of the diameter. The dashed line in the dispersion plot, Figure 2.6a, is the beam line and represents the velocity of the electrons that have been accelerated by a voltage of 10560 V. The intersection of the beam line and the dispersion curve marks the point where the electrons and the wave obtain velocity synchronism and thus defines the nominal frequency of operation. The operating point can be tuned by changing the beam voltage. For the helix with a diameter of 26 μm the operating point is at a frequency of 825 GHz. The beam line and the dispersion curve intersect in a very small angle, which is an indication of a broad instantaneous bandwidth. The main information from Figure 2.6 concerning the helix with a diameter of 26 μm is summarized in Table 2.2.

Table 2.2: Summary of cold parameters.

Frequency, f	825 GHz
Normalized phase shift, ϕ	0.60
Propagation constant, β_0	85109 m^{-1}
Axial wavelength, λ_z	73.8 μm
Periods per wavelength, N	3.4
Beam voltage, V_b	10560 V
Electron velocity, v_e	0.20c
Interaction impedance, K_0	59 Ohm
Attenuation per period, α	0.13 dB

Small-Signal Gain

The slow wave structure is often modeled as a transmission line having a certain characteristic impedance (interaction impedance) and certain dispersion properties [30], [31]. The electron beam induces image currents onto the circuit which act as a source for a growing wave. The circuit voltage, on the other hand, is related to the axial electric field which interacts with the electron beam via Newton's second law. The continuity equation completes

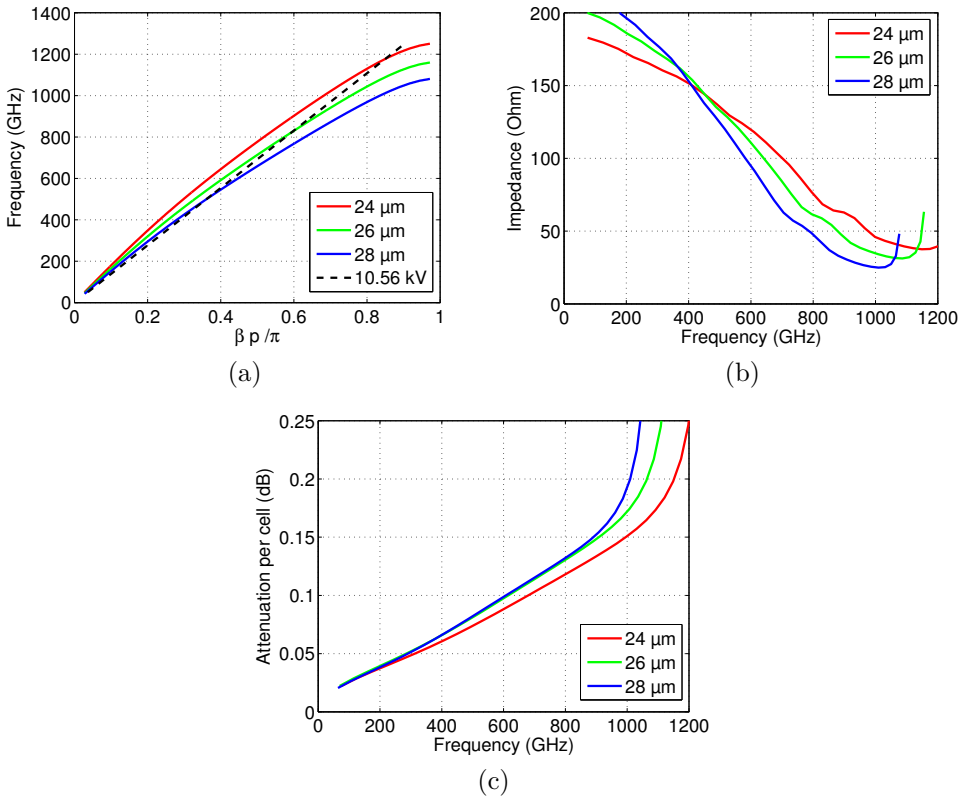

Figure 2.6: Cold parameters of the square helix slow wave structure for several helix diameters l: (a) dispersion, (b) interaction impedance and (c) attenuation.

the TWT interaction model. Alternatively, a more realistic, but mathematically more complicated, model involves the calculation of the electromagnetic fields from Maxwell's equations, the boundary conditions for which are given by the geometry of the slow wave structure [16]. An analytic solution to the transmission line model exits in the small-signal region, where the current density, charge density and velocity of the electron beam may be expressed as a sum of a constant DC-component and a small time-harmonic AC-component. The three solutions of a third order characteristic equation,

$$\delta^2 = \frac{1}{j\delta - b + jd} - 4QC, \tag{2.11}$$

are related to complex propagation constants of traveling waves in the beam-circuit coupled system through the following definition:

$$\Gamma \equiv j\beta_e \left(1 + jC\delta\right), \tag{2.12}$$

where β_e is the electron beam propagation constant $\beta_e = \omega/v_e$. The three solutions correspond to an exponentially growing wave, an exponentially decaying wave and a wave with a constant amplitude. The exponentially growing wave is responsible for the amplification in a traveling wave tube. The small-signal gain parameter C is defined as

$$C = \left(\frac{I_b K_0}{4V_b}\right)^{1/3}. \tag{2.13}$$

The cold velocity detuning parameter b in (2.11),

$$b = \frac{v_e - v_p}{Cv_p}, \tag{2.14}$$

is useful for characterizing the relation between the difference in the phase velocities of the e-beam and the wave and the growth rate of the wave. The effect of space-charge forces is characterized through the parameter

$$QC = \frac{\omega_q^2}{4C^2\omega^2}, \tag{2.15}$$

where the reduced plasma frequency in the electron beam is

$$\omega_q = F\omega_p = F\sqrt{\frac{\eta\rho_c}{\epsilon_0}}, \tag{2.16}$$

where F is the plasma frequency reduction factor introduced for finite electrons beams, ω_p the plasma frequency, η the electron charge-to-mass ratio,

ρ_c the DC charge density of the electron beam and ϵ_0 the permittivity of free space. The plasma frequency reduction factor originates from the fact that the electric field of the space-charge in a finite electron beam has a transverse component producing fringing fields that do not take part in the bunching process. In the case of a solid cylindrical electron beam inside a circular waveguide, the reduction factor may be computed from the equation

$$F = \frac{-0.7287\left(\frac{r_b}{r_a}\right) + 1.3659}{\sqrt{1 + \frac{2.2290}{(\beta_e r_b)^2}}}, \tag{2.17}$$

where r_a and r_b are the waveguide and beam radii, respectively [56]. An expression for the reduction factor has been derived also in the case where the helix is not considered as a solid conducting wall [2]. The attenuation in the circuit is described by the loss parameter

$$d = \frac{\alpha}{\beta_e C}, \tag{2.18}$$

where α is the loss per unit wavelength. The small-signal gain in decibels is

$$G = A_1 + A_2 + BCN, \tag{2.19}$$

where the initial loss factor is

$$A_1 = 20\log_{10}\left|\frac{\delta_1^2}{(\delta_1 - \delta_2)(\delta_1 - \delta_3)}\right|, \tag{2.20}$$

the space charge loss factor is

$$A_2 = 20\log_{10}\left|\frac{\delta_1^2 + 4QC}{\delta_1^2}\right|, \tag{2.21}$$

and the growing wave parameter is

$$B = 54.6\,\mathrm{Re}\,(\delta_1)\,. \tag{2.22}$$

The real part of δ_1 describes the growth rate of the growing wave. N is the number of electronic wavelengths on the circuit

$$N = \frac{\beta_e l}{2\pi}, \tag{2.23}$$

where l is the length of the slow wave structure. Using a beam voltage of 10560 V, a beam current of 2.7 mA and the simulated dispersion and loss characteristics from Figure 2.6, the small-signal gain computed from

(2.19) for a 4.7 mm long interaction structure is plotted in Figure 2.7a. It also presents the gain calculated with the multifrequency spectral Eulerian (MUSE) model of the free software package LMSuite [95]. The MUSE-model is also based on the transmission line description and as the application at hand does not need the advanced multifrequency properties of the model, it is not surprising that the results are in good agreement. However, a comparison with Figure 2.15b shows these predictions to deviate considerably from the results of 3D particle-in-cell (PIC) simulations.

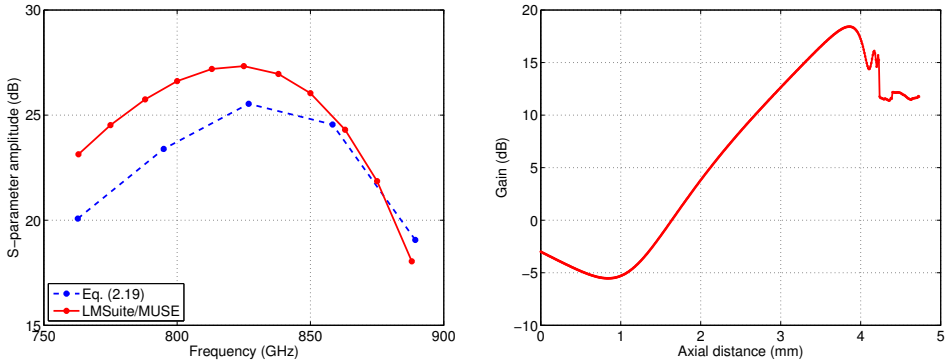

(a) (b)

Figure 2.7: (a) Small-signal gain (Pierce-theory and MUSE), (b) gain as a function of the interaction structure length (LATTE).

The Eulerian fluid model of MUSE is not able to describe electron overtaking, which is a requirement for the saturation behavior prediction. However, the LMSuite package includes the LATTE model that takes a Lagrangian approach for modeling the electron beam. The LATTE model predicts a maximum saturated gain of 18 dB for a 3.9 mm long interaction structure at 825 GHz when an input power of -3 dBm is used (Figure 2.7b). PIC simulation results do not show signs of saturation for the same e-beam and input signal configuration even at 4.7 mm. Due to the huge amount of computing time required for PIC simulations, a quicker method for approximating the performance of a designed tube would be desirable. Unfortunately, in the case of the square helix, the accuracy of the Pierce theory or the LMsuite are not sufficient, although the potential of LMSuite should be investigated further. Aside from the fact that the transmission line model is one dimensional, several other error sources can be identified: the losses in the eigenmode simulation are calculated with the perturbation method [78], the plasma frequency reduction factor is calculated for an electron beam inside a conducting cylinder and an on-axis interaction impedance is used instead calculating an average value over the cross-section of the e-beam.

Nevertheless, (2.13) and (2.19) show that higher gain may be obtained by increasing the length of the interaction structure and by maximizing the interaction impedance and the beam current while minimizing the beam voltage. Naturally, saturation prevents the gain from being increased infinitely by making the structure longer, as shown by the LATTE simulation. A high interaction impedance is obtained by placing the electron beam in a region of strong axial electric field. As seen from (2.3), a higher beam current for a fixed beam radius requires a stronger magnetic focusing field. A viable way for creating very uniform magnetic fields in the excess of 1 T with rare-earth permanent magnets is to utilize magic spheres [59]. The magnetic field is created inside a cavity in the center of the sphere, and although no theoretical upper limit is predicted for the field amplitude in this configuration, the size and weight of the magnet may increase to unpractical dimensions. Figure 2.8 illustrates the dependence of the magnetic field strength and the magnet mass on the radius of the magnet. Reference [22] suggests a configuration, where the electron beam propagates on top of the helix rather than in the center of it. The configuration allows a bigger beam diameter and a higher beam current for the same magnetic field when compared to the conventional approach.

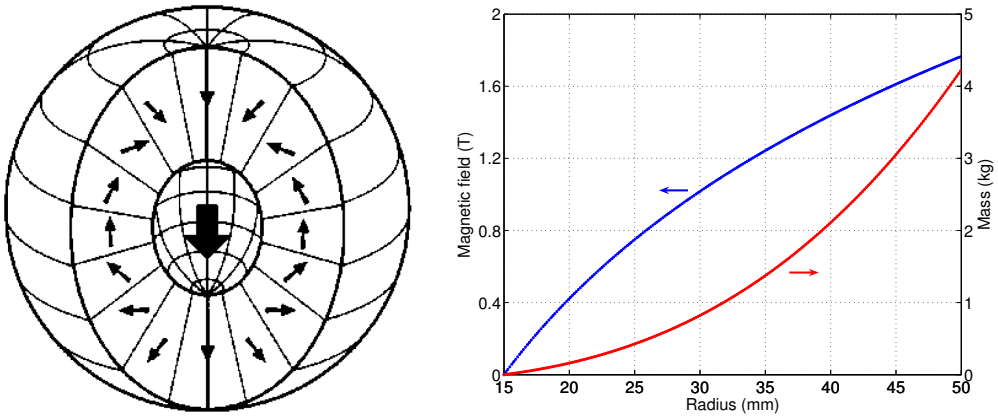

(a) (b)

Figure 2.8: (a) Magic sphere from [59] and (b) its magnetic field and mass as a function of the outer radius. A cavity radius of 15 mm is assumed.

2.2.3 Input/Output Couplers

A coupling structure is needed at both ends of the slow wave structure for guiding the input signal to the helix and the amplified signal out of the helix

with as small losses as possible. Additionally, the coupling structure is not allowed to block the electron beam. The electric field is directed radially in the vicinity of the helix wire, like the field of a TEM mode in a coaxial line (Figure 2.9a), and thus a transition to a coplanar waveguide (CPW) is a natural choice (Figure 2.9b). The ground planes appear from the side walls of the enclosure surrounding the helix and the wire forming the helix becomes the center conductor of the CPW. The ground planes and the center conductor are tapered linearly until the desired widths are attained.

A waveguide interface allows signal coupling to other terahertz components or devices, and therefore a second transition from the CPW to a rectangular WR-1.2 waveguide (305 µm × 152 µm) is included in the coupling structure. The transition is realized using either a post [82], a patch [60] or a ridge [20],[76]. Each alternative is illustrated in Figure 2.10.

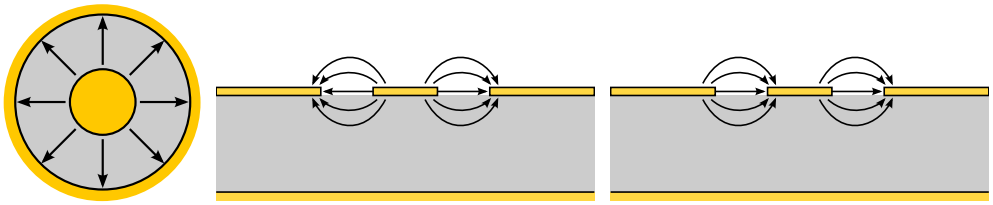

(a) (b) (c)

Figure 2.9: Electric field patterns of (a) a TEM mode in a coaxial line, (b) coplanar waveguide mode of the CPW (odd mode), (c) coupled slotline mode of the CPW (even mode).

The post in Figure 2.10a is connected to the center conductor of the CPW. The substrate is embedded in the waveguide so that the metallization of the CPW is on the same level as the waveguide ceiling. The post penetrates the substrate and enters the waveguide through the center of the broad wall. The length of the post, 93 µm, and the distance to the waveguide end (short circuit), 35 µm, are selected to maximize the return loss at 825 GHz. The symmetry of the transition ensures that the excitation of the undesired coupled slotline mode of the CPW (Figure 2.9c) is weak. Coupling to a parasitic parallel plate mode (fields concentrated in the substrate) is prevented by employing vias. This is also done in the case of the other two transitions. The simulated S-parameters of the coupler in a back-to-back configuration, with two helix periods included, are shown in Figure 2.10b. The bandwidth is here defined as the frequency range, within which $S_{11} < -15$ dB. In this case, the bandwidth is 50 GHz (6%), and the insertion loss at 825 GHz is 1.0 dB .

The E-plane patch probe is visualized in Figure 2.10c. It is a planar probe

which makes it the most appealing from the manufacturing point of view. The face of the patch probe points to the side wall of the waveguide, but the transitions works almost as well when the waveguide is aligned so that the patch faces the waveguide port (marked in red). Strong coupling to the coupled slotline mode takes place at frequencies above 820 GHz, which can be reduced about 15 dB by connecting the ground planes of the coplanar waveguide with an air bridge. The back-to-back S-parameters in Figure 2.10d exhibit broadband performance. The bandwidth is over 144 GHz (17%), and the insertion loss at 825 GHz is 1.2 dB.

The third transition in Figure 2.10e is based on a ridge waveguide. The ridge has a cosine-type profile. The use of a linear profile requires substantial modification of the configuration before good performance can be achieved. The fabrication of the transition is more demanding than that of the two other types. However, due to the symmetry, a cumbersome air bridge is not necessary. Figure 2.10f shows the S-parameters: when only the region around 825 GHz is considered, the bandwidth is 70 GHz (8%), and the insertion loss at 825 GHz is 1.4 dB.

The patch- and ridge-couplers would allow the helix slow wave structure to be used in fuller potential, but unfortunately the exploitation of these coupling structures in the simulations of a complete traveling wave tube led to oscillations. The reason for the instability, whether physical or computational, is still unknown. The traveling wave tube simulations presented below are therefore based on the post-coupler.

2.2.4 Cold Simulations

A square helix traveling wave tube with 215 periods and post-couplers at the input and output is illustrated in Figure 2.11. The simulation domain surrounding the structure is filled with a perfect electric conductor material. The structure width w may be larger through the use of a wider substrate to allow easier manufacturing, but it is limited in the simulation in order to shorten the computing time. The fields on the helix SWS, however, are not affected by this change.

Figure 2.12a shows a snapshot of the electric vector field on a cut plane through the center of the helix. The amplitude of the axial field component is four times greater than the transverse component on the helix axis and 2.5 times greater at the distance of the e-beam radius (see next section). The on-axis wavelength of the axial electric field at 825 GHz is calculated for several mesh settings. A helix is meshed with a local mesh, the grid lines

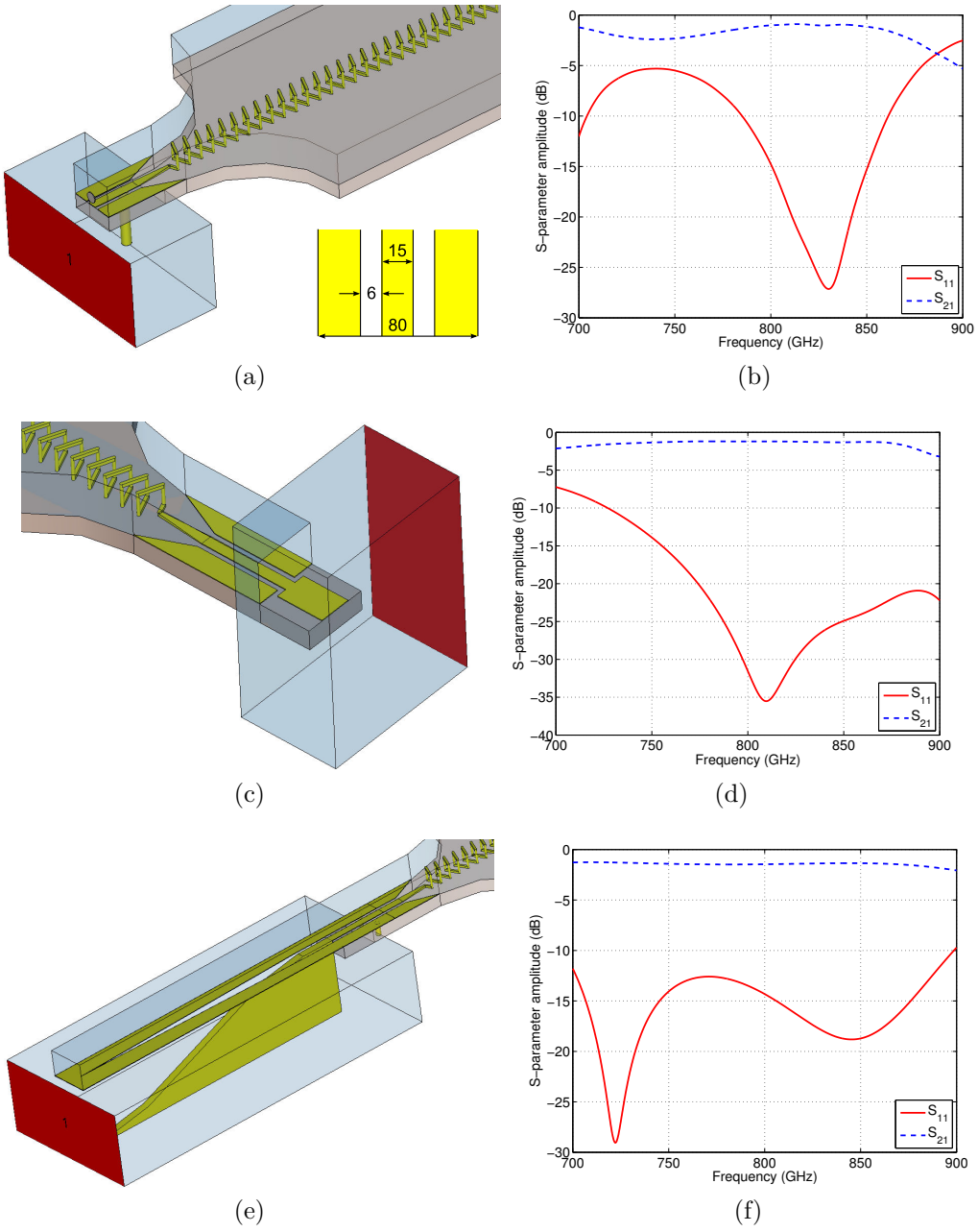

Figure 2.10: Coupling structures for the square helix SWS: (a) post-coupler, (c) patch-coupler and (e) ridge-coupler. The corresponding simulated S-parameters in back-to-back configuration are shown on the right. The inset at the lower right corner of panel (a) shows the dimensions of the coplanar waveguide in micrometers.

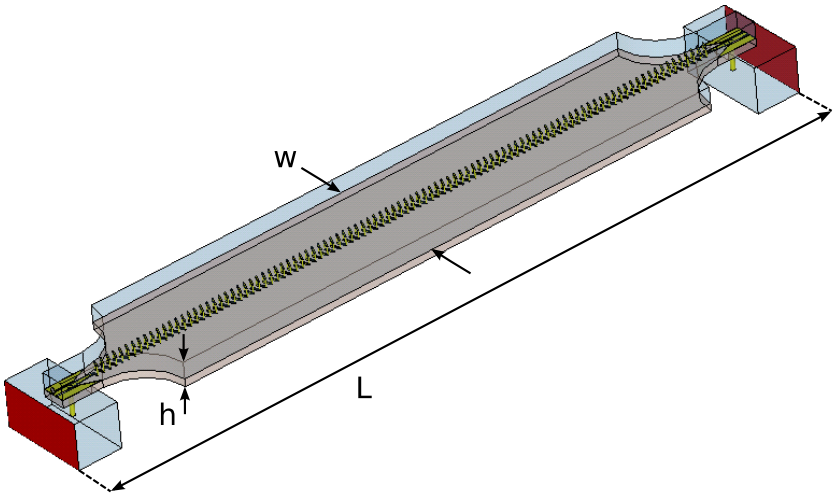

Figure 2.11: A traveling wave tube with post-couplers. The dimensions are $h = 0.08$ mm, $L = 5.1$ mm and $w = 0.4$ mm for a tube with 215 SWS periods (the actual number in this figure is smaller).

of which have a distance $p/(2N_m)$ in transversal direction and p/N_m in the axial direction. The parameter N_m therefore defines the number of mesh cells per helix period in the axial direction. The density of the mesh outside the helix region is set by the parameter m which defines the minimum number of grid lines per wavelength for the highest frequency used in the simulation. The axial wavelength is not constant for the whole helix length, but varies about ± 2 µm from one wavelength to another. Figure 2.12b indicates that as long as $N_m \geq 8$ and $m \geq 22$ these parameters have only a small effect on the wavelength. The mean wavelength is about 70 µm, or about 3.5 µm less than in the eigenmode simulation. The simulator does not completely prioritize the local mesh over the global mesh, and therefore also the parameter m has an effect on the wavelength.

The dependence of S-parameters on the mesh parameters is illustrated in Figure 2.13. The parameter m does not have significant effect on the loss for values greater than 19. Although axial wavelength was not affected by N_m for values over 6, the losses increase notably.

2.2.5 Particle-In-Cell Simulation

Mesh parameters are set to $N_m = 8$ and $m = 22$ in order to reduce the time required for particle-in-cell simulation runs. These settings allow one data point to be obtained in about 30 hours with an Intel CORE i7 970 worksta-

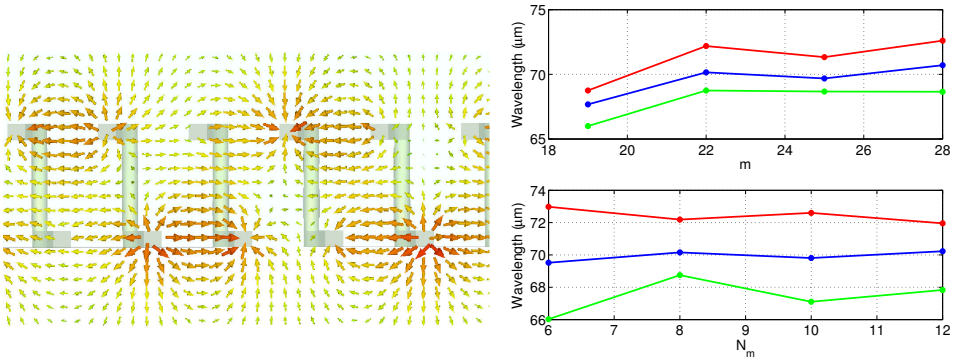

(a) (b)

Figure 2.12: (a) The electric field of the square helix SWS, (b) the effect of mesh parameters on the axial wavelength. Red is the maximum, blue is the mean and green is the minimum wavelength found along the helix SWS.

tion. The conductivity losses are underestimated because of the mesh, but as the choice of the copper conductivity is rather pessimistic (reduced by a factor of 2 to $2.9 \cdot 10^7$ S/m), a realistic gain prediction is, nevertheless, expected. A cylindrical electron beam is introduced at the input end of the tube. The electron gun is not modeled, but an emitting surface, visible as a gray disc in Figure 2.14, with the diameter of the e-beam is used. No initial transverse velocities are taken into account. The dispersive space-charge forces in the electron beam are countered with a uniform magnetic focusing field that fills the simulation domain. The field strength is approximately two times the Brillouin field given by (2.3).

The deviation of the axial wavelength from the prediction given by the eigenmode simulation necessitates a change of the beam voltage. The phase velocity of the wave is given by

$$v_p = \lambda_z f, \tag{2.24}$$

where λ_z is the axial wavelength and f the frequency. Requiring velocity synchronism, the beam voltage corresponding to v_p is obtained from (2.1). For a frequency of 825 GHz and a wavelength of 70 µm, the beam voltage is about 9500 V. A beam voltage sweep in Figure 2.15a shows that the voltage maximizing the gain is 9650 V.

Small-signal gain as a function of frequency for the parameters given in Table 2.3 is plotted in Figure 2.15b. A maximum gain of 18.3 dB is achieved at the frequency of 825 GHz. The matching of the couplers and the conduction loss of the helix are expected to be sufficient for eliminating any harmful

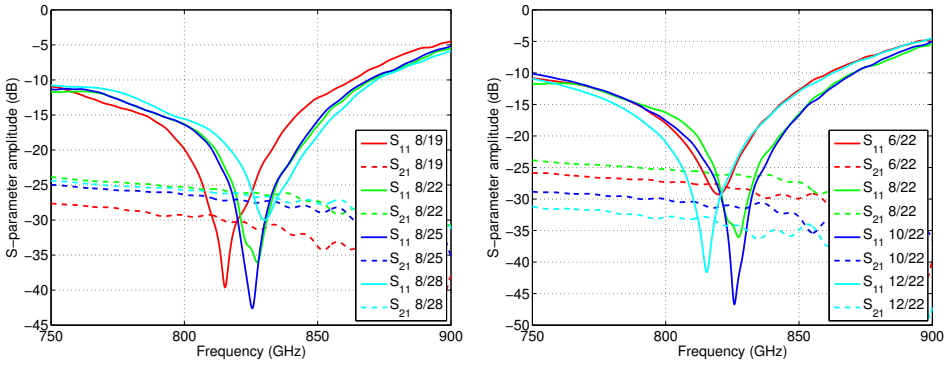

(a) (b)

Figure 2.13: The effect of the mesh parameter (a) m ($N_m = 8$) and (b) N_m ($m = 22$) on the S-parameters.

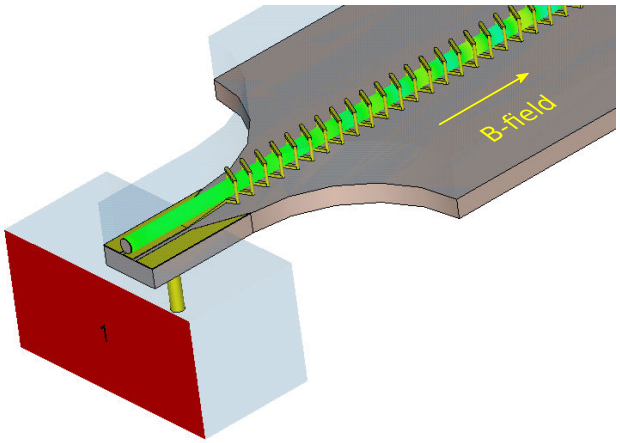

Figure 2.14: Input end of the traveling wave tube showing the beam inside the helix and the orientation of the focusing magnetic field.

oscillations, hence the use of a sewer has been omitted. A 3-dB instantaneous bandwidth of 69 GHz (8%) demonstrates the broadband operation of the square helix SWS.

Output power and gain as a function of input power at 825 GHz are shown in Figure 2.15c; otherwise the same parameters as in Table 2.3 are used. The saturation occurs at an input power of 13 dBm when the electron bunches have lost so much kinetic energy that they start slipping out of the decelerating phase of the axial electric field. The saturated output power and the

Table 2.3: Parameters in the hot simulation.

V_b [V]	I_b [mA]	r_b [μm]	B [T]	P_{in} [dBm]
9650	2.7	8.5	1	-3

power added efficiency (Figure 2.15d),

$$\eta_{PAE} = \frac{P_{out} - P_{in}}{P_{DC}}, \tag{2.25}$$

are 28 dBm and 2.2%, respectively. A depressed collector is not used, and the beam is let to collide with the envelope wall at the output end of the tube. However, already when the input power exceeds 9 dBm ($P_{out} = 25.8$ dBm), the helix starts to intercept the e-beam: strong space charge forces at end of the tube cause the beam to expand. Considering the thickness of the wire, this would have fatal consequences in the realized device.

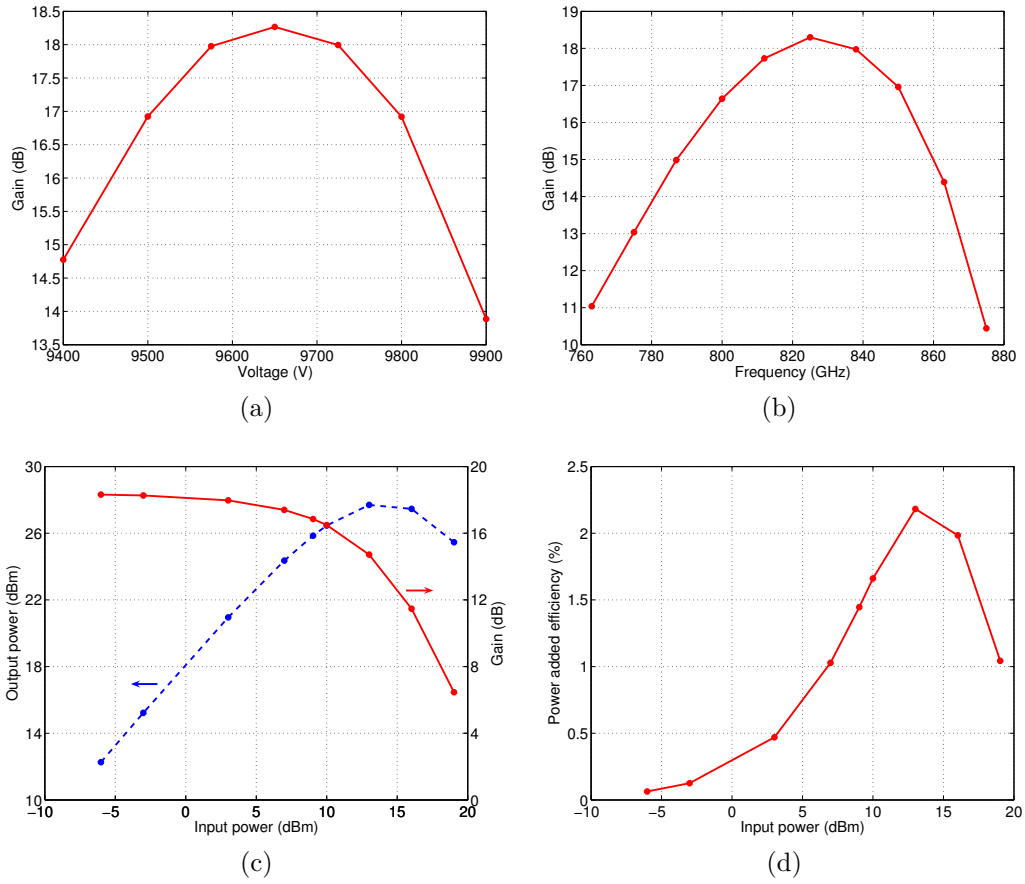

Figure 2.15: Gain as a function of (a) voltage, (b) frequency and (c) input power. Also the output power is shown in panel (c). Panel (d) shows the power added efficiency.

2.3 Frequency Multiplication

Linearization of traveling wave tubes employed in satellite communication applications at microwave frequencies has received much attention due to increasing data rate demands. Harmonic distortion is a problem especially in very broadband traveling wave tubes operated at the lower end of the operating band, because the harmonic signals may also reside within the operating band and become amplified [31]. In this section, which is based on [50], the possibility of exploiting the harmonic distortion in a terahertz traveling wave tube to perform frequency multiplication is considered: would a significant amount of power be produced even if the harmonic frequencies did not reside within the operating band?

The output response of a nonlinear device may be written as

$$v_o = a_0 + a_1 v_i + a_2 v_i^2 + a_3 v_i^3 + \ldots, \tag{2.26}$$

where v_i is the input voltage and v_0 the output voltage. For an ideal linear amplifier $a_1 > 1$ and all the other coefficients are zero. A sinusoidal input voltage at a frequency ω_0,

$$v_i = V_0 \cos(\omega_0 t), \tag{2.27}$$

applied to the input of a nonlinear amplifier generates an output voltage

$$\begin{aligned} v_o &= a_0 + a_1 V_0 \cos(\omega_0 t) + a_2 V_0^2 \cos^2(\omega_0 t) \\ &\quad + a_3 V_0^3 \cos^3(\omega_0 t) + a_4 V_0^4 \cos^4(\omega_0 t) + ... \\ &= \left(a_0 + \frac{1}{2} a_2 V_0^2 + \frac{3}{8} a_4 V_0^4\right) + \left(a_1 V_0 + \frac{3}{4} a_3 V_0^3\right) \cos(\omega_0 t) \\ &\quad + \left(\frac{1}{2} a_2 V_0^2 + \frac{1}{2} a_4 V_0^4\right) \cos(2\omega_0 t) + \frac{1}{4} a_3 V_0^3 \cos(3\omega_0 t) \\ &\quad + \frac{1}{8} a_4 V_0^4 \cos(4\omega_0 t) + ... \end{aligned} \tag{2.28}$$

The output signal is distorted and contains harmonic components at frequencies $2\omega_0$, $3\omega_0$, ... Furthermore, the gain of the fundamental frequency component is dependent on the higher order coefficient a_3,

$$G_{\omega_0} = \frac{v_{o,\omega_0}}{v_{i,\omega_0}} = \frac{a_1 V_0 + \frac{3}{4} a_3 V_0^3}{V_0} = a_1 + \frac{3}{4} a_3 V_0^2, \tag{2.29}$$

which models the saturation of the amplifier, or the decrease of gain at higher input voltage levels, because of the negative sign of the coefficient. Similarly,

the conversion gain from the fundamental frequency to the second harmonic frequency is

$$G_{2\omega_0} = \frac{v_{o,2\omega_0}}{v_{i,\omega_0}} = \frac{\frac{1}{2}a_2V_0^2 + \frac{1}{2}a_4V_0^4}{V_0} = \frac{1}{2}a_2V_0 + \frac{1}{2}a_4V_0^3 \tag{2.30}$$

and hence dependent on the input signal amplitude in all circumstances.

2.3.1 Nonlinearity in a Traveling Wave Tube

Newton's second law and the continuity equation govern the motion of the electrons in the e-beam. The equations are, respectively,

$$\frac{\partial \nu}{\partial t} = -\nu\frac{\partial \nu}{\partial z} - \eta E_z \tag{2.31}$$

$$\frac{\partial \rho}{\partial t} = -\frac{\partial}{\partial z}\left(\rho\nu\right), \tag{2.32}$$

where ν is the electron velocity, η the electron charge-to-mass ratio, E_z the axial electric field component and ρ the electron charge density. The contribution to the axial electric field by the space charge is neglected in (2.31).

The electrons are located in accelerating or decelerating phases of the axial electric field. The interaction between the field and the electrons is continuous as the electrons move in the vicinity of the SWS. The accelerating and decelerating forces and the fact that the electrons are adjusted to travel slightly faster than the wave cause the electrons to start forming bunches in decelerating phases of the electric field. Velocity and density modulations of the e-beam develop simultaneously, and the products in the first terms on the right side of (2.31) and (2.32) manifest the nonlinear nature of the modulation process.

The electron beam propagating from the cathode to the collector in a vacuum forms a convection current

$$I = AJ = A\rho\nu \tag{2.33}$$

where A is the area of the beam cross section and J the current density. The modulated beam current induces the growing wave onto the slow wave structure and therefore the current distortions are transferred to the wave. Equation (2.33) shows that the modulation in the e-beam current is determined by the product of the modulated charge density and the modulated velocity,

meaning that the generation of harmonic distortion can not be avoided in a traveling-wave tube. In the small-signal regime, the electron bunches are located in decelerating phases of the electric field and their kinetic energy is transformed into electromagnetic energy of the wave, the amplitude of which grows exponentially. At the same time the electron bunches become denser and denser, the charge density more and more non-sinusoidal, and the harmonic content of the e-beam consequently increases. In the beginning of the large signal regime, the bunches have given so much of their kinetic energy to the wave that some of the electrons start to slip out of the decelerating phase of the field. These electrons then extract energy from the wave which causes the growth rate of the wave amplitude to decrease. When enough electrons reside in the accelerating phase of the field, the amplitude growth ceases and saturation occurs. The break up of the electron bunches at saturation increases the harmonic distortion in the tube.

The saturation manifests itself also through the 1 dB compression point (AM/AM distortion). The bunching process becomes quicker as the input power is increased and the start of the large signal region and the saturation point shift closer to the input end of the TWT.

2.3.2 Structure of the Traveling Wave Tube

Figure 2.16 shows the dispersion of the two lowest modes and the beam line for a beam voltage of 10360 V. The operating frequency is 850 GHz. Wave propagation along the helix at the frequency of the second harmonic (1700 GHz) is possible, but no amplifying interaction with the electron beam will take place.

The total number of SWS periods in the TWT considered in this section is 176, corresponding to a length of 3.9 mm. Ideal copper conductivity of $5.8 \cdot 10^7$ S/m is used. A prefocused electron beam with a radius of 8.8 μm and a current of 5.5 mA centered on the helix axis is employed. The focusing axial magnetic field has a strength of 1.4 T. The transitions from the coplanar waveguide to the rectangular waveguide have been removed, and lumped ports connected between the ground (i.e. the boundary of the simulation domain modeled as a perfect electric conductor) and the center conductor of the coplanar waveguide are used at the input and output to generate and detect the signal.

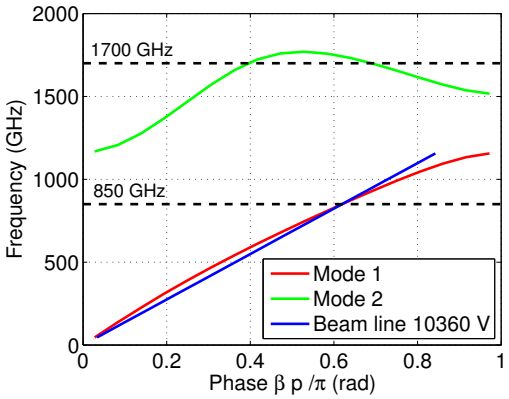

Figure 2.16: Two lowest pass bands of the square helix SWS.

2.3.3 Simulated Nonlinearity

A continuous sine wave at the frequency of 850 GHz is used as an input signal, and the nonlinearity in the TWT is studied by increasing the input signal power from -10 dBm to 22.4 dBm and by taking the Fourier transform of the voltage at the output port (marked with a red cone in Figure 2.17) once a steady state has been attained. Figure 2.17 shows the velocity modulation of an electron beam propagating inside the helix SWS. The electron line number density as a function of the axial position for an input power of 22.4 dBm is shown in Figure 2.18. The density modulation due to electron bunching is sinusoidal in the beginning, but becomes clearly nonlinear already before 1000 µm as the bunches become denser. The number density between the bunches must naturally sink below the DC beam density (axial position 0 µm), which is also seen in the figure. The phase of the axial electric field component relative to the density peaks in the small-signal region is shown: the bunches are located in the retarding, i.e. positive, phases of the field. The line density starts to decrease soon after 3000 µm, and the splitting of the density peak tips into two parts after 3500 µm is a sign of electrons overtaking each other [4]. It is evident that the input signal is sufficiently powerful for saturating the tube with the given SWS length.

Figure 2.19a shows the AM-AM curve and the gain for the fundamental frequency (850 GHz), while Figure 2.19b shows the AM-AM curve and the conversion gain for the 2nd harmonic (1700 GHz). These figures also show the fit of (2.29) and (2.30) to the respective gain curves. The equations model the gain well, and the obtained coefficients a_i (see the figure caption) can be used to predict, for example, the intermodulation distortion

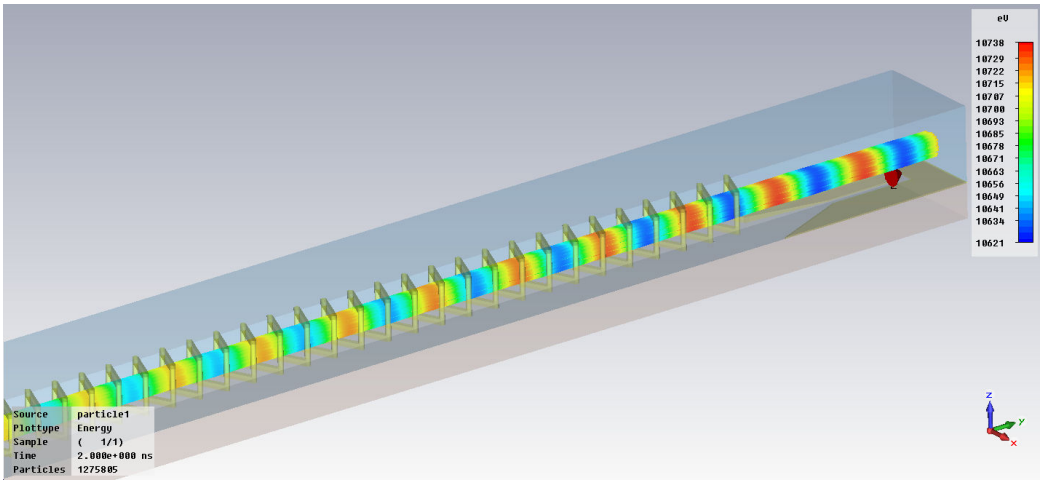

Figure 2.17: Velocity modulated e-beam propagating inside the helix SWS.

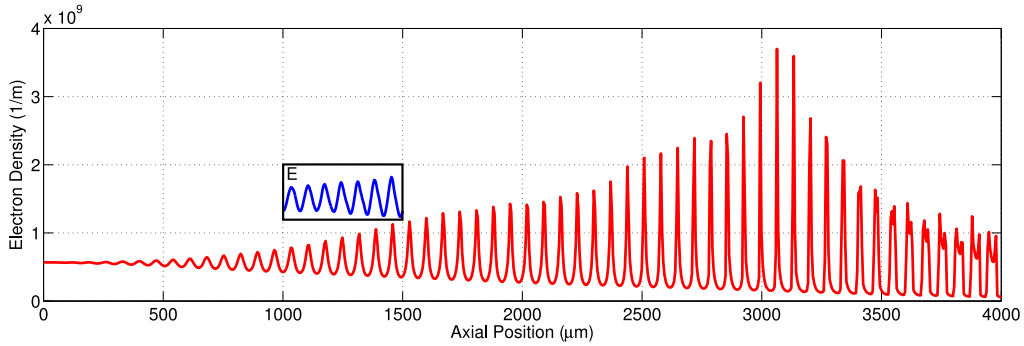

Figure 2.18: Electron line number density along the helix axis for an input power of 22.4 dBm. The axial component of the electric field (arbitrary y-scale) shows the phase of the field relative to the electron bunches.

in the tube. Power saturation in Figure 2.19a occurs at an input power of 21 dBm. Figure 2.20a and Figure 2.20b present the power added efficiency at the fundamental frequency and the conversion efficiency to the 2nd harmonic (the ratio of the output power at the second harmonic to the input power at the fundamental frequency), respectively. A maximum conversion efficiency of 8.2% to the 2nd harmonic is achieved with an input power of 15.8 dBm. However, as a consequence of local beam expansion due to strong space charge forces at the end of the interaction region, beam interception on the SWS occurs at input power levels greater than 15 dBm. This would most likely melt the thin copper wire and cause the failure of a real device. Therefore a conversion efficiency of 7.4% with an input power of 14.0 dBm is considered more realistic, which is comparable to the conversion efficiency of 4% of a 1500 GHz solid-state doubler given in [13]. The maximum conversion efficiency to higher harmonics was well below 0.1%. The losses are underestimated in the simulations because of ideally smooth material surfaces. Additionally, the output matching is not optimized at the frequency of the second harmonic, and therefore the simulated conversion efficiencies should be regarded as order of magnitude estimates.

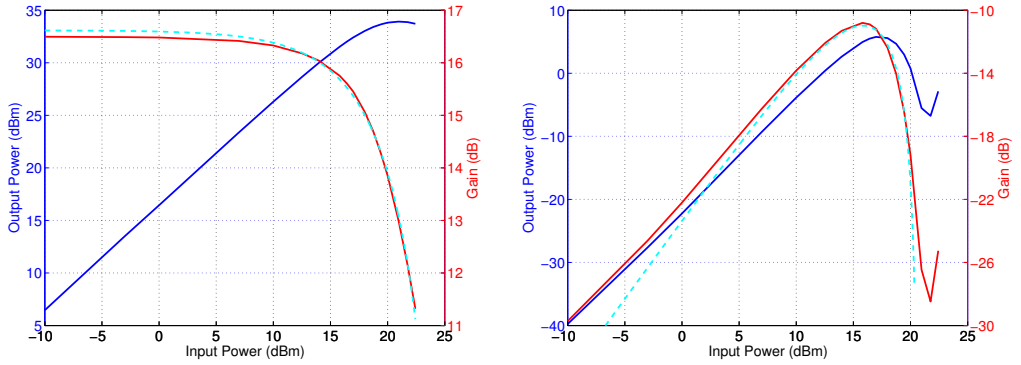

(a) (b)

Figure 2.19: AM/AM curve (blue, left y-axis) and the associated gain at (a) the fundamental frequency at 850 GHz and at (b) the second harmonic component at 1700 GHz. The dashed curves show (2.29) and (2.30) with coefficients $a_1 = 6.8, a_2 = 4.3, a_3 = -24.2$ and $a_4 = -37.7$.

2.3.4 Frequency Doubler Chain

The generation and amplification of harmonic frequencies in a two-stage TWT has been demonstrated in [5], while two-stage gyro-TWTs have been

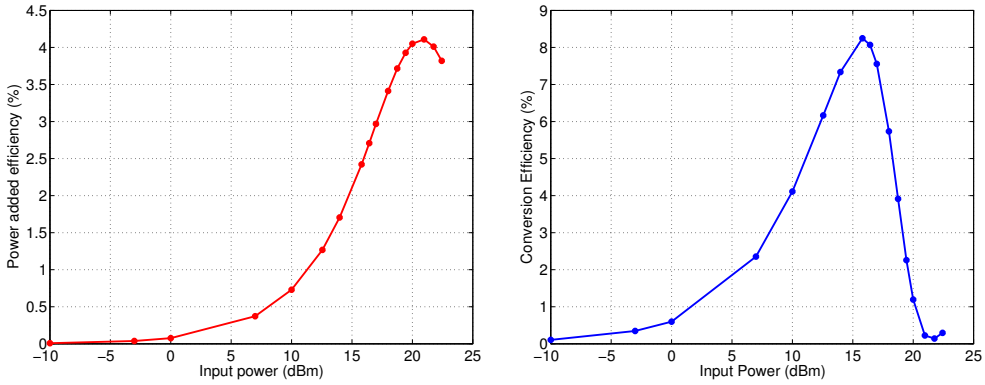

(a) (b)

Figure 2.20: (a) Power added efficiency at the fundamental frequency, (b) conversion efficiency to the 2nd harmonic.

studied more recently e.g. in [15]. The common principle for both amplifier types is that the first stage generates harmonic frequency components in the electron beam. The beam then enters the second stage, where the conditions are adjusted to be such that a wave at a particular harmonic frequency is induced and amplified. The gyrofrequency, and thus the magnetic field, is essential in the operation of a gyro-TWT, and the advantage of frequency multiplication arises from the fact that the magnetic field required to generate output power at a specific frequency is reduced by a factor equal to the harmonic number.

In order to illustrate the capabilities of a single-stage 850-GHz TWT as a frequency doubler, the configuration shown in Figure 2.21 is considered. A solid-state frequency-multiplied source such as the one described in [62] is thought to produce the input power P_0. The source is capable of providing 0 dBm at 850 GHz at room temperature. The input signal is first amplified in a traveling wave tube identical to the one used in frequency doubling. Referring to Figure 2.19a, the gain of the TWT amplifier at 0 dBm input power is 16.5 dB. If 16.5 dBm were fed into the second TWT operating as a frequency doubler, beam interception would occur, as mentioned in Section 2.3.3. The input power is therefore reduced to $P_0 = -2.5$ dBm. The power of the fundamental frequency at the amplifier output is now $P_1 = 14.0$ dBm and, at the end of the chain, the power $P_2 = 2.7$ dBm is obtained at the second harmonic at 1700 GHz. For comparison, solid-state multiplier chains are able to provide not more than -20 dBm at room or -10 dBm at cryogenic temperature at this frequency [12]. However, the preamplifier is essential for achieving the high performance. Without it, the output power drops to

-22 dBm for an input power of 0 dBm.

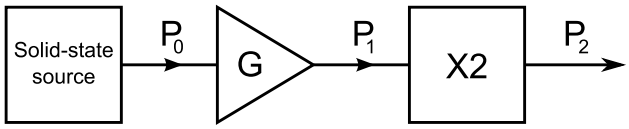

Figure 2.21: A frequency doubler chain utilizing TWTs for THz-amplification and frequency doubling.

2.3.5 Results

Particle-in-cell simulations have been performed in order to study harmonic distortion in a traveling wave tube with a square helix slow wave structure operating at 850 GHz. The maximum output power at the second harmonic frequency (1700 GHz), 2.7 dBm, is achieved when the tube is driven with an input power of 14 dBm, which corresponds to a conversion efficiency of over 7%. Even though this value should be considered as an order of magnitude estimate because of the underestimated losses and the non-optimized output matching, it indicates that a traveling wave tube could function as a frequency doubler that produces a notable amount of local oscillator power at frequencies in the excess of 1 THz, despite the lack of amplifying interaction between the e-beam and the second harmonic signal. The harmonic frequency signal can be extracted by coupling the output signal to a rectangular waveguide with such dimensions that the cutoff frequency is higher than the fundamental frequency. The fundamental frequency is reflected, and an isolator or a sewer needs to be employed to avoid oscillations in the doubler tube. This, as well as a study on the e-beam and slow wave structure parameters in order to improve the conversion efficiency, should be addressed in the future.

2.4 1-THz Cascade Backward Wave Amplifier

The amplification in a traveling wave tube is based on the synchronism between an electron beam and a wave in the forward wave regime of the dispersion curve where the phase and the group velocities have the same direction. Synchronism can also be achieved in the backward wave regime where the velocities are in the opposite directions, as illustrated in Figure 2.22a. A backward wave tube may function as an amplifier or as an oscillator. The commencement of oscillations is determined by the amount of beam current when the interaction structure length is fixed, or by the length when the beam current is fixed. The consequence is that the higher the gain of a backward wave amplifier, the closer it is for breaking into oscillation. The gain of a single-stage backward wave amplifier is limited due to this property. As the dispersion diagram suggests, the instantaneous bandwidth of the backward wave amplifier is narrow, but the operating point can be tuned with the beam voltage.

The cascade backward wave amplifier (CBWA), the schematic of which is shown in Figure 2.22b, overcomes the gain limitation [19]. The amplifier consists of two sections in which backward wave interaction takes place. The first one, at left in Figure 2.22b, is a conventional backward wave amplifier with a matched load at the output port near the electron gun. The RF input signal modulates the electron beam only to a moderate extent, so that the gain stays well below the oscillation condition. The density modulated electron beam flows then through a drift tube to the second section where enhancement of the beam modulation is performed. The drift tube provides high isolation between the two sections for the RF wave. As the beam is premodulated, the second section provides a higher gain than the first section with the same interaction structure length.

In comparison to the forward wave regime, operation in the backward wave regime allows a longer SWS pitch, which is attractive when realizing THz vacuum electron devices with microfabrication. A first-of-its-kind 1-THz CBWA has been developed within the European project OPTHER (Optically driven terahertz amplifiers) [71], [70]. In the following, a brief description of the double-corrugated waveguide slow wave structure [68] utilized in the amplifier of the OPTHER project is given, and then the focus is set on the design of efficient input/output couplers and on the measurement of slow wave structure losses.

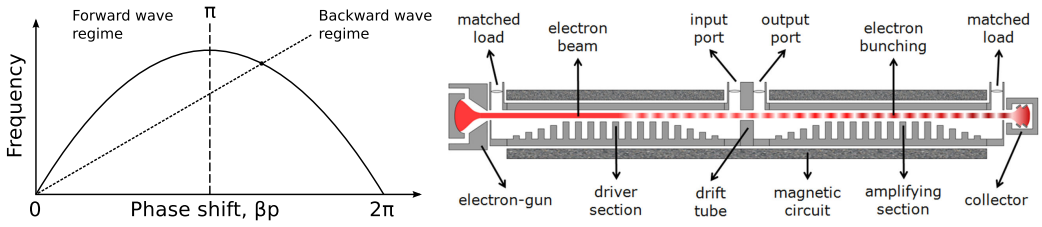

(a) (b)

Figure 2.22: (a) Interaction in the backward wave regime with the -1 space harmonic, (b) schematic of the cascade backward wave amplifier.

2.4.1 Slow Wave Structure

One period of a double-corrugated waveguide SWS is illustrated in Figure 2.23. The electron beam is centered between the corrugations and with respect to the waveguide height as illustrated in the inset. The dimensions of the structure are given in Table 2.4. The structure lends itself to two-dimensional microfabrication and provides strong interaction with a cylindrical electron beam.

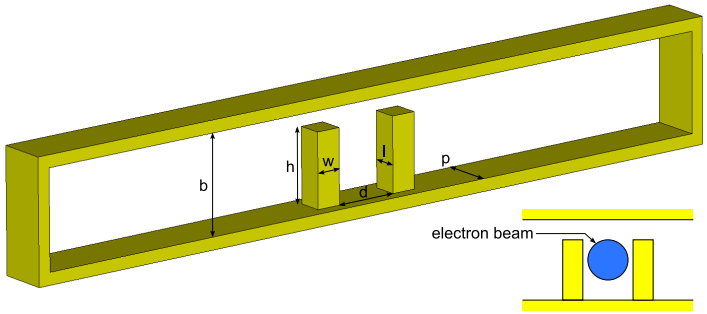

Figure 2.23: One period of a double-corrugated waveguide SWS.

Table 2.4: Dimensions of the double-corrugated waveguide SWS.

b [μm]	d [μm]	h [μm]	l [μm]	p [μm]	w [μm]
80	50	58	20	40	20

2.4.2 Input/Output Couplers

The input wave arrives at the slow wave structure in a rectangular waveguide. The interface between the waveguide and the SWS represents a mismatch for the propagating wave and a matching structure has to be implemented to avoid power reflection. As the geometry of the SWS is similar to the input/output waveguide with the difference of the periodic loading elements (i.e. the corrugations), the matching can be realized by an intermediate section, in which some physical dimension of the corrugations is gradually tapered [99]. The matching performance improves as the taper length increases. A direct quasioptical way of feeding a corrugated SWS similar to the DCW-SWS has been considered in [100], but an antenna is needed to convert the free space wave to the guided wave of the SWS also in that case.

Figures 2.24a and 2.24c show two matching sections in a lowered WR-1.0 waveguide (254 μm × 80 μm): tapering of the height of the double corrugations and tapering of the distance between the two elements of the double corrugations. The length of the tapering section should be as short as possible to minimize the losses and to ensure that the beam-current modulation is not degraded as the e-beam passes through the coupling region and the drift tube. A limiting length of 475 μm, corresponding to 12 double corrugations in the axial direction, is chosen. The S-parameters of the tapers in a back-to-back configuration are simulated, and the results in Figures 2.24b and 2.24d show the height taper to be superior in terms of both insertion and return loss. This is related to the fact that height tapering takes place in the middle of the waveguide, where the field of the TE_{10} mode is the strongest. The rapid deterioration of the performance at the high frequency end of the band is related to the cutoff of the slow wave structure passband. The S-parameter plots depict also the performance of a taper with 25 periods. Even though the return losses of both tapers improve, it is the distance taper that benefits more from the extra length.

The evolution of the electric field in the distance taper is illustrated in Figure 2.25. The transformation of a TE_{10} mode (arrows pointing into or out of the page) to a hybrid mode of the double corrugated SWS with an axial component between the corrugations is clearly seen in Figure 2.25d.

Unfortunately, the manufacturing of the height taper is difficult with established two-dimensional microfabrication techniques such as lithography. For each step in the height dimension, a different mask is required. This would increase the fabrication costs, but perhaps even more importantly, due to the small feature sizes in the terahertz region, the alignment accuracy of

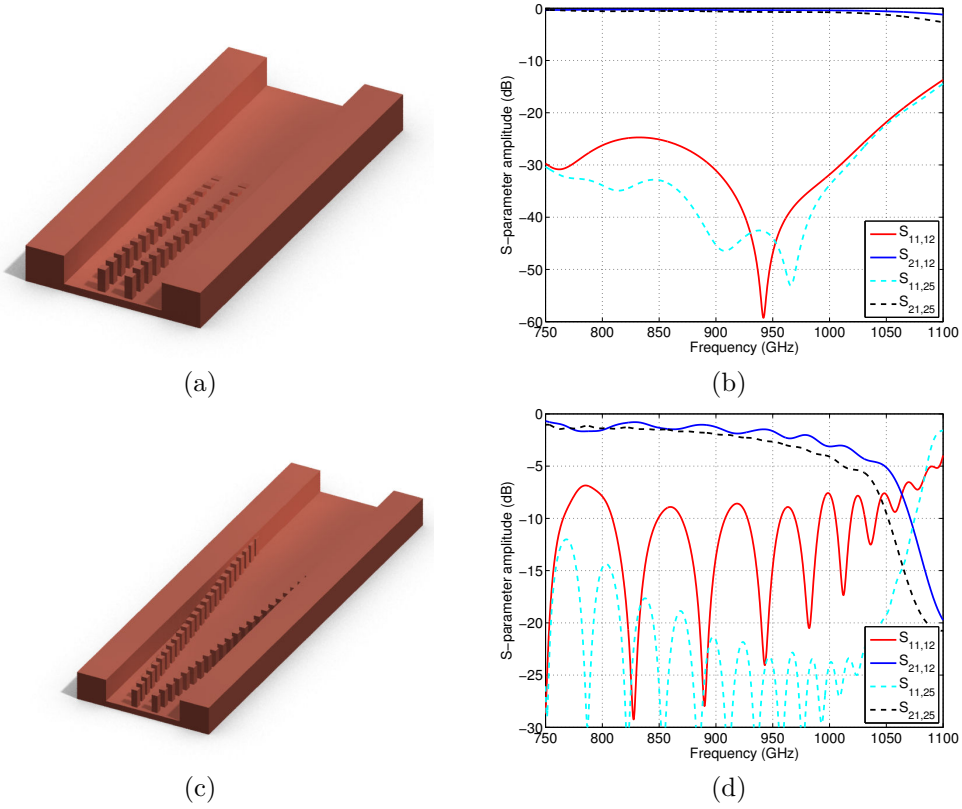

Figure 2.24: (a) and (c) show the schematics of the height and distance tapers, while (b) and (d) are the corresponding back-to-back S-parameters. The taper length is 12 periods for the solid lines and 25 for the dashed lines.

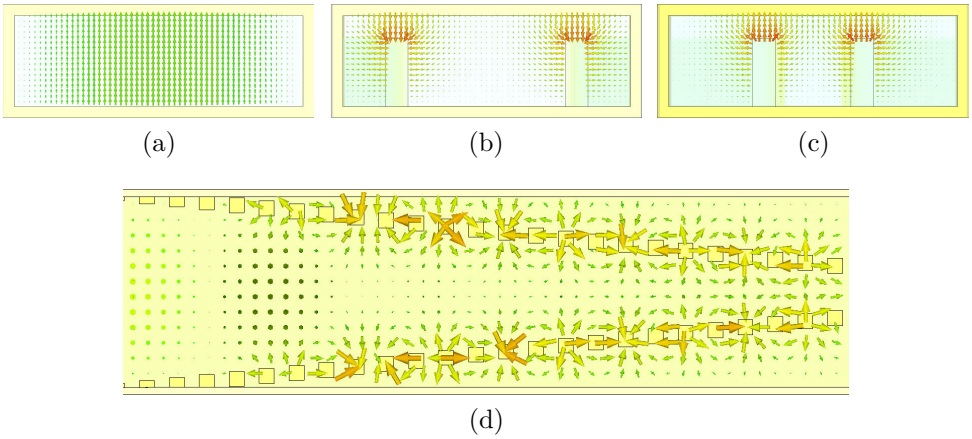

Figure 2.25: Electric vector field in the distance taper: (a)–(c) evolution in the transverse plane, (d) top view.

the masks should be better than a few micrometers. Another possibility to realize the height tapering would be an exposure of the structure from two perpendicular directions, but also this method requires extreme rotational and alignment accuracy.

The use of distance tapering avoids these problems since the whole structure, the matching sections and the slow wave structure, could be realized in one step. In order to obtain better performance in the shortest possible length, another matching section is designed: the distance between the corrugations in transverse direction is tapered nonlinearly, and one side of each corrugation is connected to the waveguide side wall in order to reduce the insertion loss. Small changes, in the order of a couple of micrometers, in the pitch of the corrugations in the axial direction help to improve the overall performance. The schematic of the taper is shown in Figure 2.26a and the simulated S-parameters in 2.26b. The return loss is clearly above 10 dB over most of the WR-1.0 band ($\Delta f = 250$ GHz), and the average insertion loss is approximately 1 dB lower than the one provided by distance tapering with 12 periods. A scanning electron microscope (SEM) image of the input/output coupling region realized with X-ray LIGA is shown in Figure 2.27a. The drift tube connecting the two sections of the cascade backward wave amplifier is seen in the center and the dual-mode horns, discussed in the next section, are seen at left and right. A close-up of the taper is shown in Figure 2.27b.

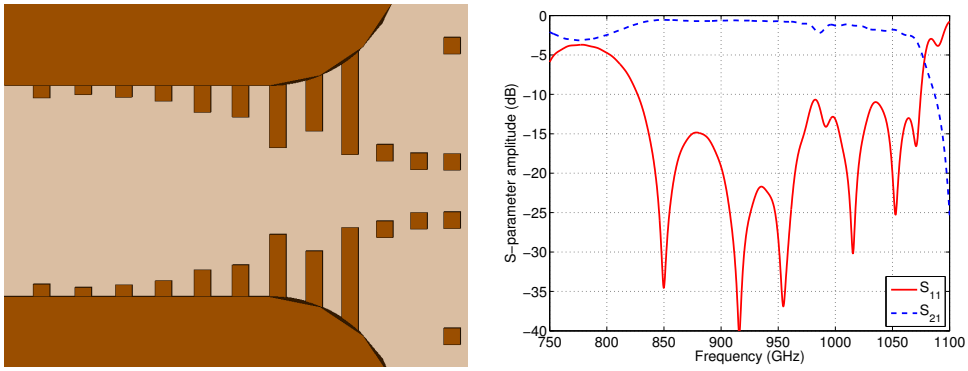

(a) (b)

Figure 2.26: (a) Schematic of the hybrid taper, (b) S-parameters in back-to-back configuration.

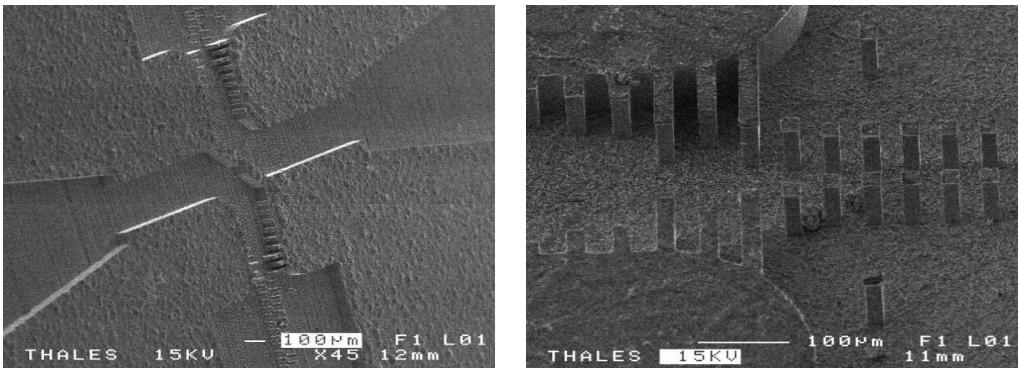

(a) (b)

Figure 2.27: SEM images of the coupling region: (a) overall view, (b) close-up of the taper.

2.4.3 Measurement of Losses

The gain of the amplifier depends on the length of the SWS. In order the select the correct length for reaching the desired gain, the loss per SWS period must be known. It may also occur that the loss per period is too high, so that the realization of the amplifier is not possible with the given specifications.

As the operating frequency increases, the penetration depth of electromagnetic fields into a conductor decreases, and the current flow concentrates more and more on the surface, which is seen from the formula for current density,

$$\vec{J} = \sigma \vec{E}, \tag{2.34}$$

where σ is the conductivity. The skin depth is the depth at which the fields have decayed to a 1/e fraction of the value at the surface, and it is given by the equation

$$\delta = \frac{1}{\sqrt{\pi f \mu \sigma}}, \tag{2.35}$$

where f is the frequency and μ the permeability. Assuming the conductivity of copper, $5.8 \cdot 10^7$ S/m, and a frequency of 1 THz, the skin depth is only 66 nm. If the surface roughness of the conductor is of the same order or greater than the skin depth, the currents on the surface end up following a crooked path causing a higher effective resistivity and losses than a smooth surface.

Three slow wave structure samples having lengths of 4 mm, 6 mm and 8 mm, corresponding to 100, 150 and 200 double corrugations, have been realized

with X-ray LIGA (Figure 2.28a). These number do not include the matching sections at the input and output of the SWS. They utilize the distance taper and have a length of 25 corrugations each (Figure 2.28b). The S-parameters of each structure in both directions (S_{11}, S_{21}, S_{22}, S_{12}) have been measured with a vector network analyzer from Agilent and WR-1.0 (750–1100 GHz) extenders from Virginia Diodes. Point-wise and sweep averaging have been used, and they yield very similar results. The measured S-parameters of 4 mm and 8 mm samples are shown in Figure 2.29a and 2.29b, respectively. The parameters S_{21} and S_{12} are around -40 dB, also in the case of the 10 mm sample, even though a difference of clearly over 10 dB is expected. The power gain in decibels is calculated for both directions in the case of each structure,

$$G_{21} = 10 \log \frac{|S_{21}|^2}{1 - |S_{11}|^2}, \tag{2.36}$$

$$G_{12} = 10 \log \frac{|S_{12}|^2}{1 - |S_{22}|^2}, \tag{2.37}$$

from which the average G_a is calculated. The average gains of two structures having different lengths are subtracted from each other, and the result is divided by the difference in the number of periods (N) to obtain the gain per period:

$$G_{cell} = \frac{G_{a,long} - G_{a,short}}{N_{long} - N_{short}}. \tag{2.38}$$

As the matching sections are theoretically identical, their contribution is cancelled out. The loss per period, $-G_{cell}$, should be positive and show an increasing trend with the frequency as the cutoff of the slow wave structure is approached, but such loss characteristics is not observed in Figure 2.29c which presents the loss per cell calculated from the S-parameters of the 4 mm and 8 mm samples.

In order to understand the reason behind the unexpected results, a series of simulations based on the 4 mm sample is undertaken. Visual inspection of the realized 4 mm structure reveals variations in the height of the corrugations. Consequently, the height of three subsequent corrugation pairs is increased in the simulations. The evolution of S-parameters for excess heights from 0 µm to 15 µm is shown in Figure 2.30, and it can be seen that three corrugation pairs with an excess height of 15 µm attenuate the transmitted signal to the level found in the measurements. The evolution of the insertion loss with height results from the fact that the operating band is defined by the height of the corrugations, and an increase in height causes a proportional shift of the upper cutoff towards lower frequencies. The position of the corrugations

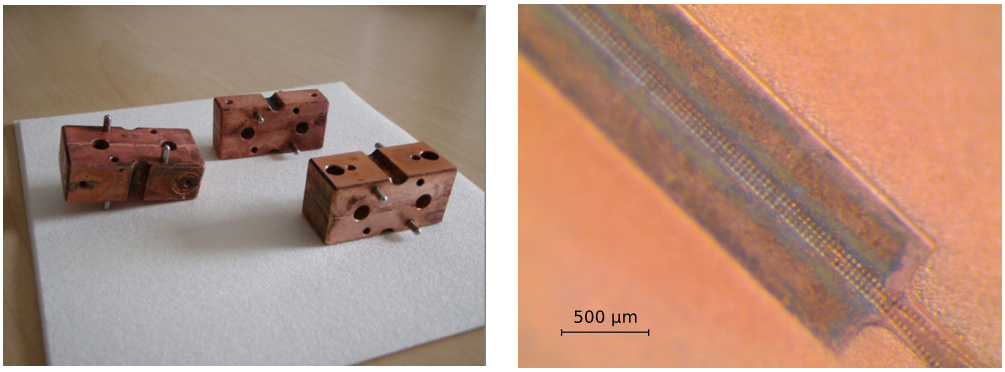

(a) (b)

Figure 2.28: (a) Loss measurement samples, (b) slow wave structure and matching section inside the samples.

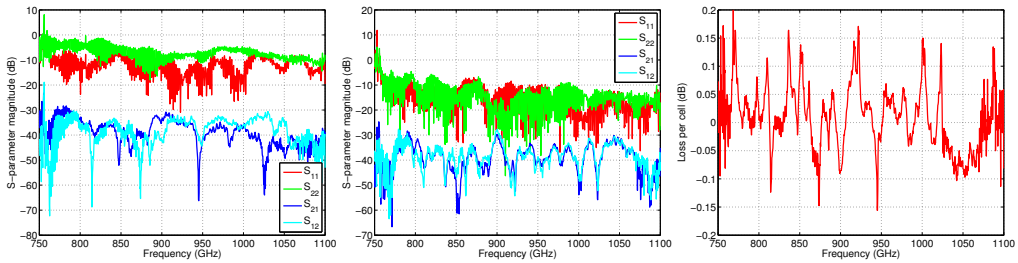

(a) (b) (c)

Figure 2.29: S-parameters of a) 4 mm and b) 8 mm samples, and c) the loss per period.

has naturally an influence on the results; in this case, the teeth were located in the middle of the SWS causing S_{11} and S_{21} to be identical with S_{22} and S_{12}, respectively. In addition to the height variations, some of the corrugations in the realized structures are missing, as made apparent by Figure 2.31a. The location of a missing corrugation pair does not affect the simulated S_{21}, meaning that S_{12} is identical to S_{21}. The insertion loss increases as shown in Figure 2.31b, but this time not due to the shift of the cutoff frequency. A significant decrease in S_{11} is observed in Figure 2.31c when two subsequent corrugation pairs are missing. The closer the defect is to the input port, the stronger is the effect. The distance to both ports is approximately equal for $z = 48$ and the S_{22} in Figure 2.31d consequently becomes equal to S_{21}. The variation of the S-parameters could, in principle, be used to locate the position of the defect, at least in the case of a shorter structure with less unknown variables. It is concluded that the manufacturing quality of the slow

wave structures has to be improved, especially in terms of height variations. The task is highly demanding, considering the number of corrugations.

Despite the setback in measuring the losses at 1 THz, an estimation of losses for the PIC simulations has been obtained by realizing large scale models with different lengths at 10 GHz and 100 GHz and by determining the loss per period from the S-parameter measurements as described above. Knowing that the conductor loss increases proportionally to the square root of the frequency, the results are extrapolated to 1 THz. A reduction of copper conductivity by a factor of $\sqrt{2.25}$ is required in the eigenmode simulations to obtain an agreement between the measured and simulated loss.

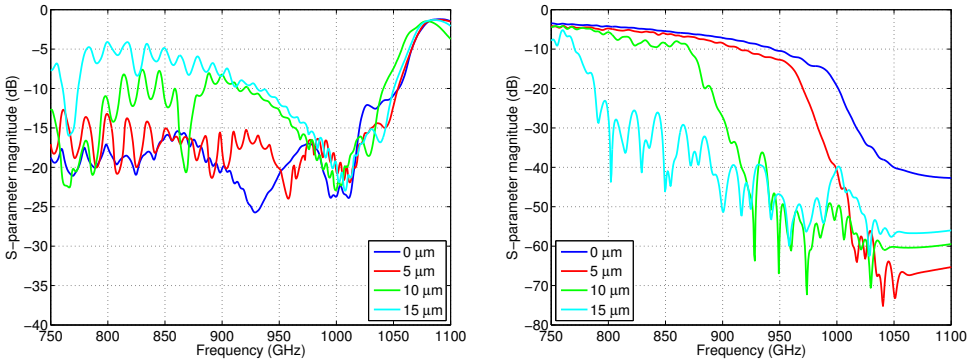

(a) (b)

Figure 2.30: Simulated effect of excess height on (a) S_{11} and (b) S_{21}.

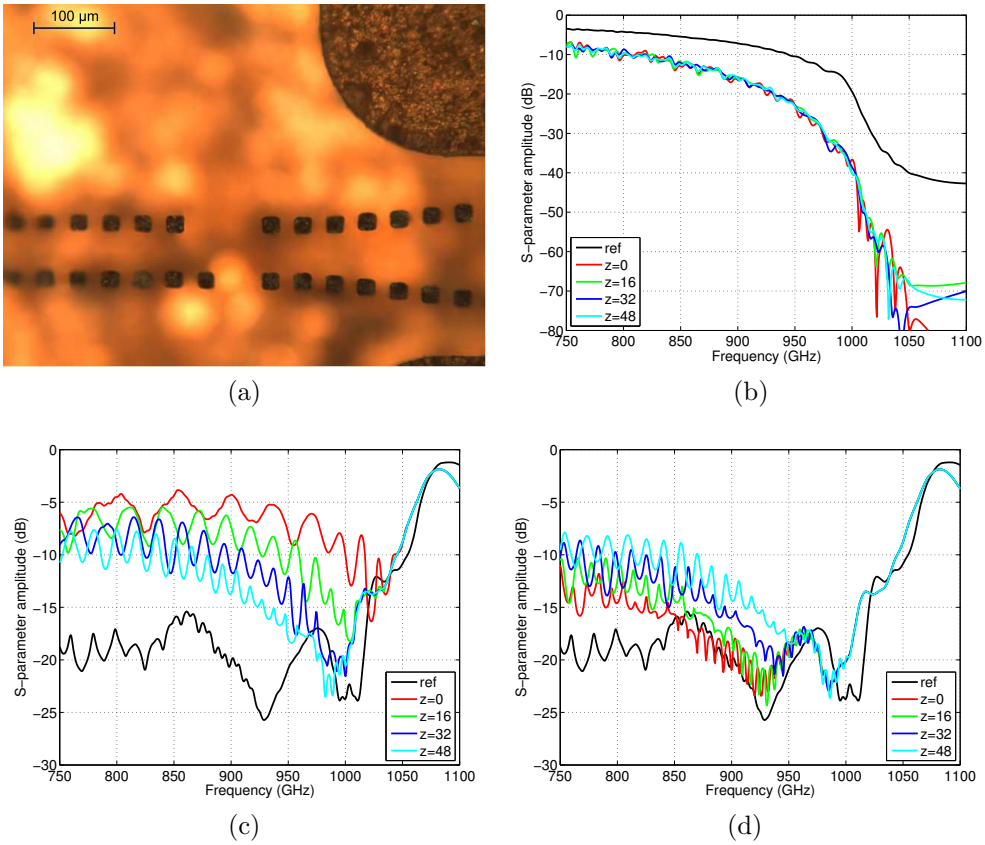

Figure 2.31: (a) Measurement sample with missing corrugations at the throat of the SWS, and the simulated effect of two missing corrugation pairs on S-parameters at different distances from the throat (given in number of periods): (b) S_{21}, (c) S_{11}, (d) S_{22}. The total length of the structure is 102 periods. Curves *ref* are for the structure with no defects. In order to make the overall behavior of S_{11} and S_{22} better visible, deep notches have been removed by applying a 15-point rolling average (the total number of points is 1001).

2.5 Dual-Mode Horn

Several methods to couple the signal from a slow wave structure to a rectangular waveguide have been presented in the previous sections. As the slow wave structure is situated inside a vacuum envelope, it is necessary to guide the wave through a vacuum window at some point. The small size of a rectangular waveguide at 1 THz makes the mounting of a vacuum window inside the waveguide difficult. This section, based on [53], presents a design of a horn antenna with an integrated vacuum window in the flaring section of the horn, which allows the use of a larger window size. The horn is attached to the rectangular waveguide of an input/output coupler. Work on a multimode horn with a sapphire window for a THz-backward wave oscillator has been presented in [73].

2.5.1 Introduction

Dual-mode horn antennas (Potter horns) [77],[89] are able to launch a beam with near-Gaussian qualities. While coupling to the fundamental Gaussian mode is somewhat stronger in corrugated horns, the manufacturing of dual-mode horns is much less complicated. A discontinuity in a circular waveguide at the throat of the horn is used to excite a higher order mode (TM_{11}) with a certain amplitude. The horn length and opening angle are then selected to match the phases of the initial TE_{11} mode and the excited TM_{11} mode at the horn aperture, which leads to the desired radiation properties. The in-phase condition limits the bandwidth to below 10%. Figure 2.32 illustrates the superpositioning of the fields at the output aperture.

A dual-mode horn design suitable for terahertz frequencies is described in [75], but as the vacuum window inside the horn disturbs the amplitude ratio and phase difference of the modes, the horn geometry has to be modified accordingly. The vacuum tube assembly shown in Figure 2.34 is such that a gap exist between the slow wave structure block and the vacuum envelope. The gap enables the sliding of the SWS block into the envelope, but causes further phase and amplitude disturbance.

2.5.2 Structure

Figure 2.34 shows the designed dual-mode horn that has been attached to the output waveguide of the CBWA. A close-up of the throat region of the

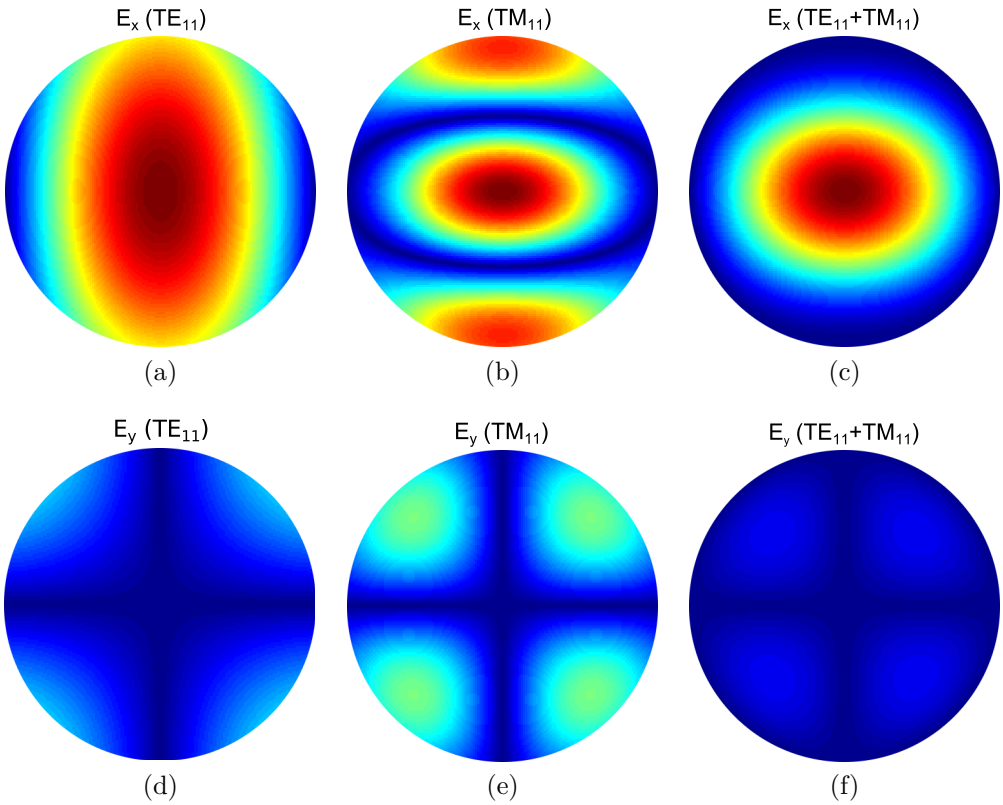

Figure 2.32: Electric field amplitude distributions of TE_{11} and TM_{11} modes and their superposition in a circular waveguide. The high-amplitude field regions (red) at the top and bottom of panel (b) have an opposite phase which leads to field cancellation at these regions in the total field in panel (c). Similarly, the direction of the field vectors in panel (e) is opposite to the direction of the field in panel (d).

horn is presented in Figure 2.35, and the numerical values related to this figure are given in Table 2.5. A rectangular waveguide coming from the SWS is transformed into a circular waveguide, directly after which a discontinuity is introduced by increasing its radius. The horn then flares out. The flaring is interrupted by a gap between the block containing the slow wave structure and the surrounding vacuum envelope. The fields from the horn are coupled to a circular waveguide behind the gap. A quartz disc ($\varepsilon_r = 4.45$) inserted inside the circular waveguide provides vacuum sealing. The baking of the vacuum tube at around 1000 °C sets a requirement to the material of the vacuum window and also restricts the use of coating materials that may be used to enhance the window transmittance. A long flaring section guides the modes through the surrounding permanent magnet.

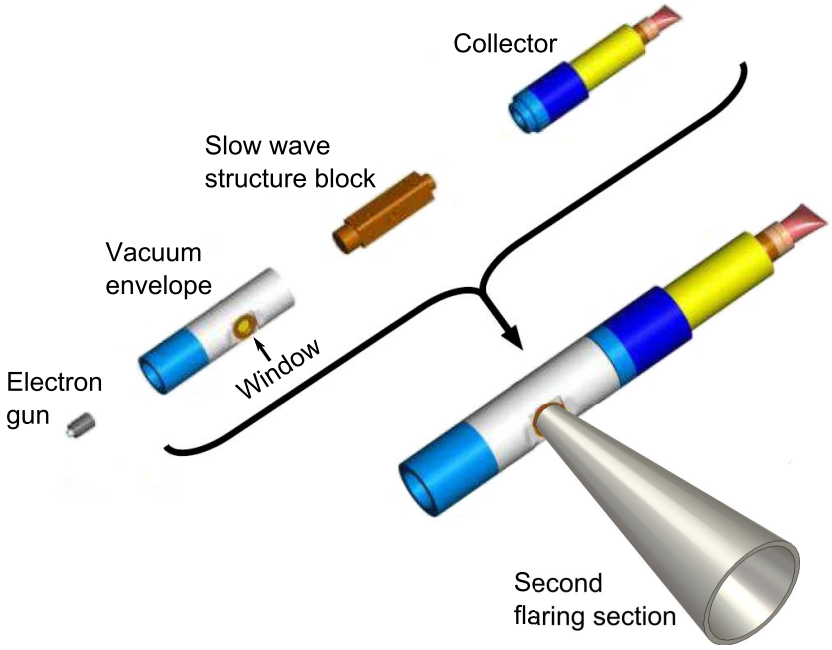

Figure 2.33: Tube assembly. The slow wave structure is slid into the vacuum envelope.

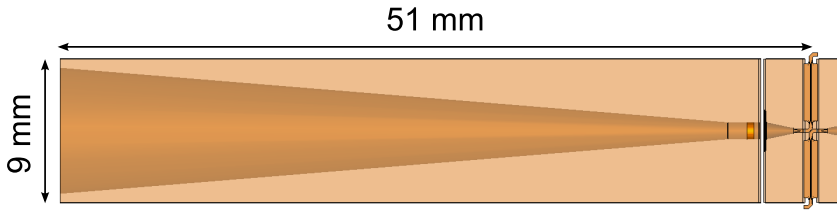

Figure 2.34: Overall dimensions of the dual-mode horn.

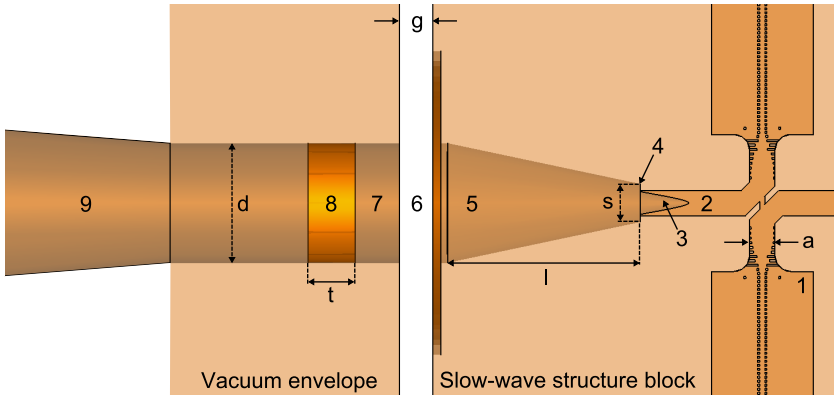

Figure 2.35: Close-up of the throat of the horn: 1) SWS, 2) lowered rectangular waveguide, 3) rectangular to circular waveguide transition, 4) discontinuity, 5) first flaring section, 6) vacuum gap, 7) window holder (circular waveguide), 8) vacuum window and 9) second flaring section.

Table 2.5: Dimensions of the dual-mode horn (see Figure 2.35).

a [µm]	d [µm]	g [µm]	l [µm]	s [µm]	t [µm]
254	1200	339	1937	382	478

2.5.3 Design

For mechanical stability, a minimum window thickness of approximately 500 µm is required. From the electromagnetic point of view, the thickness should be a multiple of a half-wavelength for both TE_{11} and TM_{11} modes. The input impedance seen when looking in the direction of the window in a circular waveguide is

$$Z_{in} = Z_w \frac{Z_{wg} + jZ_w \tan(\beta t_w)}{Z_w + jZ_{wg} \tan(\beta t_w)}. \tag{2.39}$$

If $Z_{in} = Z_{wg}$, no power is reflected back from the window. This means that

$$\tan(\beta t_w) = 0, \tag{2.40}$$

$$\beta t_w = \frac{2\pi}{\lambda_g} = \pi n, \tag{2.41}$$

$$t_w = n\frac{\lambda_g}{2}. \tag{2.42}$$

The multiple $n = 7$ gives thicknesses of 479 µm and 483 µm for TE_{11} and TM_{11}, respectively, and provides better phase difference behavior around

1040 GHz than the higher multiples. However, an improved overall return loss is obtained by selecting a window thickness of 478 μm.

The geometry of the discontinuity at the throat of the first flaring section is optimized to obtain the desired amplitude ratio and phase difference between the modes after the window. The geometry of the second flaring section is then selected to fulfill the mechanical requirements and the in-phase condition of the modes at the output aperture of the horn. A flaring section can be regarded as a series of infinitely short cylindrical waveguides with different radii. The propagation constants expressing the phase change per unit length (towards negative values) for TE_{nm} and TM_{nm} modes in a circular waveguide are

$$\beta_{nm}^{TE} = \left[k_0^2 - \left(\frac{p'_{nm}}{a}\right)^2\right]^{1/2}, \tag{2.43}$$

$$\beta_{nm}^{TM} = \left[k_0^2 - \left(\frac{p_{nm}}{a}\right)^2\right]^{1/2}, \tag{2.44}$$

where a is the waveguide radius, p'_{nm} is the nth root of the derivative of the Bessel function of mth order, and p_{nm} the nth root of the Bessel function of mth order. Specifically, $p'_{11} = 1.841$ and $p_{11} = 3.832$, and therefore $\beta_{11}^{TE} > \beta_{11}^{TM}$, so the phase of the TE_{11} mode changes more rapidly, and phase compensation in a circular waveguide is possible. Letting the length of each waveguide section approach zero, an analytical expression for the phase difference in a conical horn is given in [77]:

$$\begin{aligned}
\Delta\Phi &= \Phi_{11}^{TE} - \Phi_{11}^{TM} \\
&= \cot(\gamma)\left(\left[\left(\frac{a_o^2}{\lambda^2} - \frac{p'^2_{11}}{4\pi^2}\right)^{1/2} - \left(\frac{a_o^2}{\lambda^2} - \frac{p_{11}^2}{4\pi^2}\right)^{1/2}\right.\right. \\
&\quad \left. - \left(\frac{p'_{11}}{2\pi}\cos^{-1}\frac{p'_{11}\lambda}{2\pi a_o}\right) + \left(\frac{p_{11}}{2\pi}\cos^{-1}\frac{p_{11}\lambda}{2\pi a_o}\right)\right] \\
&\quad - \left[\left(\frac{a_i^2}{\lambda^2} - \frac{p'^2_{11}}{4\pi^2}\right)^{1/2} - \left(\frac{a_i^2}{\lambda^2} - \frac{p_{11}^2}{4\pi^2}\right)^{1/2}\right. \\
&\quad \left.\left. - \left(\frac{p'_{11}}{2\pi}\cos^{-1}\frac{p'_{11}\lambda}{2\pi a_i}\right) + \left(\frac{p_{11}}{2\pi}\cos^{-1}\frac{p_{11}\lambda}{2\pi a_i}\right)\right]\right),
\end{aligned} \tag{2.45}$$

where γ is the half flare angle, λ the wavelength and a_i and a_o the radii of the horn at the throat and at the output aperture, respectively. The propagation constant difference, $\Delta\beta_{11} = \beta_{11}^{TE} - \beta_{11}^{TM}$, decreases as the frequency

increases, so in order to attain phase matching in a broad frequency range, the phase difference at the reference plane after the window should ideally be less negative below the center frequency than above it.

2.5.4 Simulated Performance

The horn is simulated with CST Microwave Studio. The second flaring section is very large compared to the wavelength, and in order to reduce the computing time, it is initially not present in the simulation. The simulated amplitude ratio of TE_{11} to TM_{11} at the throat of the flaring section is between 4.0 dB and 5.8 dB in the frequency range of 1020–1060 GHz, as shown in Figure 2.36a. Figure 2.36b shows the simulated phase difference between the modes at the same location. Considering the propagation constant argument presented earlier, the slope of the phase difference curve is disadvantageous from the point of view of broadband phase matching. Using (2.45) and the value of phase difference at 1040 GHz, the length and the opening angle of the second flaring section are selected in such a way that the phase difference is a multiple of $-360°$ at the output aperture. A flaring section with a length of 48 mm, an input aperture radius of 0.6 mm and an output aperture radius of 4.5 mm results into the aperture phase difference curve of Figure 2.37. As expected, the slope of the curve has steepened further. In principle, the attenuation of the flaring section changes the amplitude ratio. As in phase matching, the flaring section can be considered as a series of short waveguide sections, the contributions from which make up the total loss. The attenuation in a cylindrical waveguide decreases as the radius increases [78], and since the waveguide at the throat is already electrically large, the loss in the whole flaring section stays below 0.1 dB. Therefore, the amplitude ratio at the output aperture is practically identical to that of Figure 2.36a. Reference [33] suggests an optimal amplitude ratio of 2.1 dB, so performance improvement, by optimizing the discontinuity further, is possible.

Additionally, the scattering parameter S_{11} can be obtained with good accuracy without the second flaring section. The result in Figure 2.38 is, however, the return loss of the complete horn. It is smaller than -15 dB in a bandwidth of 33 GHz, the limiting factor being the resonant quartz window. Anti-reflection layers may be employed to broaden the window bandwidth. These layers could be concentric circular grooves or cylindrical holes that are machined into the window surface.

In order to simulate the far-field radiation performance with CST Microwave Studio, the second flaring section is included to the simulated structure.

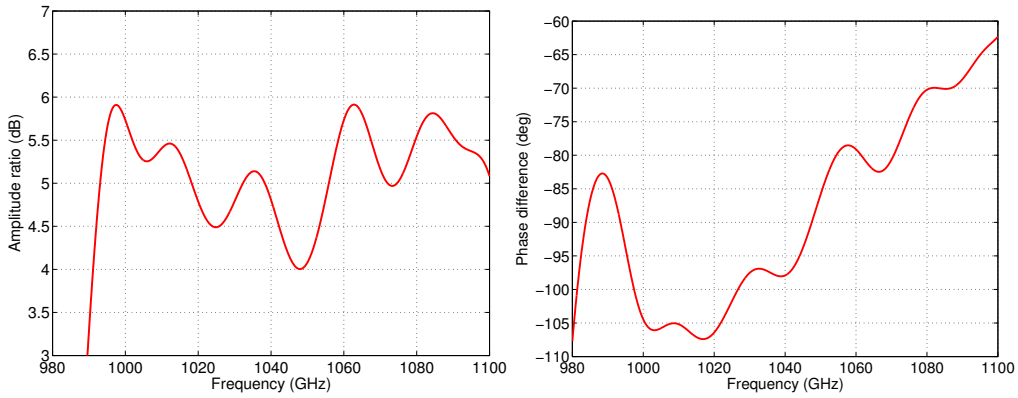

(a) (b)

Figure 2.36: Simulated (a) amplitude ratio and (b) phase difference at the throat of the second flaring section.

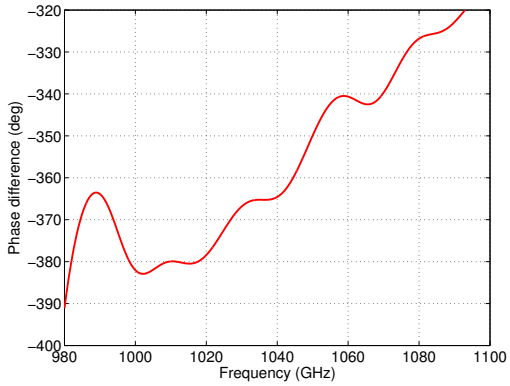

Figure 2.37: Amplitude ratio at the output aperture.

The number of mesh cells required for modeling the complete horn exceeds 500 million, which necessitates the use of powerful CPU/GPU clusters. In order to verify the design before performing such a simulation run, a Gauss-Laguerre analysis of the horn has been carried out as described in Section 2.5.5. The E- and H-plane far-field radiation patterns resulting from the CST simulations at the center frequency, 1040 GHz, and at the frequencies corresponding to the 15 dB return loss points, 1020 GHz and 1060 GHz, are shown in Figure 2.39. The half power beamwidths at 1040 GHz in the E-plane and H-plane are 3.2° and 2.3°, respectively, and the sidelobes are below -35 dB. Only moderate radiation performance degradation is observed at the edges of the operating band. The radiation patterns of the dual-mode horn and a single-mode conical horn (TE_{11}) with comparable dimensions

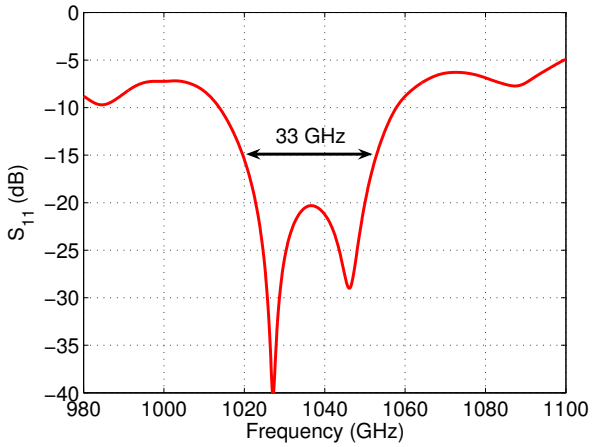

Figure 2.38: Simulated scattering parameter S_{11} of the complete horn model.

are compared in Figure 2.40. It is easy to recognize the advantages of the dual-mode horn in terms of beam symmetry and sidelobe level.

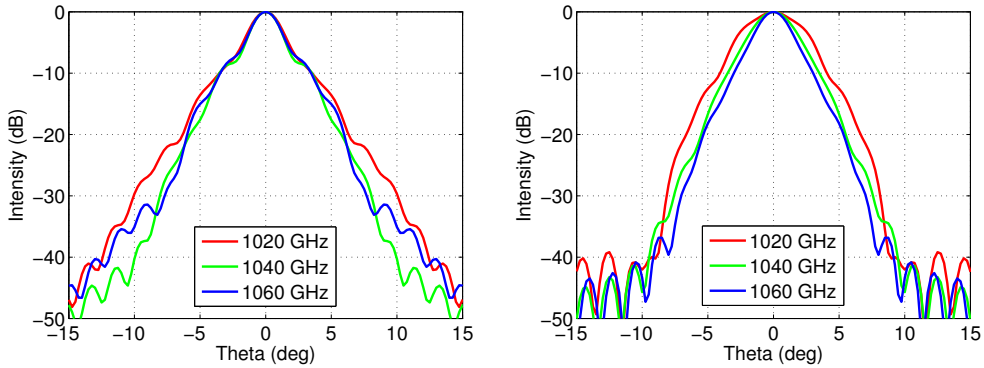

Figure 2.39: Far-field radiation patterns for several frequencies (a) in the E-plane and (b) in the H-plane.

2.5.5 Gauss-Laguerre Analysis

Before running time-consuming 3D simulations of the full dual-mode horn model, it is important to gain an understanding on how the amplitude ratio and phase difference of the modes at the output aperture affect the radiation characteristics. The electric field at the output aperture can be expanded to

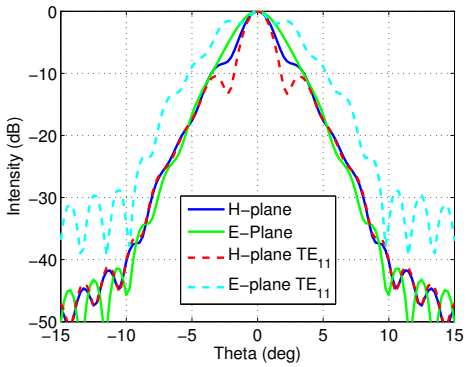

Figure 2.40: Simulated E- and H-plane radiation patterns at 1040 GHz for dual-mode (solid line) and single-mode (dashed line) horn antennas.

Gauss-Laguerre modes [33], the evolution of which with respect to distance is known. Reference [41] explains how the copolar and cross-polar radiation patterns of a dual-mode horn can be calculated based on this method.

The total electric field at the output aperture is given by

$$\vec{E}\left(r,\phi\right) = \frac{\vec{E}_{TE_{11}}\left(r,\phi\right) + C\vec{E}_{TM_{11}}\left(r,\phi\right)}{1+C} \tag{2.46}$$

where $\vec{E}_{TE_{11}}$ and $\vec{E}_{TM_{11}}$ are the electric field expressions for the TE_{11} and TM_{11} modes in a circular waveguide [78] and C is the complex mode balance constant, the real part of which determines the amplitude ratio and the imaginary part the phase difference. By selecting $C = 0.785 = -2.1$ dB as in [41], the radial component of the field vanishes at the aperture boundary. This condition is demonstrated in Figure 2.32. The imaginary part is introduced here in order to estimate the change in the horn radiation performance in the case of non-ideal phase matching. By splitting the mode balance constant into real and imaginary parts, $C = C_r + jC_i$, and by manipulating (2.46), one obtains

$$\begin{aligned}\vec{E}\left(r,\phi\right) &= \frac{1}{1+C}\vec{E}_{TE_{11}}\left(r,\phi\right) + \frac{C}{1+C}\vec{E}_{TM_{11}}\left(r,\phi\right)\\ &= \left(A_{TE}+jB_{TE}\right)\vec{E}_{TE_{11}}\left(r,\phi\right) + \left(A_{TM}+jB_{TM}\right)\vec{E}_{TM_{11}}\left(r,\phi\right)\\ &= K_{TE}\exp\left(j\phi_{TE}\right)\cdot\vec{E}_{TE_{11}}\left(r,\phi\right) + K_{TM}\exp\left(j\phi_{TM}\right)\cdot\vec{E}_{TM_{11}}\left(r,\phi\right),\end{aligned} \tag{2.47}$$

where

$$A_{TE} = \frac{1 + C_r}{(1 + C_r)^2 + C_i^2}, \tag{2.48}$$

$$B_{TE} = -\frac{C_i}{(1 + C_r)^2 + C_i^2}, \tag{2.49}$$

$$A_{TM} = \frac{C_r + C_r^2 + C_i^2}{(1 + C_r)^2 + C_i^2}, \tag{2.50}$$

$$B_{TM} = \frac{C_i}{(1 + C_r)^2 + C_i^2}. \tag{2.51}$$

The amplitude ratio and phase difference of the modes are

$$K = \frac{K_{TE}}{K_{TM}} = \sqrt{\frac{A_{TE}^2 + B_{TE}^2}{A_{TM}^2 + B_{TM}^2}} \tag{2.52}$$

$$\Delta\phi = \phi_{TE} - \phi_{TM} = \arctan\left(\frac{B_{TE}}{A_{TE}}\right) - \arctan\left(\frac{B_{TM}}{A_{TM}}\right), \tag{2.53}$$

respectively. Equations (2.51)–(2.53) are solved for C_r and C_i giving

$$C_r = \mp\frac{\cot(\Delta\phi)\sqrt{\sin(\Delta\phi^2)}}{K}, \tag{2.54}$$

$$C_i = \pm\frac{\sqrt{\sin(\Delta\phi^2)}}{K}. \tag{2.55}$$

For $\Delta\phi \leq 0$ the negative sign is selected for C_r and the positive sign for C_i. Otherwise, the signs are interchanged. The amplitude ratio and the phase difference are read from Figures 2.36a and 2.37 and the complex C is calculated from (2.54) and (2.55). It can be directly inserted into the equations in [41] giving the copolar and cross-polar far-field radiation patterns. The far-field radiation patterns at several frequencies are plotted in Figure 2.41. The half power beamwidths are slightly broader than those simulated with CST Microwave Studio, 4.3° in the E-plane and 5.0° in the H-plane at 1040 GHz. The variation of radiation patterns with respect to the frequency is smaller, but the same qualitative changes can be found: the beam becomes broader as the frequency decreases, the tip of the beam pattern is narrower and the sidelobes are higher in the E-plane than in the H-plane. The radiation patterns of a dual-mode horn and a single-mode horn at 1040 GHz are compared in Figure 2.42. The single-mode radiation pattern is calculated by setting $C = 0$ in (2.46). The improved radiation performance of the dual-mode horn in the E-plane is evident.

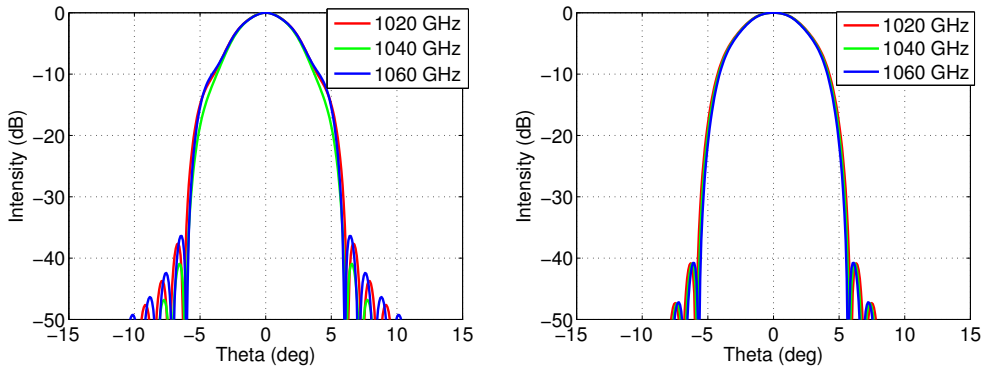

(a) (b)

Figure 2.41: Far-field radiation patterns calculated using the Gauss-Laguerre method for several frequencies (a) in the E-plane and (b) in the H-plane.

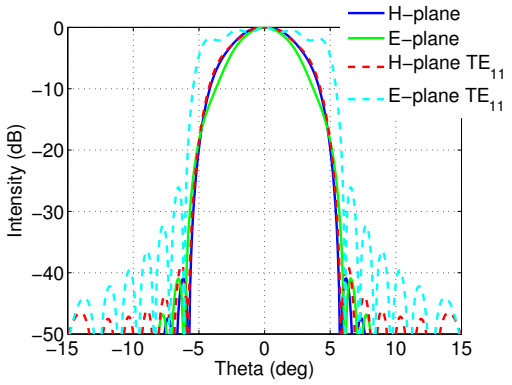

Figure 2.42: E- and H-plane radiation patterns at 1040 GHz calculated using the Gauss-Laguerre method for dual-mode (solid line) and single-mode (dashed line) horn antennas.

2.6 Quasioptical Measurement Setup

Even though vector network analyzer extenders with waveguide flange interfaces enabling measurements up to 1 THz have been recently introduced [42], their scarce availability, the quasioptical input/output interface of the designed amplifier and the desire to study its saturation behavior by using a molecular gas laser, make a fully quasioptical measurement setup preferable.

Network analyzers employ directional couplers to extract information from the waves transmitted through or reflected from the device under test (DUT) as illustrated in Figure 2.43. Quasioptical reflectometers such as the one presented in [86] use wire grid polarizers for extracting the reflected signal.

The purpose of this section, based on [49], is to take a closer look at the operating principle of a simple quasioptical setup for measuring the transmittance and reflectance of a DUT, and to confirm the operation of a realized setup by performing calibration measurements near 1 THz. Extraction of the phase information is not possible, but it could be done with a quasioptical six-port setup.

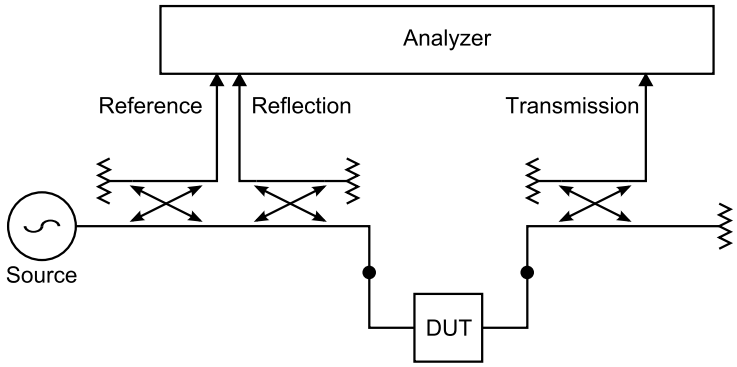

Figure 2.43: Simplified network analyzer block diagram.

2.6.1 Polarization

Since polarization plays an important role in the operation of the wire grid polarizers and in the reception of an incident wave with an antenna (and in the next chapter in Martin-Puplett interferometers), some basic aspects of polarization are reviewed here.

Polarization of an electromagnetic wave is defined by the evolution of the direction of the electric field vector in time in a plane perpendicular to the

propagation direction. Assuming a wave propagating in the z-direction, the electric field vector is given by

$$\vec{E} = \vec{x}E_1 \sin(\omega t - kz) + \vec{y}E_2 \sin(\omega t - kz + \delta), \tag{2.56}$$

where E_1 and E_2 are the amplitudes of linearly polarized waves in x- and y-direction, k the wavenumber and δ the phase difference by which E_y leads E_x. In a general case, the tip of the electric field vector draws an ellipse, a line and a circle being two special cases of elliptical polarization. The polarization ellipse can be described by the parameters shown in Figure 2.44.

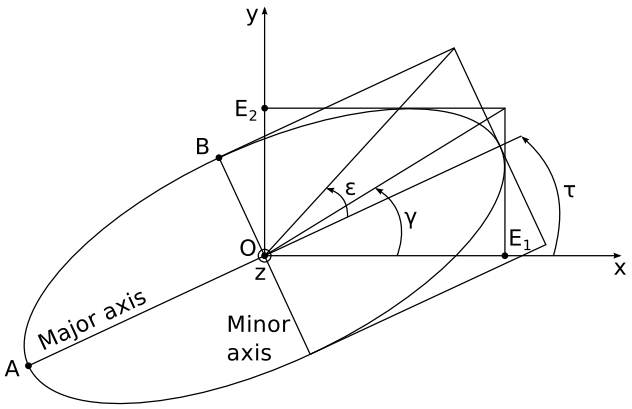

Figure 2.44: Polarization ellipse.

The polarization state of a wave can be described by a point on a Poincaré sphere. The latitude and longitude of the point are given by

$$\delta = 2\epsilon, \tag{2.57}$$

$$\lambda = 2\tau, \tag{2.58}$$

respectively, where the angle ϵ is related to the axial ratio $AR = OA/OB$ through the equation

$$\epsilon = \tan^{-1}\left(\frac{1}{\pm AR}\right), \tag{2.59}$$

and τ is the tilt angle of the polarization ellipse. The axial ratio and ϵ are negative for right-handed and positive for left-handed polarization as defined by IEEE.

The great circle angle between two polarization states (δ_w, λ_w) and (δ_a, λ_a) on a Poincaré sphere,

$$\Theta = \cos^{-1}\left(\cos(\delta_w)\cos(\delta_a)\cos(\lambda_w - \lambda_a)\sin(\delta_w)\sin(\delta_a)\right) \tag{2.60}$$

can be used to calculate the polarization matching factor for power between a wave and an antenna [54]

$$f = \cos\left(\frac{\Theta}{2}\right), \tag{2.61}$$

which expresses the fraction of the received power relative to the total incident power ($f \leq 1$).

2.6.2 Operating Principle

The quasioptical measurement setup is presented schematically in Figure 2.45. The operation of a directional coupler is realized with two free standing wire grid polarizers. The plane of wires is tilted 45° with respect to the incoming beam direction in both cases. The projected wire angles are 45° (G1) and 90° (G2) relative to the vertical.

A circularly polarized incoming beam from the THz-source (SRC) is first collimated with a parabolic mirror. The polarization component parallel to the wires is reflected while the orthogonal component is transmitted. The beam intensity is therefore halved at each wire grid. The reflected fraction can be measured or absorbed by an absorber. After the second wire grid, the vertically polarized beam is focused by another parabolic mirror to the DUT. The transmitted, vertically polarized signal is guided to the detector TM. A part of the incoming signal is reflected back towards the source from the DUT. G2 has no effect on it, since the polarization has not changed during the reflection, but G1 divides the signal equally between the detector RL and the source.

The signals arriving at the circularly polarized detectors TM and RL are linearly polarized in angles of 0° and 45° relative to the vertical. Since linear polarization can be split into two circularly polarized components with opposite polarization senses, only half of the incident wave power is detected.

Figure 2.46 shows the block diagrams of the measurements associated with the determination of the transmittance (T_D) and the reflectance (R_D) of a DUT. Assuming that 1) the alignment is perfect, 2) the source and detector are polarization matched in (a), 3) the polarization of the DUT is ideally matched to the incoming wave and to the detector in (d) and (e) and 4) cross-polarization and conduction losses are negligible, the following equations are

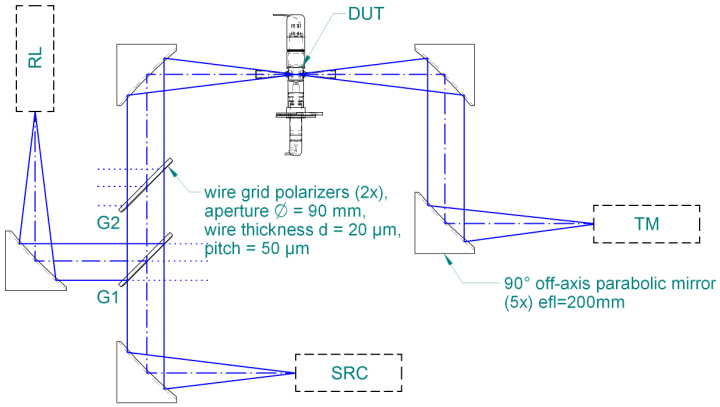

Figure 2.45: Quasioptical setup for determining the transmittance and reflectance of the DUT.

obtained:

$$P_R = P_0, \tag{2.62}$$
$$P_T = F_T P_0, \tag{2.63}$$
$$P_S = F_S R_S P_0, \tag{2.64}$$
$$P_{DT} = F_T T_D P_0, \tag{2.65}$$
$$P_{DS} = F_S R_D P_0 \tag{2.66}$$

where $P \propto V^2$ is the detected power, P_0 the detected power in a head-to-head measurement, R the reflectance, T the transmittance and F the total polarization matching factor for power. The factor F is a product of several polarization matching factors, $F = f_1 f_2 \dots f_i$, caused by polarization mismatches between a wave and an antenna. In addition to the detectors, also the polarizers are considered as antennas. They are linearly polarized in a direction perpendicular to the wires in transmission and parallel to them in reflection. First the total polarization matching factors in the thru and short measurements and then the transmittance and reflectance of the DUT are solved from the equations:

$$F_T = \frac{V_T}{V_R}, \tag{2.67}$$
$$F_S = \frac{1}{R_S}\frac{P_S}{P_R}, \tag{2.68}$$
$$T_D = \frac{1}{F_T}\frac{P_{DT}}{P_R}, \tag{2.69}$$
$$R_D = \frac{1}{F_S}\frac{V_{DR}}{V_R}. \tag{2.70}$$

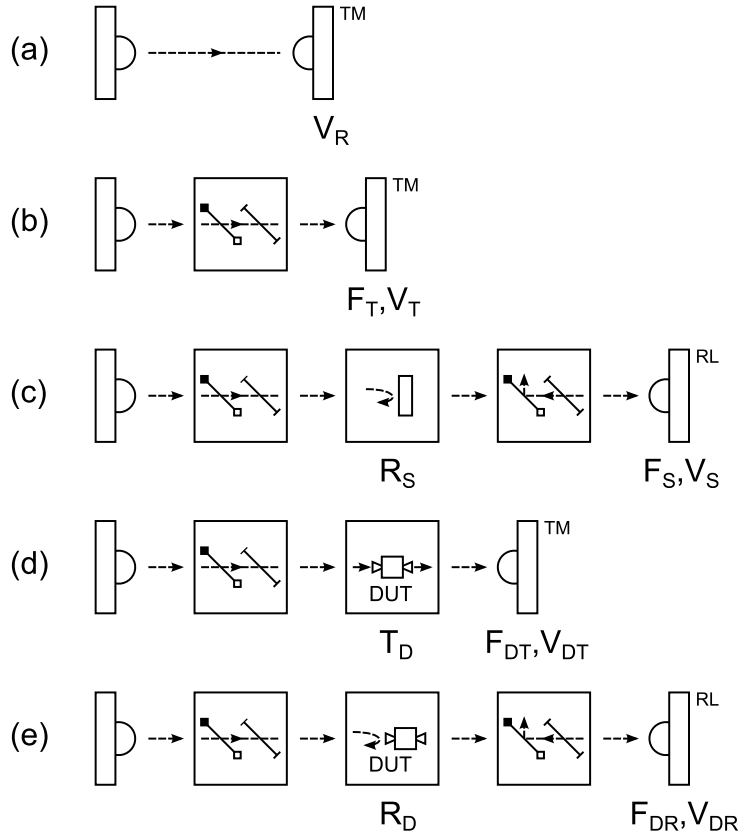

Figure 2.46: Block diagrams of the measurements for determining the transmittance and reflectance of the DUT: (a) reference, (b) thru, (c) short, (d) DUT transmission, (e) DUT reflection.

2.6.3 Characterization

Ion-implanted GaAs photomixers [11] with integrated log-periodic spiral antennas are used to characterize the operation of the measurement setup at 797 GHz and 1109 GHz by performing the calibration measurements (a)–(c) of Figure 2.46. The output power is a few dozen nanowatts while the dynamic range of the devices in a face-to-face configuration is over 55 dB, as depicted in Figure 2.47. The realized setup without the photomixers is shown in Figure 2.48. The source and the detector are driven by the beat signal of two distributed feedback lasers with an emission wavelength slightly above 800 nm. The amplitude of the emitted THz-signal is modulated by changing the bias voltage of the source photomixer in order to allow lock-in detection.

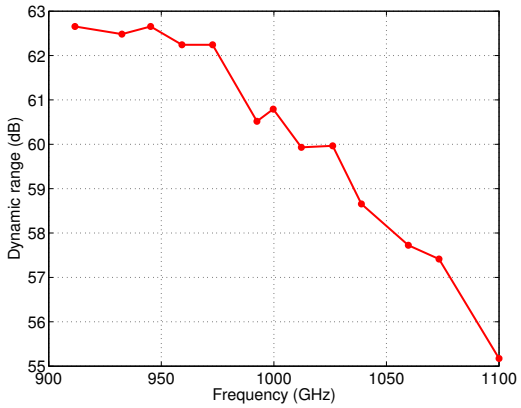

Figure 2.47: Dynamic range of the photomixers.

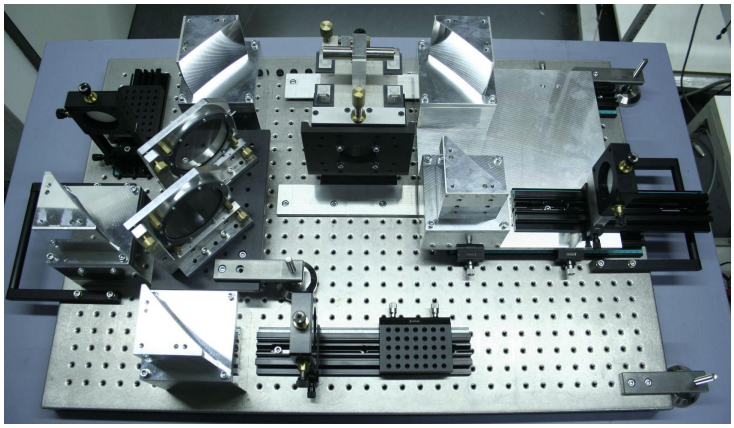

Figure 2.48: Realized measurement setup without the photomixers.

The direction of the wires of the polarizers is set by illuminating them with a visible light laser and by aligning the resulting diffraction patterns according to reference markers. Signal transmission from the source to the detector TM is measured without and with the wire grids (reference and thru). The reflected signal from a plane mirror, which is assumed to be perfectly reflecting ($R_S = 1$), placed at the position of the DUT is measured with the detector RL (short). Only one photomixer detector is available, so its place is alternated between the two detector positions. Table 2.6 presents the total polarization matching factors calculated from (2.68) and (2.69). The factor F_T at 1109 GHz is slightly lower than the one of an ideal setup, which can be caused by an imperfect alignment of the detector TM in the reference measurement. In addition to misalignment, deviation from the ideal total polarization matching factors is caused by the fact that the source and the

detector transmit and receive somewhat elliptical polarization. Depending on the tilt angle of the polarization ellipse, G1 may split the beam unequally or an amount different from half of the incident wave power may be detected. The axial ratios of the source and the detector are measured by placing them face-to-face, inserting a wire grid between them and rotating each photomixer until the minimum and maximum amplitudes are found. Both devices exhibit an axial ratio of about 1.2 at 797 GHz and 1.15 at 1109 GHz. Assuming an axial ratio of 1.2 and the worst case tilt angles of $\pm 45°$, the factor F_T calculated using (2.61) attains the values -8.3 dB and -9.9 dB and F_S the values -10.6 dB and -13.8 dB. Cross polarization of the wire grids causes further measurement uncertainty, but only to a smaller extent.

Table 2.6: Total polarization matching factors.

	Ideal setup	797 GHz	1109 GHz
F_T	-9.0 dB	-9.1 dB	-8.8 dB
F_S	-12.0 dB	-12.7 dB	-12.0 dB

3 QUASIOPTICAL DIPLEXER

Martin-Puplett Interferometers (MPI) [64] are utilized as diplexers in heterodyne receivers at millimeter and submillimeter wavelengths [26],[28],[97]. An MPI-diplexer combines the local oscillator (LO) signal and the signal of interest in such a way that their polarization states are identical at the diplexer output. A coherent mixer, sensitive only to a certain polarization direction, can then be used to down-convert the signal of interest to the intermediate frequency. This chapter, based [52], presents a study on characterization of imperfections in Martin-Puplett interferometers using ray-tracing.

3.1 Gaussian Beams

Although the characterization of imperfections is done in the following sections mainly in terms of ray-tracing, the following aspects related to the propagation of Gaussian beams are exploited.

Figure 3.1a illustrates the properties of a fundamental-mode Gaussian beam propagating in the z-direction. As the wave propagates along the z-axis, the amplitude distribution of the electric field retains its Gaussian form. The radius of the Gaussian beam is the distance w from the axis at which the amplitude of the electric field has decreased to a 1/e fraction of the maximum on the axis and is at a distance z from the beam waist, where w attains the minimum value w_0, given by the equation

$$w(z) = w_0 \sqrt{1 + \left(\frac{\lambda z}{\pi w_0} \right)^2}. \tag{3.1}$$

The equiphase surfaces of the beam are spherical with a radius of curvature

$$R(z) = z \left[1 + \left(\frac{\pi w_0^2}{\lambda z} \right)^2 \right], \tag{3.2}$$

as illustrated in Figure 3.1b.

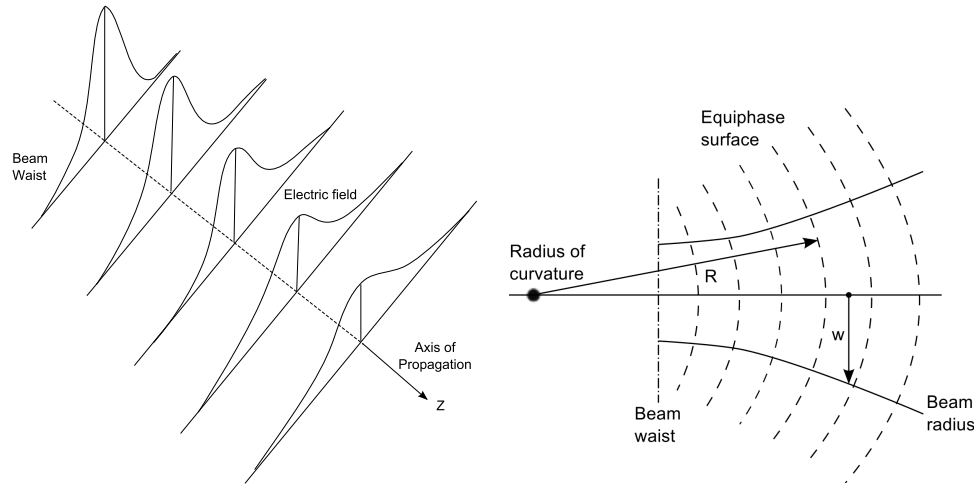

(a) (b)

Figure 3.1: (a) Electric field distribution and (b) radius of curvature of a Gaussian beam. Adapted from [32].

3.2 Martin-Puplett Interferometer

The optical paths of the signals in an MPI based diplexer are shown in Figure 3.2. The signal of interest E_s enters the interferometer by passing through the wire grid polarizer G1 with wires oriented along the y-axis. The wires of the polarizer G2 form a projected angle of 45° relative to the incident signal polarization, which causes the signal to split equally into two parts: the electric field component perpendicular to the wires (E_1) is transmitted to the movable roof mirror M1 and the parallel component (E_2) is reflected to the fixed roof mirror M2. Reflection from a roof mirror rotates the polarization direction 90°, so the roles of the returning signal components are interchanged: E_1 is reflected from the grid G2 while E_2 passes through it. The two components then interfere to form the output signal. The LO-signal enters the interferometer by reflecting from the wire grid G1 and propagates further like E_s.

A wavelength dependent phase shift of E_1 relative to E_2 is introduced by moving the roof mirror M1 in z-direction. This causes the polarization of the output signal to change and, when a specific polarization is used for receiving, the detected amplitude to vary sinusoidally. If the path length difference of the components E_1 and E_2 is $2d \approx \lambda_{if}/2$, both E_{LO} and E_S exit the diplexer with the same linear polarization.

Imperfections of the quasioptical components originating from misalignment

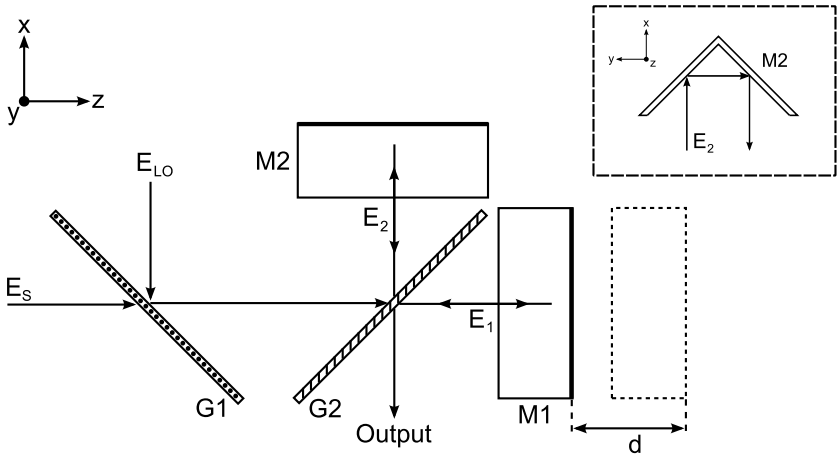

Figure 3.2: Martin-Puplett Interferometer as a diplexer. Mirror M1 is moved a distance $d \approx \lambda_{if}/4$ to obtain correct operation.

and manufacturing accuracy cause the phase difference between E_1 and E_2 to deviate from the desired value leading to an incorrect polarization state. The mixer rejects the cross polarization components of the LO-signal and the signal of interest, which leads to degraded receiver sensitivity. In a single-pixel receiver, the phase error can be compensated by adjusting the position of M1, but in a multi-pixel system, the phase error being generally different for each pixel, much stricter alignment is required.

An analysis of the Martin-Puplett interferometer with imperfections has been presented in [57]. Non-ideal polarization rotation of roof mirrors has been studied in [90] and the effect of roof mirror rotation around the roof line in [80]. Wire grid polarizers with uneven wire spacing are discussed in [63]. In this chapter, the imperfections of the quasioptical components are studied with ray-tracing simulations, in which the path length differences between E_1 and E_2 for rays entering the diplexer at different input aperture positions are calculated. Several parameters describing the rotation, translation and deformation of the components are defined and a parameter sweep is performed to find a parameter set that most accurately reproduces the path length differences measured in a test diplexer. Measurement results supporting the predictions given by the simulations are presented. The same process is repeated to find out the imperfections in the diplexer of a multi-pixel THz-receiver installed at a radio telescope. Simulations may provide useful information on how to improve the receiver performance by removing or compensating the imperfections.

3.3 Ray-tracing Simulations

Ray-tracing simulations are performed with MATLAB according to the procedure described in [84]. A ray representing a Gaussian beam is defined with an initial position $\bar{p}_0 = (\bar{p}_{0,x}, \bar{p}_{0,y}, \bar{p}_{0,z})$ and direction cosines $\bar{r}_0 = (\bar{r}_{0,x}, \bar{r}_{0,y}, \bar{r}_{0,z})$ in a cartesian reference coordinate system $\bar{O}$. The components of the interferometer are modeled with surfaces defined by equations of the form $S(x, y, z) = 0$. The imperfections involve translations and rotations of the components. The surface equations are not changed, but a rotated coodinated system O is introduced. In order to calculate the intersection point between the ray and a surface of a misaligned component, the initial position of the ray is transformed into the new coordinate system:

$$\bar{p}_0 - \bar{s} = Rp_0, \tag{3.3}$$

$$p_0 = R^{-1}\left(\bar{p}_0 - \bar{s}\right), \tag{3.4}$$

where p_0 is the position of the ray in the new coordinate system O and $\bar{s}$ the translation of the coordinate system O (i.e. the component) as measured in the reference system $\bar{O}$. The rotation matrix is

$$R = R_x(\theta_x)R_y(\theta_y)R_z(\theta_z) = \begin{bmatrix} 1 & 0 & 0 \\ 0 & \cos\theta_x & -\sin\theta_x \\ 0 & \sin\theta_x & \cos\theta_x \end{bmatrix} \begin{bmatrix} \cos\theta_y & 0 & \sin\theta_y \\ 0 & 1 & 0 \\ -\sin\theta_y & 0 & \cos\theta_y \end{bmatrix} \begin{bmatrix} \cos\theta_z & -\sin\theta_z & 0 \\ \sin\theta_z & \cos\theta_z & 0 \\ 0 & 0 & 1 \end{bmatrix}, \tag{3.5}$$

where the angles θ_x, θ_y and θ_z define how much a component is rotated around each axis. In order to allow the use of the same rotation matrix as in the transformation of the coordinate axes of O, a rotation of the rotated point back to the original position is considered in (3.3). The direction cosines of the ray are rotated by using the same idea:

$$\bar{r}_0 = Rr_0, \tag{3.6}$$

$$r_0 = R^{-1}\bar{r}_0. \tag{3.7}$$

Now the rotated ray (p_0, r_0) propagates straight ahead a distance t until it intersects with a surface $S(x, y, z) = 0$. The intersection point is

$$p_i = (p_{0,x} + tr_{0,x}, p_{0,y} + tr_{0,y}, p_{0,z} + tr_{0,z}) \tag{3.8}$$

and the distance t is computed from

$$S(p_{x,0} + tr_{x,0}, p_{y,0} + tr_{y,0}, p_{z,0} + tr_{z,0}) = 0. \tag{3.9}$$

For example, in the case of the x-z-plane, $y = 0$, the distance is

$$p_{y,0} + t r_{y,0} = 0 \tag{3.10}$$

$$t = -\frac{p_{y,0}}{r_{y,0}}. \tag{3.11}$$

The ray propagates the same distance t also in the reference coordinate system, so the intersection point in $\bar{O}$ is

$$\bar{p}_i = \left(\bar{p}_{x,0} + t\bar{r}_{x,0}, \bar{p}_{y,0} + t\bar{r}_{y,0}, \bar{p}_{z,0} + t\bar{r}_{z,0}\right). \tag{3.12}$$

The direction of the reflected ray is calculated from the equation

$$\bar{r}_r = \bar{r}_0 - 2\bar{r}_{0,\perp} = \bar{r}_0 - 2\left(\bar{n} \cdot \bar{r}_0\right)\bar{n}, \tag{3.13}$$

where $\bar{r}_{0,\perp}$ is the component of the incoming ray parallel to the surface normal $\bar{n}$. The surface normal n in O is given by the gradient at the intersection point p_i

$$n = \nabla S(p_{i,x}, p_{i,y}, p_{i,z}). \tag{3.14}$$

It is rotated to obtain the surface normal at the reference coordinate system:

$$\bar{n} = Rn. \tag{3.15}$$

The LO-signal and the wire grid G1 are not present in the simulations. The ray first intersects with the polarizer G2. At this point the ray is divided into two rays: one is reflected and the other is transmitted. After each ray has reflected from both surfaces of the respective roof mirror and returned to the polarizer G2, the difference in their path lengths is calculated. The rays may hit the polarizer in different spots and may be tilted in respect to each other causing beam coupling losses. They are, however, small compared to the polarization losses originating from the incorrect path length difference and are therefore neglected.

Figure 3.3 illustrates the dimensions of the components and the parameters describing the imperfections. Numerical values for the dimensions are given in Table 3.1. The system has many additional degrees of freedom, but the selected parameters suffice to describe the occurring phenomena, have a clear physical meaning and allow a direct comparison with measurements.

In addition to the translations and rotations shown in Figure 3.3b, a parameter describing the deformation of the wire grid polarizer is included. It is assumed that the elliptical frame of the polarizer with major and minor axes a and b is bent in such a way that the minor axis forms a parabola. The deformation is described with the parameter GD which is the height difference

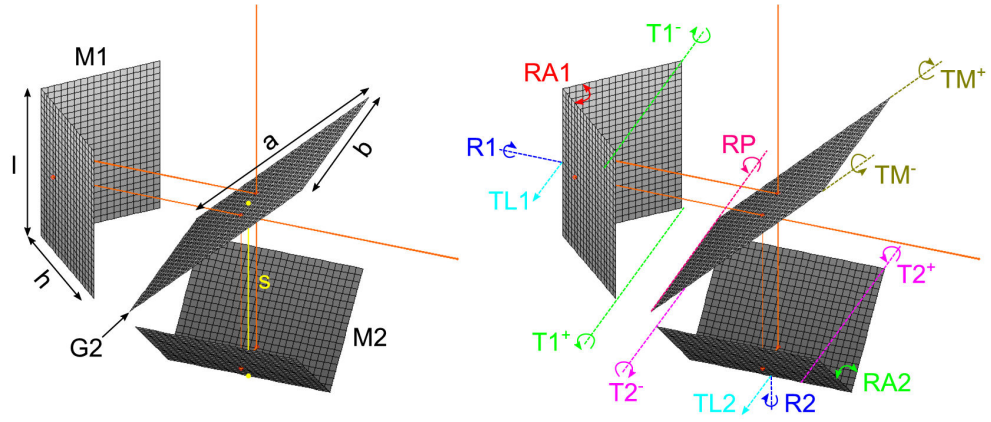

(a) (b)

Figure 3.3: (a) Component dimensions and (b) parameters describing the imperfections. Orange lines show the path of an example ray. RA1 (RA2) is the deviation of the roof angle from 90°. M1 (M2) can be translated along the axis TL1 (TL2) and rotated around the axis R1 (R2), $T1^-$ ($T2^-$) or $T1^+$ ($T2^+$). Rotation around the axis $T1^-/T1^+$ ($T2^-/T2^+$) is realized by lifting the opposite end of the mirror; therefore a measure of length is given instead of an angle. The rotation of the wire grid polarizer around the axis RP or TM^-/TM^+ is also considered as lifting of the opposite side.

Table 3.1: Component dimensions.

l [mm]	h [mm]	a [mm]	b [mm]	s [mm]
120	120.7	180	130	109.7

between the center point and the end points of the parabola (Figure 3.4a). The polarizer is modeled in simulations as a solid surface which is obtained by spanning straight wires in an angle of 35.3° across the bent frame (Figure 3.4b) and fitting a surface on the wires (Figure 3.4c). A saddle surface,

$$x = a + by^2 + cz^2, \tag{3.16}$$

the coefficients of which are given by the fit, describes the surface of the wires well. The rays are reflected from or transmitted through the surface, but no polarization effects or losses are taken into account.

Figure 3.5 shows example outputs of virtual raster scans when the incident ray position is scanned within an area of 60 mm × 60 mm with a resolution

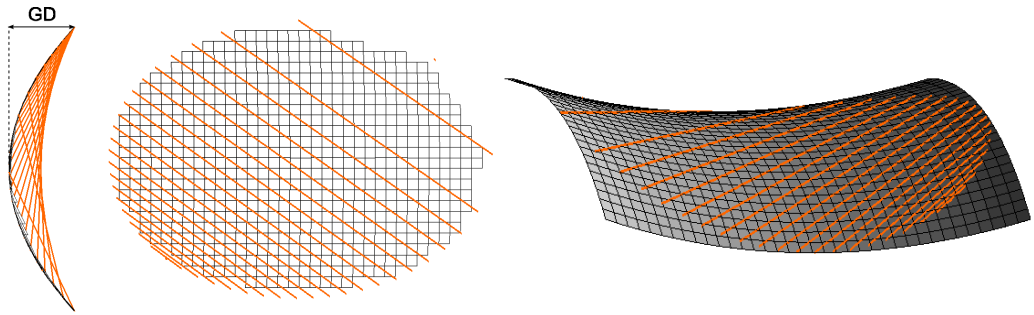

(a) (b) (c)

Figure 3.4: Wires spanned on an elliptical frame: (a) top view, (b) front view. (c) A saddle surface fit to the wires.

of 13 × 25 pixels. If $d_{x,y}$ is the position correction of mirror M1 needed for achieving a path length difference equal to $\lambda_{if}/2$ ($f_{if} = 6$ GHz) between the interferometer arms at pixel position (x,y), the figure shows the mirror position correction relative to the center pixel, $\Delta d_{x,y} = d_{x,y} - d_{0,0}$.

When no imperfections are introduced in the simulation, Δd is zero for each pixel position. When the mirror M2 is rotated around $T2^-/T2^+$, a slope along the x-axis appears. The effect of rotating M2 around $T2^-$ by lifting the opposite end is shown in Figure 3.5a. The same effect can be achieved by rotating the wire grid G2 around the axis RP, and compensation of the misalignment effect caused by one component is possible by misaligning the other. Symmetric vertical slopes on both sides of the roof line $y = 0$ are created when the roof angle of M2 deviates from 90° by an amount RA2 (Figure 3.5b). Rotation of M2 around R2 by a small angle leads to a nearly vertical slope (Figure 3.5c) which can be compensated for by a rotation of G2 around TM^-/TM^+ (Figure 3.5d). The rotation of the slope becomes clearly visible at large angles of R2. Figure 3.5e demonstrates the effect of frame deformation and contains, as one might expect, more round features. Translation of M2 along TL2 has no effect alone as long as the ray does not miss the mirror, but appears when another parameter is introduced (Figure 3.5f). Whenever M2 is concerned, one could alternatively change the respective parameter of M1 with the same amount or, excluding TL1 and TL2, the respective parameters of both mirrors to obtain identical results.

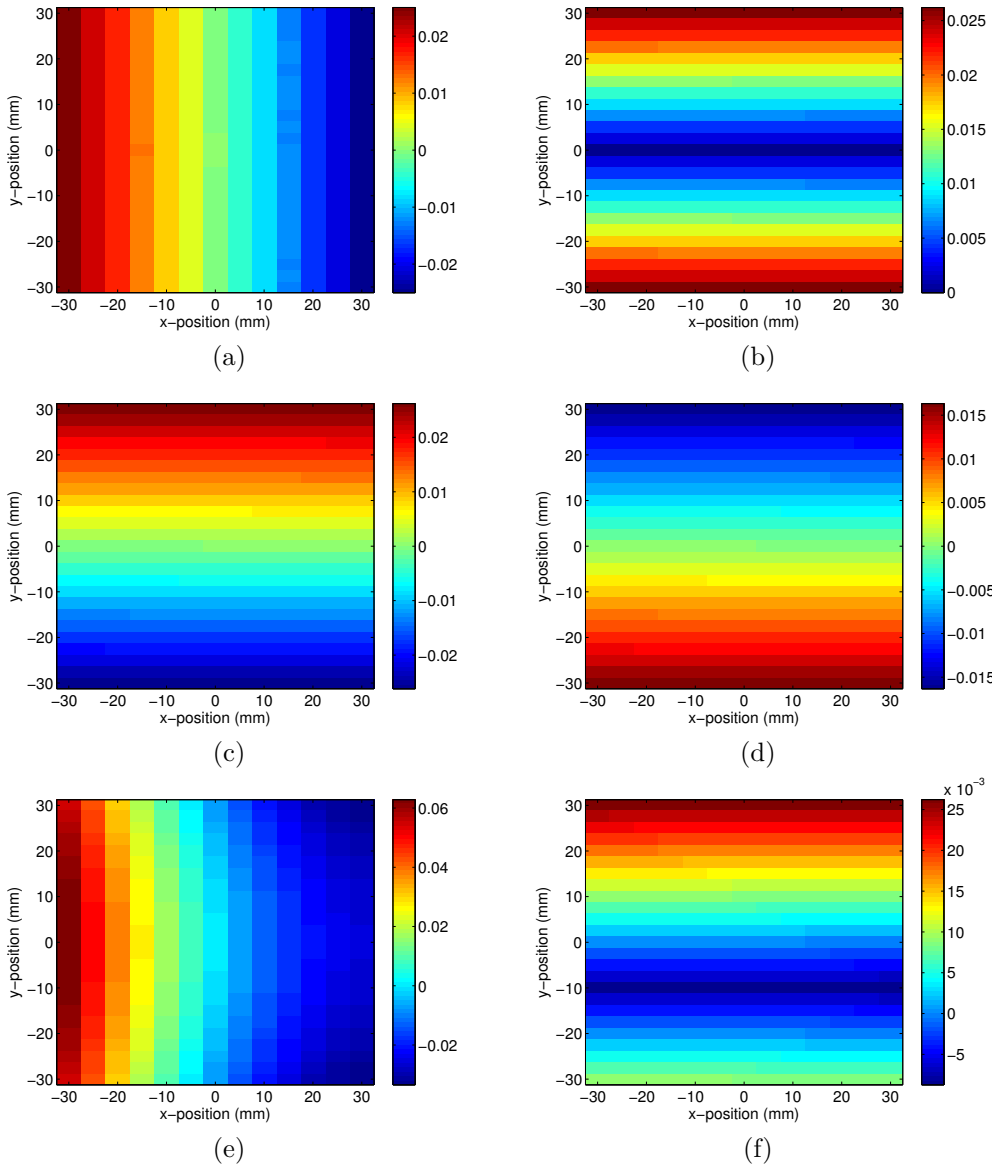

Figure 3.5: Simulated relative mirror position corrections Δd in the case of different interferometer imperfections introduced to the ideal configuration. Colors show Δd in millimeters. (a) Rotation around T2$^-$ by lifting 50 µm, (b) roof angle deviation RA2 50 mdeg, (c) rotation around R2 by 50 mdeg, (d) rotation around TM$^+$ by lifting 50 µm, (e) bending of the frame by setting GD to 50 µm, (f) roof angle deviation RA2 50 mdeg and translation along TL2 by 10 mm.

3.4 Diplexer Measurements

An MPI based diplexer, the CAD model of which is shown in Figure 3.6, is measured to provide comparison data for the ray-tracing program. A solid state frequency multiplier and a sub-harmonic mixer equipped with corrugated horns are used to launch and receive a Gaussian beam at 480 GHz. Both the source and the detector are connected to a vector network analyzer from AB Millimetre and mounted on computer controlled linear tables which allow precise setting of the beam location at the input aperture and the movement of the detector according to the source movement at the output aperture to maximize the received signal amplitude.

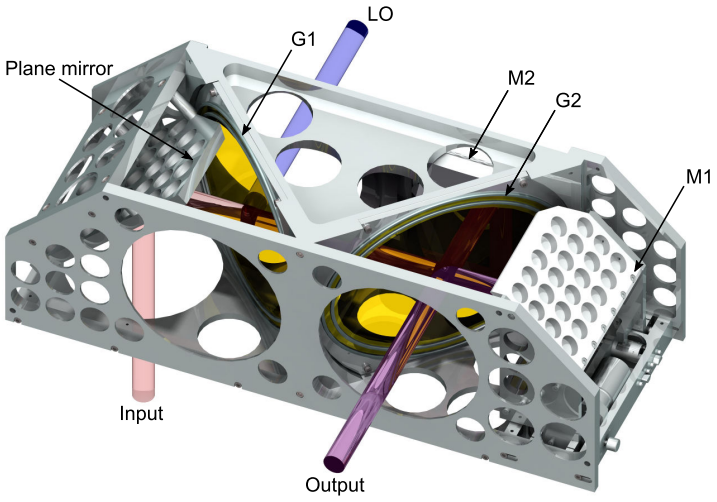

Figure 3.6: CAD model of the measured diplexer and the optical paths of the beams. The component dimensions are as in Table 3.1. The LO-beam and the wire grid G1 were not present during the measurements.

The capability of the vector network analyzer to measure the phase of the signal is utilized in the initial alignment of the detector. First, the source is centered at the input aperture. Then the detector is moved along an arc with a radius of curvature calculated with (3.2), as shown in Figure 3.7. Ideally, the detector moves along the equiphase line and the measured phase is constant as in Figure 3.8a. If the detector does not reside on the optical axis or if the radius curvature is incorrect enough, the detector crosses one or several equiphase lines (surfaces) and the measured phase as a function of position looks like the one in Figure 3.8b. Figure 3.8b shows the situation when the detector position is correct, but the radius of curvature is

slightly incorrect. After the detected signal has been maximized by moving the detector, a small absorber patch is moved at the output aperture of the diplexer to ensure that maximum signal attenuation occurs when the patch is at the center of the aperture, meaning that the source is not tilted in any direction.

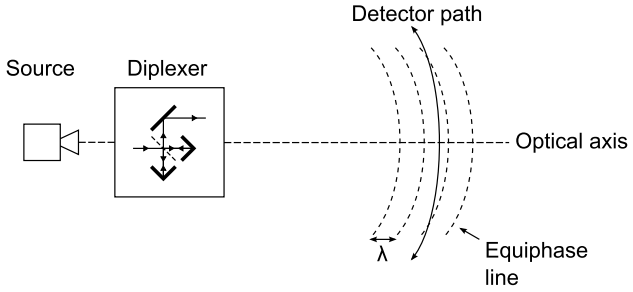

Figure 3.7: Alignment of the detector.

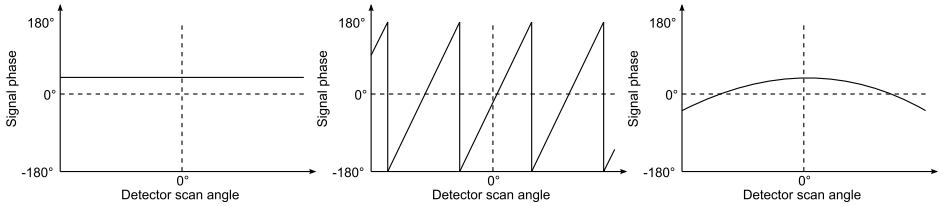

Figure 3.8: Detected phase as a function of detector position: (a) detector moves along an equiphase line, (b) detector crosses equiphase lines due to incorrect positioning, (c) correct detector position, but incorrect radius of curvature.

A raster scan with a resolution of 13 × 25 pixels and a range of 60 mm × 60 mm is performed by moving the source at the input aperture. At each pixel position, the output signal amplitude is measured as a function of the roof mirror M1 position by sweeping it about the position $s + \lambda_{if}/4$. The transmission responses of the three different pixels in Figure 3.9a should ideally overlap, but due to unequal path lengths the transmission minima (and maxima) are obtained at different mirror positions. The relative mirror position corrections Δd are calculated by comparing the minima positions to the reference which is the transmission response minimum of the center pixel.

The radius of the beam waist is about 6 mm, the total path length approximately 780 mm and the beam radius therefore, from (3.1), 27 mm at the

output aperture. As the output aperture has a radius of 67 mm, some beam blockage occurs at pixels near the corners of the scanned area, as illustrated in Figure 3.9b. The transmission responses, including those of the corner pixels, possess the sinusoidal characteristics predicted by interferometer analysis based on geometrical optics [58], which provides confidence on the validity of the ray-tracing simulations.

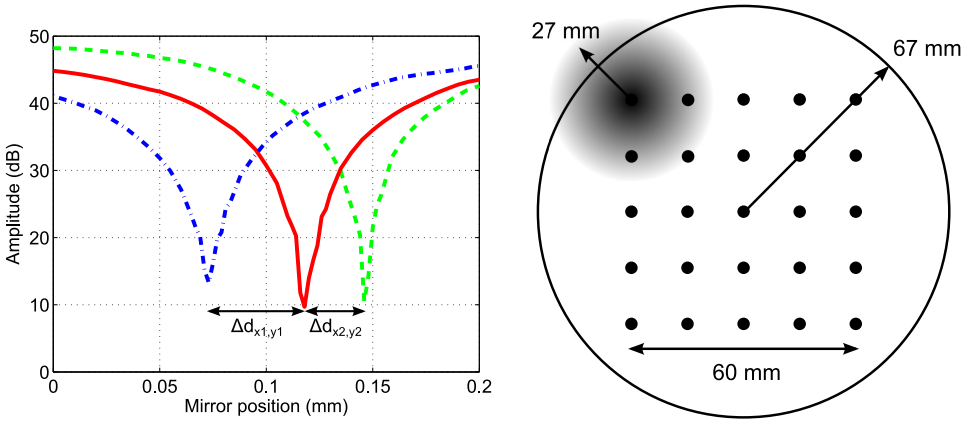

(a) (b)

Figure 3.9: (a) Measured transmission responses of the center pixel (solid) and two corner pixels, and (b) beam blockage at the output aperture.

Five in-house manufactured polarizers numbered from 1 to 5 with a wire thickness of 20 µm and a period of 60 µm are used in the measurements. A flatness measurement of a polarizer frame with a coordinate measuring machine (CMM) before the winding of the wires, presented in Figure 3.10, supports the type of deformation implemented in the simulations and indicates a worst case GD of 92 µm, while those resulting from the simulations exhibit the same order of magnitude. The CMM measurements show the roof angle of M2 to be 90.022°, whereas cumbersome disassembling and subsequent aligning prevents the moving mirror to be characterized.

Figure 3.11a and Figure 3.11b show the measured relative mirror position corrections for the polarizers 1 and 2 and Figure 3.12 for the polarizers 3 and 4. Values up to about ±50 µm are typical for all polarizers. The rotation of the polarizers by 180° does not have qualitative effects on the patterns, which is in agreement with the symmetry of the saddle surface.

A simulated parameter sweep is made in order to reproduce the measurement results. The misalignment parameters included in the sweep are given in Table 2, while the others maintained the value of an ideal interferometer, except

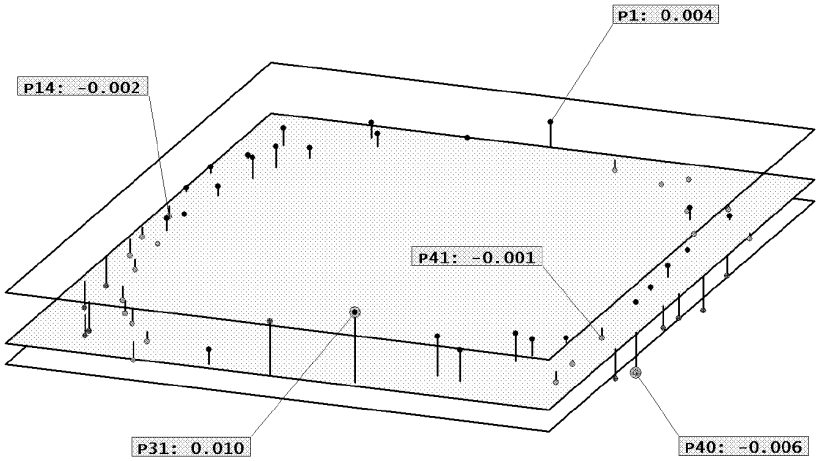

Figure 3.10: Flatness of a polarizer frame measured before the winding. Deviation from the reference plane is given in millimeters.

RA2 which is fixed to the measured value of 22 mdeg. These parameters are sufficient to cause each effect of Figure 3.5, but they are not necessarily the real origin, since other parameters of Figure 3.3b may also bring about the same effects. In spite of this, the information provided by the sweep can be used to improve the alignment; for example, the parameter R2 can be interpreted as the sum R1 + R2 and an adjustment of the polarizer according to RP helps even if the real cause is a tilted roof mirror. Simulated relative mirror position corrections are subtracted from the measured ones for each parameter set, $\Delta d_{meas} - \Delta d_{sim}$, and the root mean square (RMS) difference is calculated. A minimum of about 3 µm is obtained for both polarizers, and the resulting patterns, presented in Figure 3.11c and 3.11d, match the measurements very well.

Table 3.2: Parameter sets that minimize the difference between the measured and simulated Δd in the case of two different polarizers. The confidence limits originate from the step sizes of the parameter sweep which were refined until there is practically no change between the RMS differences of neighboring values.

Parameter	TL2 [mm]	RP [μm]	GD [μm]	RA1 [mdeg]	R2 [mdeg]
Polarizer 1	-7.4 ± 0.05	-61 ± 0.5	60 ± 0.5	-36 ± 0.5	-9 ± 0.5
Polarizer 2	-7.7 ± 0.05	57 ± 0.5	-12 ± 0.5	-27 ± 0.5	0 ± 0.5

The two simulation results are consistent in the sense that the parameters

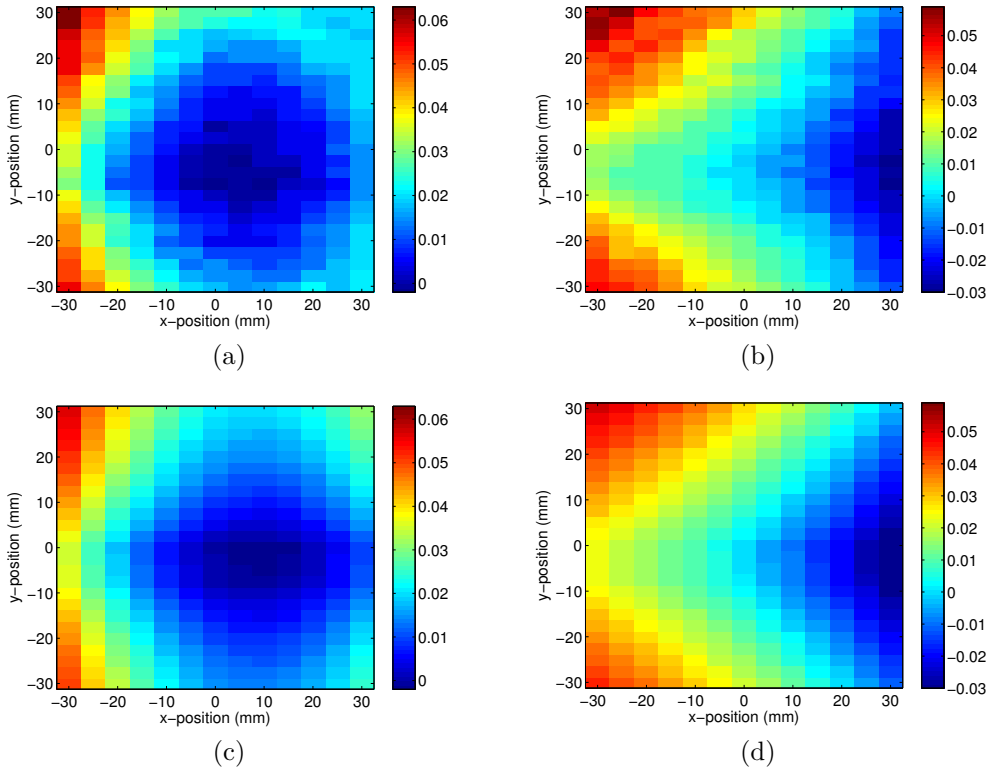

Figure 3.11: Measured mirror position corrections for (a) the polarizer 1 and (b) the polarizer 2. Panels (c) and (d) show the respective simulations. Colors show the value of Δd in millimeters.

not related to the polarizer (TL2, RA1 and R2) differ only by a relatively small amount from each other. The parameter TL2 is unexpectedly large, but, in addition to TL1, no other parameter or parameter combination has been found that could produce the same effect. As the construction of the diplexer allows M1 to be translated laterally relatively easy, it is suspected that the origin of the TL2 value is actually M1 which has been accidentally displaced during a polarizer change.

Figure 3.13 demonstrates the evolution of the measured relative mirror position corrections for the polarizer 5 when M2 is rotated around $T2^{+}$. The initial misalignment causing the horizontal slope is compensated relatively well with a tilting of 60 µm in Figure 3.13b. As the mirror is tilted 40 µm more in Figure 3.13c, the slope becomes steeper and exhibits the opposite sign.

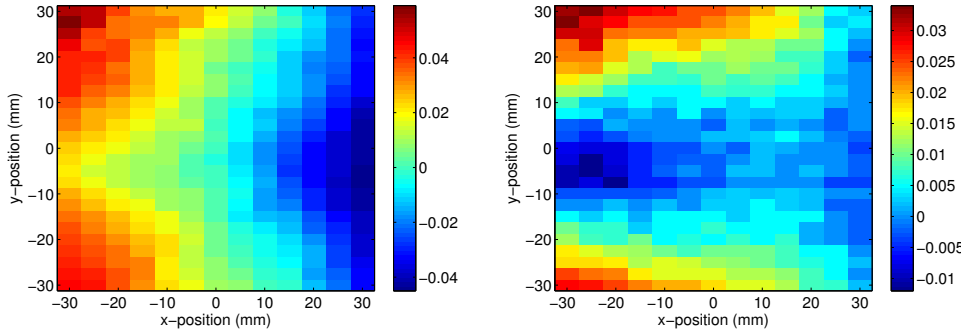

(a) (b)

Figure 3.12: Measured mirror position corrections for the polarizers (a) 3 and (b) 4. Colors show the value of Δd in millimeters.

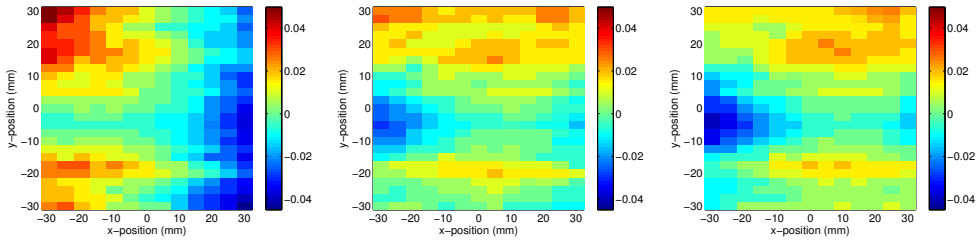

(a) (b) (c)

Figure 3.13: Rotation of M2 around T2$^-$: a) 0 µm, b) 60 µm and c) 100 µm. Colors show the value of Δd in millimeters.

3.5 Multi-Pixel Receiver Measurements

Martin-Puplett interferometers identical to the one measured in Section 3.4 are utilized as diplexers and single-side band filters at cryogenic temperature in the CHAMP$^+$ multi-pixel THz-receiver operated by the Max Planck Institute for Radio Astronomy at the APEX telescope in Chile [44],[45]. CHAMP$^+$ has two frequency bands centered at 660 GHz and 850 GHz. The positions of the seven beams of the low frequency band diplexer are marked with encircled numbers in Figure 3.15.

Mirror position corrections relative to the center pixel are measured at each beam position (meas1) as described in the previous section, and a simulated parameter sweep (sim1) with parameters listed in Table 3.3 is performed to reproduce the measurement results. Other parameters assume the values of an ideal instrument. No information about the roof angle RA1 is available, and therefore the parameter RA2 has actually the meaning RA2 - RA1.

Table 3.3: Parameter set minimizing the difference between the measured and simulated Δd in the case of the CHAMP$^+$ diplexer. The confidence limits have the same meaning as in Table 3.2.

Parameter	TL2 [mm]	RP [μm]	GD [μm]	RA2 [mdeg]	R2 [mdeg]
sim1	-2.7 $\pm$ 0.05	1 $\pm$ 0.5	-22 $\pm$ 0.5	10 $\pm$ 0.5	-6 $\pm$ 0.5

Another measurement is performed with the roof mirror M2 rotated around T2$^-$ by lifting the opposite end 40 µm (meas2). The same is done also in the simulation (sim2) while keeping the other parameters fixed to the values given in Table 3.3. The relative mirror position corrections of the measurements and the simulations are plotted in Figure 3.14. The initial measurement is reproduced very accurately with the given parameters (RMS difference 0.4 µm). The most significant difference between the measured and simulated curves after the mirror tilting is the absence of the peak at beam position 3 leading to a five times greater RMS difference. Figure 3.15 shows the results of simulated 2D raster scans with the parameter sets of sim1 and sim2.

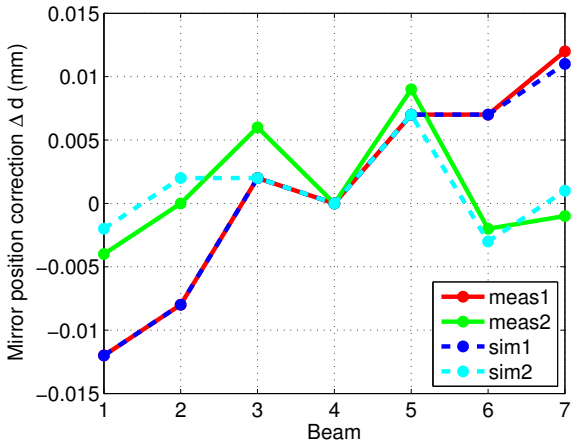

Figure 3.14: meas1 and meas2 are the measured relative mirror position corrections at the pixel positions of Figure 3.15 before and after the rotation of M2 around T2$^-$, and sim1 and sim2 are the corresponding simulations.

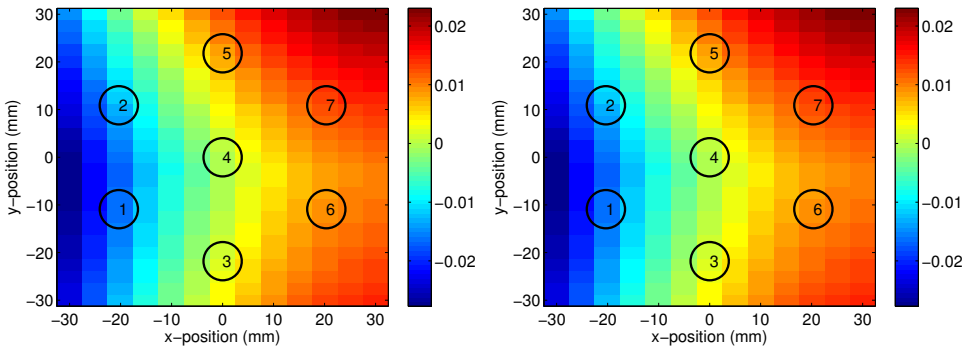

(a) (b)

Figure 3.15: Simulated relative mirror position corrections (a) before (sim1) and (b) after (sim2) the rotation of M2 around T2$^-$. Encircled numbers show the beam positions and colors show the value of Δd in millimeters.

3.6 Results

The effects of roof mirror alignment and angle deviation as well as the effects of rotation and deformation of the frame of the polarizing wire grid on optical path lengths in a Martin-Puplett interferometer have been studied with ray-tracing simulations and verified using measurements. Five parameters describing such imperfections have been found sufficient to accurately reproduce the measured path length differences in two interferometers used as diplexers. The obtained parameter values are on the order of dozens of micrometers or millidegrees, the only exception being the lateral shift of a roof mirror by several millimeters, which is suspected to be a result of an accidental impact during the change of a polarizer. Unfortunately, no measurement data are available to confirm the shift of the mirror. The roof angle deviations, the polarizer frame deformation and the effect of roof mirror tilting predicted by the simulations are, however, in good agreement with the measurements. There are several ways to produce the same optical path length differences, so some information on the imperfections of the characterized interferometer is needed to find an unambiguous description of the device. Nevertheless, if optical path length differences are known at several pixel positions, ray-tracing simulations may provide valuable insights on how to improve the performance of a receiver by correcting the quasioptical assembly of the interferometer.

4 CONCLUSION

The sensitivity of radio astronomical receivers has reached a level, at which a considerable reduction in observing time is possible only by increasing the number of pixels in the receiver. However, the development of multi-pixel receivers is severely hindered at terahertz frequencies by the lack of local oscillator power. Imperfect optical coupling of the signal and local oscillator power to the mixers complicates the situation further. This dissertation attacked these crucial issues by proposing the use of vacuum electronic amplifiers for the amplification of the LO-signal and discussing their development in detail as well as by introducing a new method for finding the defects in a Martin-Puplett interferometer based diplexer with an in-house developed ray-tracing program.

A terahertz traveling wave tube with a helix slow wave structure has the potential of providing amplification on a broad frequency band making it a perfect match for a highly tunable low-power solid state or photonic local oscillator. However, the small dimensions of the helix SWS at terahertz frequencies require microfabrication. A helix configuration that is compatible with state-of-the-art microfabrication methods was introduced, and a design method was described. The compability has been achieved by adopting a square shape and a supporting quartz substrate. In order to realize a traveling wave tube, efficient signal coupling structures for the input and output ends of the helix are required. The design of input/output couplers is restricted by the fact that the path of the electron beam must remain free. Several structures have been designed and simulated as part of this dissertation to enable coupling from a rectangular waveguide to the helix: a post-probe, a patch-probe and a ridge waveguide were used to couple the signal to a coplanar waveguide, after which a transition to the helix took place. The ridge and patch-probe transitions provided larger bandwidths than the post-probe transition. A three dimensional particle-in-cell simulation of a traveling wave tube utilizing the designed square helix SWS in combination with the designed couplers has been performed. To author's knowledge, such simulations have not been carried out before. The TWT

exhibits a small-signal gain of 18.3 dB at 825 GHz and a 3-dB bandwidth of 69 GHz ($\Delta f/f = 8\%$) with post-couplers. The maximum simulated output power is 25.8 dBm. The use of wide-band transitions led to oscillations in the simulation, the reason for which is possibly a parasitic substrate mode, but a more rigorous study of the instability remains to be done. Nevertheless, the performance obtained with the post-couplers demonstrates the tremendous potential of the device. The square helix and the post-couplers are ready for fabrication.

Although the concept of frequency multiplication with linear beam traveling wave tubes has been known for some time, the exploitation of harmonic signal power generated by a dedicated TWT multiplier has seldom been pursued. In this work, a single-stage 850-GHz TWT is shown to exhibit a simulated conversion efficiency of 7% to the second harmonic at 1700 GHz for an input power of 25 mW which is comparable with the efficiencies of state-of-the-art solid-state doublers. It may be concluded that a substantial amount of power can be generated even though the signal at the second harmonic does not interact with the electron beam. The input/output couplers of the square helix TWT can be directly used at the input of the doubler, but further work is needed on the design of an output coupler which separates the fundamental and harmonic signals. The power at the fundamental frequency may be notable, and if reflected from the output coupler, unstable operation of the device may occur.

Moreover, this dissertation discussed a first-of-its-kind 1-THz cascade backward wave amplifier based on a double-corrugated waveguide SWS. The combination of a CBWA and a DCW-SWS allows more relaxed manufacturing requirements than the square helix TWT. The matching of a DCW-SWS to a rectangular waveguide has been realized in three different ways. The first structure exploited height tapering of the corrugations, but while providing excellent performance over a wide band, its microfabrication turns out to be difficult. In the second structure, the height of the corrugations was kept constant, but the distance between them in the transverse direction was tapered linearly until the corrugations merged with the waveguide side walls. The number of corrugations in the distance taper needed to be approximately doubled in order to attain similar matching performance with the height tapering. Hence, to minimize the coupler length while keeping the corrugation height constant, a third coupler type was introduced. Not only the distance between the corrugations in the transverse direction was tapered nonlinearly, but the corrugations were also made so wide that the other end touched the waveguide side walls. This novel coupler was shown to provide a -10 dB bandwidth of 250 GHz for a length of just 475 μm. Both the linear

distance taper and the nonlinear distance taper structure were realized with X-ray LIGA.

The loss per SWS period is essential for deciding on the correct SWS length when a certain amplifier gain is desired. Slow wave structure samples with different lengths were realized in order to measure the losses of the DCW-SWS at 1 THz. Unfortunately, the manufactured structures were malfunctioning, and therefore the losses could not be extracted. It was shown, using simulations, that an excess height of only a few corrugations is enough to attenuate the transmitted signal to the level exhibited by the measurements. Missing corrugations were shown to be important primarily from the point of view of the return loss, especially if the corrugations were missing near the input port. As the structures are periodic and the defects are related mainly to the height of the corrugations, it could be possible to synthesize the measured S-parameters from simulated scattering matrices of single corrugation periods with varying heights. In any case, the performed simulations provided important information on how the efforts to improve the manufacturing process should be targeted.

Both the traveling wave tube and the cascade backward wave amplifier require a high to ultra-high vacuum to operate correctly. The vacuum envelope is sealed with vacuum windows, through which the input and output signals have to pass. The window has to be manufactured from a material which withstands the high temperatures during the baking of the tube, and its dimensions have to be large enough to provide sufficient mechanical stability. The mounting of the window in an input/output waveguide makes the electromagnetic design relatively uncomplicated, but the small size of a 1-THz waveguide necessitated other placement. A novel configuration consisting of a dual-mode horn with an integrated quartz window has been proposed. The window was placed between two separate flaring sections of the horn, which allows the use of a larger window diameter. However, the window and the vacuum envelope disturb the fields inside the horn, which made the design very challenging. Although further improvement in the geometry of the discontinuity creating the higher order mode in the horn is possible, the far-field radiation pattern simulations have clearly evidenced the improved beam symmetry and lower sidelobes over a single-mode horn. The far-field radiation pattern of the horn has also been calculated by performing a Gauss-Laguerre analysis, and good agreement between the radiation characteristics has been obtained. The Gauss-Laguerre method is fast and allows the effect of phase difference and amplitude ratio between the modes to be investigated easily, while the huge amount of mesh cells in the 3D simulations can be dealt in a reasonable time only with powerful CPU/GPU clusters. The bandwidth of

the dual-mode horn is limited by the resonant character of the window rather than the in-phase condition of the modes, and may be extended by making holes or grooves into the surfaces of the window. This will be addressed in future work.

An essential step in the development of a THz-amplifier is the experimental characterization of the amplification performance. Sources, detectors and other measurement equipment at 1 THz are, however, expensive and rarely available. Hence, a general-purpose quasioptical measurement setup based on two free-standing wire grid polarizers for measuring the transmittance and reflectance of a device under test has been designed and built in-house. Such a setup is optimal in the case of the THz-amplifier, which exploits quasioptical coupling via dual-mode horns. Furthermore, the setup is compatible with a molecular gas laser, which, in contrary to the solid-state multiplier source of a network vector analyzer, provides a possibility to investigate the amplifier performance in the saturation regime. A polarization loss analysis of the setup and a simple method for calibrating it have been presented in the course of this dissertation. Calibration measurements with photomixers have shown the transmittance and reflectance losses caused by the setup itself to be within 0.7 dB from the ideal 9 dB and 12 dB, respectively.

The latter part of the dissertation focused on the diplexing of the LO- and signal beams in a heterodyne array receiver. Due to the increased waveguide losses at THz-frequencies, quasioptical diplexing with a Martin-Puplett interferometer is often preferred. Misalignment and deformation of the quasioptical components cause the optical path length difference between the two arms of the interferometer to deviate from the desired value, which leads to an incorrect polarization state of the output signal and, consequently, to coupling losses. The position of one roof mirror is typically adjustable, so in a single-pixel receiver, the path length error can be compensated by moving the mirror. In the case of a multi-pixel receiver, the error is different for each pixel, and while the total error can be minimized, it cannot be completely eliminated by moving the mirror. Hence, a ray-tracing program has been developed for investigating the path length differences between different pixels when the quasioptical components of the interferometer are deformed or misaligned. Furthermore, a measurement method for obtaining path length difference information experimentally has been presented. By combining these two approaches, a new method for finding the defects in a diplexer has been proposed. Based on the measurement results, the program is able to compute a component configuration creating the measured path length differences. The results of the simulated defects were demonstrated to be in agreement with verification measurements. Furthermore, five defect param-

eters are shown to be sufficient for reproducing the measured path length differences in a laboratory diplexer and in the diplexer of the multi-pixel receiver CHAMP$^+$. The obtained parameter values are mainly on the order of dozens of micrometers or millidegrees. The only parameter outside the expected range is the lateral shift of a roof mirror with a magnitude of several millimeters. No measurement data were available to confirm the simulation result, but such a misalignment could have been created accidentally during a change of a polarizer. The quasioptical configuration of the diplexer may be corrected based on the information provided by the simulations, which leads to lower optical coupling losses and higher receiver sensitivity. The expansion of the capabilities of the ray-tracing program to allow investigation of quasioptical single sideband filters is planned for the future.

ACKNOWLEDGMENTS

I express my gratitude to my supervisor Viktor Krozer, not only for his guidance and teaching in the area of millimeter/terahertz waves and generally in the world of research, but also for providing a pleasant and informal working atmosphere. I am grateful to Claudio Paoloni from the Lancaster University for the fruitful cooperation during the past four years and for acting as the second assessor of my dissertation. I also thank Rolf Güsten from the Max Planck Institute for Radio Astronomy for making my research stay in Bonn possible, and Thomas Klein for supervising me there. I thank Robert Weikle of the University of Virginia and Thomas Crowe of Virginia Diodes for giving the possibility to use their equipment for S-parameter measurements and the staff members for their help in practical issues. Furthermore, I thank all the friendly and helpful people I got to know in the Electromagnetic Systems group at the Technical University of Denmark, in the Division for Submm Technologies at the Max Planck Institute for Radio Astronomy and at the Physikalisches Institut of the Goethe University Frankfurt, especially Bernd Hils for sharing his insights in optics.

I would like to thank all the partners involved in the OPTHER project, especially Alain Durand for inviting me to discuss the helix slow wave structure at THALES Electron Devices.

Many thanks to Monika Balk and Tilmann Wittig of CST for helping me with many simulation related questions and for carrying out the far-field simulations of the dual-mode horn.

I would like to thank my family and Gisela for the love and encouragement.

Finally, I would like to acknowledge the financial support provided by the FP7 European Project No. 224356 "OPTHER - Optically Driven Terahertz Amplifiers".

REFERENCES

[1] M. Aloisio and P. Waller. Analysis of helical slow-wave structures for space TWTs using 3-D electromagnetic simulators. *IEEE Transactions on Electron Devices*, 52(5):749–754, May 2005.

[2] T.M. Antonsen and B. Levush. Traveling-wave tube devices with nonlinear dielectric elements. *IEEE Transactions on Plasma Science*, 26(3):774–786, Jun. 1998.

[3] C.M. Armstrong. The truth about terahertz. *IEEE Spectrum*, 49(9):36–41, Sept. 2012.

[4] R.J. Barker, J.H. Booske, N.C. Luhmann Jr., and G.S. Nusinovich, editors. *Modern Microwave and Millimeter-Wave Power Electronics*. Wiley-IEEE Press, 2005.

[5] D.J. Bates and E.L. Ginzton. A Traveling-Wave Frequency Multiplier. *Proceedings of the IRE*, 45(7):938–944, Jul. 1957.

[6] A.L. Betz and R.T. Boreiko. A Practical Schottky Mixer for 5 THz (Part II). In *7th International Symposium on Space Terahertz Technology*, pages 503–510, 1996.

[7] J.H. Booske, M.C. Converse, C.L. Kory, C.T. Chevalier, D.A. Gallagher, K.E. Kreischer, V.O. Heinen, and S. Bhattacharjee. Accurate parametric modeling of folded waveguide circuits for millimeter-wave traveling wave tubes. *IEEE Transactions on Electron Devices*, 52(5):685–694, May 2005.

[8] J.H. Booske, R.J. Dobbs, C.D. Joye, G.R. Kory, C.L. Neil, G.-S. Park, and R.J. Park, J. Temkin. Vacuum electronic high power terahertz sources. *IEEE Transactions on Terahertz Science and Technology*, 1(1):54–75, 2012.

[9] E.R. Brown, F.W. Smith, and K.A. McIntosh. Coherent millimeter-wave generation by heterodyne conversion in low-temperature-grown GaAs photoconductors. *Journal of Applied Physics*, 73(3):1480–1484, 1993.

[10] I. Cámara Mayorga. *Photomixers as Tunable Terahertz Local Oscillators*. PhD thesis, Rheinischen Friedrich-Wilhelms-Universität Bonn, 2008.

[11] I. Cámara Mayorga, E.A. Michael, A. Schmitz, P. van der Wal, R. Güsten, K. Maier, and A. Dewald. Terahertz photomixing in high energy oxygen- and nitrogen-ion-implanted GaAs. *Applied Physics Letters*, 91(3):031107–1–031107–3, 2007.

[12] G. Chattopadhyay. Technology, Capabilities, and Performance of Low Power Terahertz Sources. *IEEE Transactions on Terahertz Science and Technology*, 1(1):33–53, 2012.

[13] G. Chattopadhyay, E. Schlecht, J.S. Ward, J.J. Gill, H.H.S. Javadi, F. Maiwald, and I. Mehdi. An all-solid-state broad-band frequency multiplier chain at 1500 GHz. *Microwave Theory and Techniques, IEEE Transactions on*, 52(5):1538–1547, May 2004.

[14] G. Chin. Optically pumped submillimeter laser heterodyne receivers: astrophysical observations and recent technical developments. *Proceedings of the IEEE*, 80(11):1788–1799, Nov. 1992.

[15] K. R. Chu, H. Guo, and V. L. Granatstein. Theory of the Harmonic Multiplying Gyrotron Traveling Wave Amplifier. *Phys. Rev. Lett.*, 78:4661–4664, Jun. 1997.

[16] L.J. Chu and J.D. Jackson. Field Theory of Traveling-Wave Tubes. *Proceedings of the IRE*, 36(7):853–863, Jul. 1948.

[17] C. Chua, S. Aditya, J.M. Tsai, and S. Tang, M. Zhongxiang. Microfabricated Planar Helical Slow-Wave Structures Based on Straight-Edge Connections for THz Vacuum Electron Devices. *Terahertz Science and Technology*, 4(4):208–229, Dec. 2011.

[18] Ciersiang Chua, J.M. Tsai, S. Aditya, Min Tang, Soon Wee Ho, Zhongxiang Shen, and Lei Wang. Microfabrication and Characterization of W-Band Planar Helix Slow-Wave Structure With Straight-Edge Connections. *IEEE Transactions on Electron Devices*, 58(11):4098–4105, Nov. 2011.

[19] M.R. Currie and J.R. Whinnery. The Cascade Backward-Wave Amplifier: A High-Gain Voltage-Tuned Filter for Microwaves. *Proceedings of the IRE*, 43(11):1617–1631, Nov. 1955.

[20] G.C. Dalman. New waveguide-to-coplanar waveguide transition for centimetre and millimetre wave applications. *Electronics Letters*, 26(13):830–831, Jun. 1990.

[21] J.A. Dayton, C.L. Kory, G.T. Mearini, D. Malta, M. Lueck, and K. Gilchrist. Applying microfabrication to helical vacuum electron devices for THz applications. In *IEEE International Vacuum Electronics Conference (IVEC 2009)*, pages 41–44, Apr. 2009.

[22] J.A. Dayton, C.L. Kory, G.T. Mearini, D. Malta, M. Lueck, and B. Vancil. Fabrication and testing of the 0.650 THz helical BWO. In *IEEE Thirteenth International Vacuum Electronics Conference (IVEC), 2012*, pages 33–34, Apr. 2012.

[23] T. de Graauw et al. The Herschel-Heterodyne Instrument for the Far-Infrared (HIFI). *Astronomy & Astrophysics*, 518:L6, Jul. 2010.

[24] P. Dixit, C.W. Tan, L. Xu, N. Lin, J. Miao, J.H.L. Pang, P. Backus, and R. Preisser. Fabrication and characterization of fine pitch on-chip copper interconnects for advanced wafer level packaging by a high aspect ratio through AZ9260 resist electroplating. *Journal of Micromechanics and Microengineering*, 17(5):1078–1086, 2007.

[25] Christian Y. Drouet d'Aubigny, Christopher K. Walker, Abram G. Young, Paul Gensheimer, Dathon R. Golish, and Christopher E. Groppi. Terahertz traveling wave tube amplifiers as high-power local oscillators for large heterodyne receiver arrays. *Proceedings of SPIE*, 7741:774115–774115–10, 2010.

[26] N.R. Erickson. A Very Low-Noise Single-Sideband Receiver for 200–260 GHz. *IEEE Transactions on Microwave Theory and Techniques*, 33(11):1179–1188, 1985.

[27] Jerome Faist, Federico Capasso, Deborah L. Sivco, Carlo Sirtori, Albert L. Hutchinson, and Alfred Y. Cho. Quantum Cascade Laser. *Science*, 264(5158):553–556, 1994.

[28] M.C. Gaidis, H.M. Pickett, C.D. Smith, S.C. Martin, R.P. Smith, and P.H. Siegel. A 2.5-THz Receiver Front End for Spaceborne Applications. *IEEE Transactions on Microwave Theory and Techniques*, 48(4):733–739, 2000.

[29] P.D. Gensheimer, C.K. Walker, R.W. Ziolkowski, and C. Drouet d'Aubigny. Full-Scale Three-Dimensional Electromagnetic Simulations of a Terahertz Folded-Waveguide Traveling-Wave Tube Using ICEPIC. *IEEE Transactions on Terahertz Science and Technology*, 2(2):222–230, Mar. 2012.

[30] J.W. Gewartowski and H.A. Watson. *Principles of electron tubes*. D. Van Nostrand Company, Inc., 1965.

[31] A.S. Gilmour Jr. *Principles of Traveling Wave Tubes*. Artech House, 1994.

[32] P.F. Goldsmith. Quasi-optical techniques. *Proceedings of the IEEE*, 80(11):1729–1747, Nov. 1992.

[33] P.F. Goldsmith. *Quasioptical Systems*. IEEE Press, 1998.

[34] U.U. Graf and S. Heyminck. A Novel Type of Phase Grating for THz Beam Multiplexing. In *11th International Symposium on Space Terahertz Technology*, 2000.

[35] C.E. Groppi and J.H. Kawamura. Coherent Detector Arrays for Terahertz Astrophysics Applications. *IEEE Transactions on Terahertz Science and Technology*, 1(1):85–96, Sept. 2011.

[36] R. Güsten, L. Å. Nyman, P. Schilke, K. Menten, C. Cesarsky, and R. Booth. The Atacama Pathfinder EXperiment (APEX) - a new submillimeter facility for southern skies. *Astronomy & Astrophysics*, 454:L13–L16, Aug. 2006.

[37] J.L. Hesler, W.R. Hall, T.W. Crowe, II Weikle, R.M., Jr Deaver, B.S., R.F. Bradley, and Shing-Kuo Pan. Fixed-tuned submillimeter wavelength waveguide mixers using planar Schottky-barrier diodes. *IEEE Transactions on Microwave Theory and Techniques*, 45(5):653–658, May 1997.

[38] S. Heyminck, U. U. Graf, R. Güsten, J. Stutzki, H. W. Hübers, and P. Hartogh. GREAT: the SOFIA high-frequency heterodyne instrument. *Astronomy & Astrophysics*, 542:L1, Jun. 2012.

[39] H.-W. Hubers. Terahertz Heterodyne Receivers. *IEEE Journal of Selected Topics in Quantum Electronics*, 14(2):378–391, Mar-Apr. 2008.

[40] H.-W. Hubers, H. Richter, S. Pavlov, A. Semenov, A. Tredicucci, L. Mahler, H. Beere, and D. Ritchie. Laser Local Oscillators for Heterodyne Receivers beyond 2 Terahertz. *Frequenz*, 62(5-6):111–117, Jun. 2008.

[41] J.F. Johansson. A Gauss-Laguerre Analysis of the Dual-Mode ('Potter') Horn. In *Fourth International Symposium on Space Terahertz Technology*, pages 134–138, 1993.

[42] T.W. Johansson, S. Foley, S. Durant, Kai Hui, Y. Duan, and J.L. Hesler. VNA Frequency Extenders to 1.1 THz. In *36th International Conference on Infrared, Millimeter and Teraherz Waves (IRMMW-THz)*, Oct. 2011.

[43] H. Karttunen, P. Kröger, H. Oja, M. Poutanen, and K.J. Donner. *Fundamental Astronomy*. Springer, 5 edition, 2007.

[44] C. Kasemann, R. Güsten, S. Heyminck, B. Klein, T. Klein, S.D. Philipp, A. Korn, G. Schneider, A. Henseler, A. Baryshev, and T.M. Klapwijk. CHAMP$^+$: a powerful array receiver for APEX. *Proceedings of SPIE*, 6275:62750N, 2006.

[45] C. Kasemann, S. Heyminck, A. Bell, A. Belloche, C. Castenholz, R. Güsten, H. Hafok, A. Henseler, S. Hochgürtel, B. Klein, T. Klein, I. Krämer, A. Korn, K. Meyer, D. Muders, F. Pacek, F. Schäfer, G. Schneider, G. Wieching, H-J. Wunsch, A. Baryshev, R. Hesper, T. Zijlstra, C.F.J. Lodewijk, and T.M. Klapwijk. CHAMP$^+$: A powerful submm Heterodyne Array. In *19th International Symposium on Space Terahertz Technology*, Apr. 2008.

[46] J. Kloosterman, C. Groppi, C. Kulesa, C. Walker, T. Cottam, E. Liggett, D. Lesser, M. Borden, P. Schickling, D. Golish, C. d'Aubigny, S. Weinreb, G. Jones, J. Barden, H. Mani, T.K.J. Kooi, A. Lichtenberger, T. Cecil, P. Puetz, G. Narayanan, A. Hedden, and Xu X. A Progress Update on Supercam: A 345 GHz, 64-pixel Heterodyne Imaging Spectrometer. In *22nd International Symposium on Space Terahertz Technology*, pages 174–178, 2011.

[47] C.L. Kory and Jr Dayton, J.A. Computational investigation of experimental interaction impedance obtained by perturbation for helical traveling-wave tube structures. *IEEE Transactions on Electron Devices*, 45(9):2063–2071, Sept. 1998.

[48] H.G. Kosmahl. Modern multistage depressed collectors–A review. *Proceedings of the IEEE*, 70(11):1325–1334, Nov. 1982.

[49] M. Kotiranta, B. Hils, B. Batz, and V. Krozer. Quasioptical Setup for Transmission and Reflection Measurements. In *37th International Conference on Infrared, Millimeter and Teraherz Waves (IRMMW-THz)*, Sept. 2012.

[50] M. Kotiranta and V. Krozer. Harmonic distortion in a traveling wave tube at 850 GHz and its use in frequency multiplication. In *Workshop on Integrated Nonlinear Microwave and Millimetre-Wave Circuits (INMMIC 2011)*, pages 1–4, Apr. 2011.

[51] M. Kotiranta, V. Krozer, and V. Zhurbenko. Square helix TWT for THz frequencies. In *35th International Conference on Infrared, Millimeter and Teraherz Waves (IRMMW-THz)*, Aug. 2010.

[52] M. Kotiranta, C. Leinz, T. Klein, V. Krozer, and H.-J. Wunsch. Characterization of Imperfections in a Martin-Puplett Interferometer Using Ray-Tracing. *Journal of Infrared, Millimeter and Terahertz Waves*, 33:1138–1148, 2012.

[53] M. Kotiranta, W. von Spiegel, V. Krozer, D. Bariou, and A.J. Durand. Terahertz dual-mode horn antenna with a vacuum window. In *IEEE Thirteenth International Vacuum Electronics Conference (IVEC), 2012*, pages 193–194, Apr. 2012.

[54] J. Kraus and D. Fleisch. *Electromagnetics with Applications*. McGraw-Hill, New York, 5. edition, 1999.

[55] C. Kulesa. Terahertz Spectroscopy for Astronomy: From Comets to Cosmology. *IEEE Transactions on Terahertz Science and Technology*, 1(1):232–240, Sept. 2011.

[56] S. Kumar Datta and L. Kumar. A Simple Closed-Form Formula for Plasma-Frequency Reduction Factor for a Solid Cylindrical Electron Beam. *IEEE Transactions on Electron Devices*, 56(6):1344–1346, Jun. 2009.

[57] D.K. Lambert and P.L. Richards. Martin-Puplett interferometer: an analysis. *Applied Optics*, 17(10):1595–1602, 1978.

[58] J. Lesurf. *Millimetre-wave Optics, Devices & Systems*. Adam Hilger, Bristol, 1990.

[59] H. A. Leupold, A. Tilak, and E. Potenziani. Permanent magnet spheres: Design, construction, and application (invited). *Journal of Applied Physics*, 87(9):4730–4734, May 2000.

[60] Jan Machac and Wolfgang Menzel. On the design of waveguide-to-microstrip and waveguide-to-coplanar line transitions. In *23rd European Microwave Conference, 1993*, pages 615–616, Sept. 1993.

[61] A. Maestrini, I. Mehdi, J.V. Siles, J.S. Ward, R. Lin, B. Thomas, C. Lee, J. Gill, G. Chattopadhyay, E. Schlecht, J. Pearson, and P. Siegel. Design and Characterization of a Room Temperature All-Solid-State Electronic Source Tunable From 2.48 to 2.75 THz. *IEEE Transactions on Terahertz Science and Technology*, 2(2):177–185, Mar. 2012.

[62] A. Maestrini, J.S. Ward, J.J. Gill, Choonsup Lee, B. Thomas, R.H. Lin, G. Chattopadhyay, and I. Mehdi. A Frequency-Multiplied Source With More Than 1 mW of Power Across the 840–900-GHz Band. *IEEE Transactions on Microwave Theory and Techniques*, 58(7):1925–1932, Jul. 2010.

[63] T. Manabe and A. Murk. Transmission and Reflection Characteristics of Slightly Irregular Wire-Grids for Arbitrary Angles of Incidence and Grid Rotation. In *14th International Symposium on Space Terahertz Technology*, Apr. 2003.

[64] D.H. Martin and Puplett E. Polarised interferometric spectrometry for the millimetre and submillimetre spectrum. *Infrared Physics*, 10:105–109, 1970.

[65] I.C. Mayorga, A. Schmitz, T. Klein, C. Leinz, and R. Gusten. First in-field application of a full photonic local oscillator to terahertz astronomy. *Terahertz Science and Technology, IEEE Transactions on*, 2(4):393–399, July 2012.

[66] W.R. McGrath. Hot-Electron Bolometer Mixers for Submillimeter Wavelengths: an Overview of Recent Developments. In *Sixth International Symposium on Space Terahertz Technology*, pages 216–228, Mar. 1995.

[67] G.J. Melnick et al. The Submillimeter Wave Astronomy Satellite: Science Objectives and Instrument Description. *The Astrophysical Journal Letters*, 539(2):L77, 2000.

[68] M. Mineo and C. Paoloni. Double-Corrugated Rectangular Waveguide Slow-Wave Structure for Terahertz Vacuum Devices. *IEEE Transactions on Electron Devices*, 57(11):3169–3175, Nov. 2010.

[69] Eric R. Mueller, Robert Henschke, Jr. William E. Robotham, Leon A. Newman, Lanny M. Laughman, Richard A. Hart, John Kennedy, and Herbert M. Pickett. Terahertz local oscillator for the Microwave Limb Sounder on the Aura satellite. *Appl. Opt.*, 46(22):4907–4915, Aug. 2007.

[70] C. Paoloni, A. Di Carlo, F. Bouamrane, T. Bouvet, A.J. Durand, V. Kotiranta, M. Krozer, S. Megtert, M. Mineo, and V. Zhurbenko. Design and Realization Aspects of 1-THz Cascade Backward Wave Amplifier Based on Double Corrugated Waveguide. *Submitted to IEEE Transactions on Electron Devices*, Nov. 2012.

[71] C. Paoloni, M. Mineo, A. Di Carlo, A.J. Durand, V. Krozer, M. Kotiranta, F. Bouamrane, T. Bouvet, and S. Megtert. 1-THz cascade backward wave amplifier. In *IEEE Thirteenth International Vacuum Electronics Conference (IVEC), 2012*, pages 237–238, Apr. 2012.

[72] E. Pehl. *Mikrowellentechnik*. Hüthig GmbH, 2. edition, 1989.

[73] P. Phillips, L. Ives, C. Kory, M. Read, J. Neilson, M. Caplan, N. Chubun, S. Schwartzkopf, and R. Witherspoon. Backward Wave Oscillators for Terahertz Applications. *Proceedings of SPIE*, 5403:695–703, 2004.

[74] T.G. Phillips and J. Keene. Submillimeter astronomy. *Proceedings of the IEEE*, 80(11):1662–1678, Nov. 1992.

[75] H.M. Pickett, J.C. Hardy, and J. Farhoomand. Characterization of a Dual-Mode Horn for Submillimeter Wavelengths. *IEEE Transactions on Microwave Theory and Techniques*, 32(8):936–937, 1984.

[76] G.E. Ponchak and R.N. Simons. A new rectangular waveguide to coplanar waveguide transition. In *IEEE MTT-S International Microwave Symposium Digest, 1990*, pages 491–492 vol.1, May 1990.

[77] P.D. Potter. A New Horn Antenna with Suppressed Sidelobes and Equal Beamwidths. Technical Report 32-354, Jet Propulsion Laboratory, California Institute of Technology, 1963.

[78] D.M. Pozar. *Microwave Engineering*. John Wiley & Sons, Inc., 3. edition, 2005.

[79] P. Rao and S.K. Datta. Estimation of conductivity losses in a helix slow-wave structure using eigen-mode solutions. In *IEEE International Vacuum Electronics Conference (IVEC 2008)*, pages 99–100, Apr. 2008.

[80] A. Schillaci and P. de Bernardis. On the effect of tilted roof reflectors in Martin-Puplett spectrometers. *Infrared Physics & Technology*, 55:40–44, 2012.

[81] P.H. Siegel. Terahertz technology. *IEEE Transactions on Microwave Theory and Techniques*, 50(3):910–928, Mar. 2002.

[82] R. Simons. *Coplanar Waveguide Circuits, Components, and Systems*. Wiley-IEEE Press, 2001.

[83] P. Sobis. *Advanced Schottky Diode Receiver Front-Ends for Terahertz Applications*. PhD thesis, Chalmers University of Technology, 2011.

[84] G.H. Spencer and M.V.R.K. Murty. General Ray-Tracing Procedure. *Journal of the Optical Society of America*, 52(6):672–678, 1962.

[85] S.M. Sze. *Semiconductor devices, physics and technology*. John Wiley & Sons, Inc., 2 edition, 2001.

[86] D. Thompson, R.D. Pollard, and R.E. Miles. One-port S-parameter measurements using quasi-optical multistate reflectometer. *Electronics Letters*, 34(12):1222–1224, 1998.

[87] M.S. Tobin. A review of optically pumped NMMW lasers. *Proceedings of the IEEE*, 73(1):61–85, Jan. 1985.

[88] J.C. Tucek, M.A. Basten, D.A. Gallagher, K.E. Kreischer, R. Lai, V. Radisic, K. Leong, and R. Mihailovich. A 100 mW, 0.670 THz power module. In *IEEE Thirteenth International Vacuum Electronics Conference (IVEC), 2012*, pages 31–32, Apr. 2012.

[89] R.H. Turrin. Dual Mode Small-Aperture Antennas. *IEEE Transactions on Antennas and Propagation*, 15(2):307–308, 1967.

[90] V. Vasic, A. Murk, and N. Kämpfer. Non-Ideal Quasi Optical Characteristics of Rooftop Mirrors. In *28th Conference on Infrared and Millimeter Waves*, Sept. 2003.

[91] P. Voll, L. Samoska, S. Church, J.M. Lau, M. Sieth, T. Gaier, P. Kangaslahti, M. Soria, S. Tantawi, and D. Van Winkle. A G-band cryogenic MMIC heterodyne receiver module for astronomical applications. In *41st European Microwave Conference (EuMC), 2011*, pages 523–526, Oct. 2011.

[92] C. Walker, C. Groppi, D. Golish, C. Kulesa, A. Hungerford, C.D. d'Aubigny, K. Jacobs, U. Graf, C. Martin, and J. Kooi. PoleStar: An 810 GHz Array Receiver for AST/RO. In *12th International Symposium on Space Terahertz Technology*, pages 540–552, 2001.

[93] M.J. Wengler. Submillimeter-wave detection with superconducting tunnel diodes. *Proceedings of the IEEE*, 80(11):1810–1826, Sept. 1992.

[94] B.S. Williams. Terahertz quantum-cascade lasers. *Nature Photonics*, 1:517–525, Sept. 2007.

[95] J.G. Wohlbier, J.H. Booske, and I. Dobson. The multifrequency spectral Eulerian (MUSE) model of a traveling wave tube. *IEEE Transactions on Plasma Science*, 30(3):1063–1075, Jun. 2002.

[96] A. Wootten and A.R. Thompson. The Atacama Large Millimeter/Submillimeter Array. *Proceedings of the IEEE*, 97(8):1463–1471, Aug. 2009.

[97] G.T. Wrixon. A Superhetrodyne Receiver from 350–400 GHz. In *8th European Microwave Conference*, pages 717–719, Sept. 1978.

[98] E. T. Young, E. E. Becklin, P. M. Marcum, T. L. Roellig, J. M. De Buizer, T. L. Herter, R. Güsten, E. W. Dunham, P. Temi, B.-G. Andersson, D. Backman, M. Burgdorf, L. J. Caroff, S. C. Casey, J. A. Davidson, E. F. Erickson, R. D. Gehrz, D. A. Harper, P. M. Harvey, L. A. Helton, S. D. Horner, C. D. Howard, R. Klein, A. Krabbe, I. S. McLean, A. W. Meyer, J. W. Miles, M. R. Morris, W. T. Reach, J. Rho, M. J. Richter, H.-P. Roeser, G. Sandell, R. Sankrit, M. L. Savage, E. C. Smith, R. Y. Shuping, W. D. Vacca, J. E. Vaillancourt, J. Wolf, and H. Zinnecker. Early Science with SOFIA, the Stratospheric Observatory For Infrared Astronomy. *The Astrophysical Journal Letters*, 749:L17, Apr. 2012.

[99] V. Zhurbenko, V. Krozer, M. Kotiranta, F. Bouamrane, S. Megtert, T. Bouvet, A. Di Carlo, and M. Dispenza. Excitation of a double corrugation slow-wave structure in terahertz range. In *Proceedings of*

the 5th European Conference on Antennas and Propagation (EUCAP), pages 1041–1043, Apr. 2011.

[100] V. Zhurbenko, V. Krozer, M. Kotiranta, T. Rubaek, A. Durand, and R. Marchesin. Submillimeter wave antenna with slow wave feed line. In *SBMO/IEEE MTT-S International Microwave and Optoelectronics Conference (IMOC), 2009*, pages 388–392, Nov. 2009.

[101] J. Zmuidzinas and P.L. Richards. Superconducting detectors and mixers for millimeter and submillimeter astrophysics. *Proceedings of the IEEE*, 92(10):1597–1616, Oct. 2004.